Magnetic Trapping Apparatus and Frequency Stabilization of a Ring Cavity Laser for Bose-Einstein Condensation Experiments

Ina B. Kinski

Diplomarbeit zur Erlangung
des Titels Diplomphysikerin

Vorgelegt am
Institut für Experimentalphysik
Fachbereich Physik
Freie Universität Berlin

April 2005

Durchgeführt am

Physics Department
University of Otago
Dunedin, New Zealand
unter der Leitung von
Dr. Andrew C. Wilson

und am

Institut für Experimentalphysik
Leopold–Franzens–Universität Innsbruck
Innsbruck, Österreich
unter der Leitung von
Prof. Dr. Rudolf Grimm.

Betreut von

Prof. Dr. Dr. h.c. Günter Kaindl
Institut für Experimentalphysik
Freie Universität Berlin

Abstract

In this thesis, two experimental projects carried out in the field of ultracold quantum gases are presented.

The first one deals with the construction of a magnetic trapping apparatus that is used to create Bose–Einstein Condensation (BEC). Magnetic traps are used to confine and compress neutral pre–cooled atoms and to reach the necessary temperatures and densities for condensation. Along with sophisticated timing and ultra–high vacuum systems, they form the core of nearly every macroscopic BEC experiment. During a visiting appointment at the University of Otago, New Zealand, computer simulations in MATLAB were developed to model the magnetic field distribution of a QUIC (quadrupole–Ioffe–configuration) trap [Ess98]. Based on the results, a coil arrangement was designed and built. The configuration allows flexible optical access to the BEC and is distinguished by a stable and compact mounting system. This first part of the thesis summarizes the related physics of magnetic trapping, as well as the practical issues concerning the design and construction of copper wire coils.

The second project involves the implementation of a laser frequency stabilizing scheme, which is based on the use of an optical mirror cavity and the Pound–Drever–Hall (PDH) technique [Dre83]. The stabilized laser is used to perform experiments with BECs in optical lattice potentials. In the course of a stay in the rubidium BEC laboratory at the University of Innsbruck, Austria, an appropriate cavity together with laser locking electronics were assembled and characterized. The cavity's transmission frequency is controlled by means of a temperature stabilization arrangement. This second part of the thesis summarizes the relevant background on optical mirror cavities, the Pound–Drever–Hall method, and gives constructional details on the lock's components.

Zusammenfassung

Diese Diplomarbeit besteht aus zwei experimentellen Projekten, die auf dem Gebiet der ultrakalten Quantengase durchgeführt wurden.

Das erste Projekt handelt von der Planung, der Konstruktion und dem Aufbau einer Magnetfalle, mit der Bose–Einstein–Kondensation (BEC) experimentell realisiert wird. Magnetfallen dienen hierbei dazu, neutrale vorgekühlte Atome festzuhalten und zu komprimieren, damit die nötigen Temperaturen und Dichten zur Herstellung von BEC erreicht werden. Neben ausgefeilten Regelungstechniken und Versuchskammern, in den ultrahohes Vakuum herrscht, bilden sie das Herzstück der meisten makroskopischen BEC–Apparaturen. Im Rahmen eines Gastaufenthaltes an der University von Otago, Neuseeland, wurden MATLAB–Computersimulationen entwickelt, die die Magnetfeldverteilung einer QUIC (Quadrupole–Ioffe–configuration) Falle [Ess98] berechnen. Auf den Ergebnissen basierend wurden Spulenkörper geplant und konstruiert. Der kompakte Aufbau der Falle zeichnet sich durch großzügigen optischen Zugang aus. Im ersten Teil der Arbeit wird eine Einführung in das Fangen neutraler Atome gegeben und experimentelle Details zur Herstellung von Kupferdrahtspulen werden vorgestellt.

Der zweite Teil der Arbeit dokumentiert die Implementation einer Frequenzstabilisierung eines Ring–Cavity–Lasers. Dabei wird ein optischer Spiegelresonator und die Pound–Drever–Hall–Methode [Dre83] verwendet. Im Zusammenhang eines Aufenthaltes im Rubidium–BEC–Labor an der Universtität Innsbruck, Österreich, wurde ein solcher Spiegelresonator und die dazugehörige Elektronik aufgebaut. Der stabilisierte Laser findet bei Experimenten mit BECs in optischen Gitterpotentialen Verwendung. Die Transmissionsfrequenz des Resonators wird mit Hilfe einer Temperaturstabilisierung kontrolliert. In diesem zweiten Teil der Arbeit werden Hintergründe von Spiegelresonatoren und der Pound–Drever–Hall–Methode erläutert und experimentelle Details zu den erstellten Komponenten vorgestellt.

Contents

List of Figures

Introduction: Bose–Einstein condensation

In the microscopic world of quantum mechanics, all particles can be classified as either *fermions* or *bosons*. When studying systems of either kind at moderately high temperatures, both demonstrate behavior in accordance with the Boltzmann distribution: of all possible energy states of a given system, there is no single state that accommodates a large fraction of all the particles. For decreasing temperatures, the wave–like behavior of the particles, which was introduced by de Broglie's matter waves (Nobel Prize 1929), prevails.

Fermions possess an intrinsic half–odd spin and are described by particle wavefunctions (Schrödinger, Nobel Prize 1933) that change their sign upon the exchange of two particles. Consequently, fermions are restricted by the Pauli exclusion principle (Nobel Prize 1945) that forbids them to occupy the same quantum state. Electrons are fermions and, for instance, the composition of the elements in the periodic table is based on their *unsocial* behavior.

Bosons, on the other hand, have an integer spin and are described by wavefunctions that are invariant under particle exchange. There exists no restriction on how many identical particles can occupy the same one–particle state, and a vivid example for this is the *gregarious* behavior of photons in a laser. A single quantum state can be occupied by a large fraction of all the bosons in a system. The collection of a macroscopic fraction of all particles of a system into the ground state constitutes a phase transition, and is referred to as **Bose–Einstein condensation (BEC)**.

As Einstein has pointed out [Ein25], in an ideal gas BEC occurs solely due to quantum statistical effects. The phase–space density, $n\lambda_{dB}^3$, for a condensate satisfies the condition

$$n\lambda_{dB}^3 \geq \zeta(\tfrac{3}{2}) = 2.612, \tag{1}$$

where the thermal de Broglie wavelength $\lambda_{dB} = h/\sqrt{2\pi m k_B T}$ must be of the same order as the usually much greater inter–particle separation $n^{-1/3}$. Here h is Planck's constant, k_B is the Boltzmann constant, and m is the atomic mass.

$\zeta(x)$ is the Riemann–Zeta function. From equation (1) and the definition of the de Broglie wavelength, one can see that the transition occurs at a critical temperature

$$T_C = \frac{h^2}{2\pi m k_B} \left(\frac{n}{\zeta(\frac{3}{2})} \right)^{2/3}. \tag{2}$$

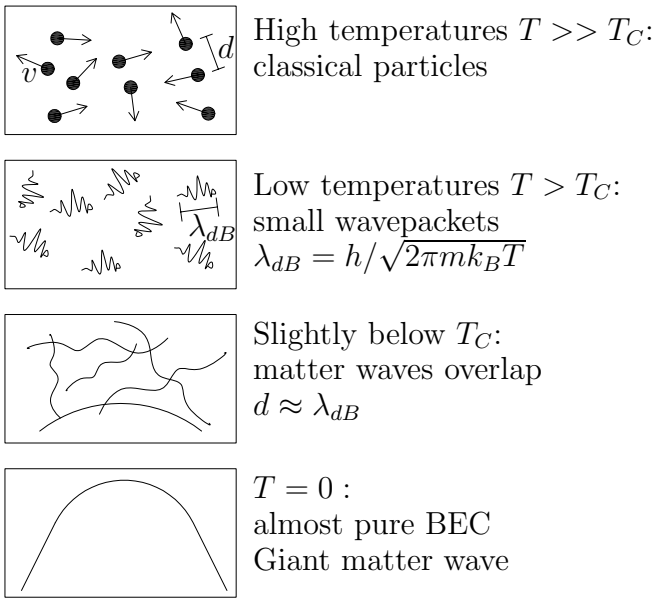

Figure 1: Schematic transition from a weakly interacting room temperature gas to a BEC. At high temperatures, the gas can be treated as a system of classical particles moving at a velocity v. In a simple quantum mechanical description, the atoms can be regarded as wavepackets with a spatial extension of λ_{dB}. At the BEC transition temperature, the de Broglie wavelength becomes comparable to the inter–atom distance d. The thermal atomic cloud vanishes and an almost pure Bose condensate forms as T is lowered towards zero. Adapted from [Ket99].

The transition from a room temperature gas to a BEC is illustrated in figure 1. At moderately high temperatures, $T >> T_C$, the particles show their particle–like behavior. They move with a thermal velocity v and are spaced by the inter–particle distance d. For lower temperatures, but $T > T_C$, the gas atoms can be described by small wavepackets with the thermal de Broglie wavelength λ_{dB}. At the critical temperature T_C, the wavefunctions spread out and start to overlap. The de Broglie wavelength and inter–particle separation are of the same order, as required by equation (1). An overall macroscopic matter wave develops and BEC is reached.

Einstein predicted BEC in 1924 [Ein25] after generalizing Bose's new statistical method of describing photons as entirely indistinguishable particles [Bos24]. London attributed the phenomenon of superfluidity in liquid helium to BEC in 1938. We know today that the interactions between particles in the liquid phase are too strong to condense more than 10 % of the particles.

The experimental realization of BEC in weakly interacting systems requires advanced cooling and trapping techniques of low density atomic clouds. Three–body collisions that would cause classical condensation into solids or liquids are suppressed by keeping the gas dilute. Using laser and evaporative cooling, the temperature of the cloud is lowered by a factor of 10^9. In 1995, Anderson *et al.* achieved BEC in ^{87}Rb [And95]. Figure 2 shows an absorption image of this first BEC. It illustrates the velocity distribution of an atomic cloud with a transition temperature $T_C \approx 280\,\mathrm{nK}$.

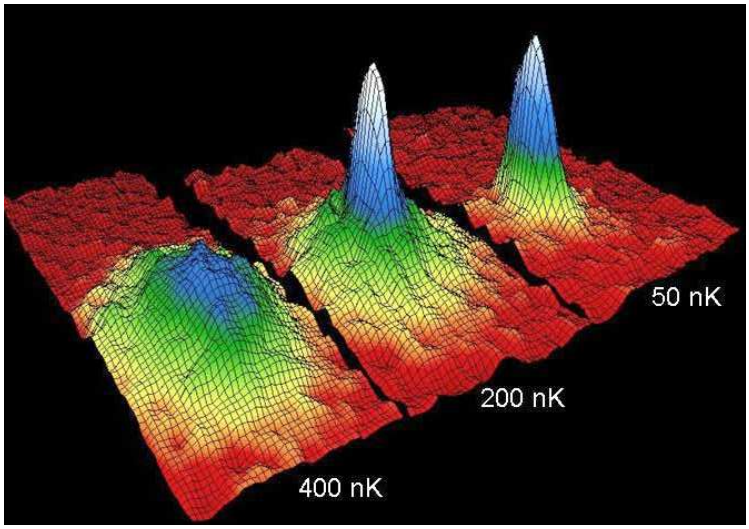

Figure 2: False–color images of the velocity distribution of an ultracold ^{87}Rb cloud obtained by absorption imaging. The left most image shows the cloud just before the appearance of BEC, and the next just after the formation of BEC at $T_C \approx 280\,\mathrm{nK}$. The right most shows a nearly pure condensate containing only 2000 atoms after further evaporative cooling had been applied. The circular pattern of the non–condensed fraction (mostly yellow and green) is an indication for the isotropic velocity distribution, which is consistent with thermal equilibrium. The condensate fraction (mostly blue and white) is elliptical and indicates a highly non–thermal velocity distribution. The peak is an image of a single, macroscopically occupied wavefunction. The field of view of each image is $200\,\mu$m by $270\,\mu$m [Ens98]. Figure taken from the JILA webpage http://jilawww.colorado.edu/bec/.

Today, Bose Einstein condensation, "a new window into the quantum world" [Ket99], is the basis of a whole field of new and exciting experiments and theories. Condensates of bosonic gases, mostly ^{87}Rb, are routinely produced in over 30 laboratories world–wide. BEC has long been achieved in all other stable alkali species, hydrogen, metastable ^{4}He, and most recently, ^{52}Cr [Gri05]. BEC has been achieved with more than 10^5 molecules of Li_2 [Joc03] and also with fermionic atom pairs [Reg04]. This opens up the possibility to study the crossover from a BEC to a Bardeen–Cooper–Schrieffer (BCS) superfluid [Bar04]. The research into ultracold molecules, quantum information, and more fundamental research concerning the properties of both bosonic and fermionic ultracold gases continues at a breathtaking speed.

This diploma thesis contains two experimental projects, carried out in BEC laboratories in New Zealand and Austria. The first deals with the construction of a magnetic trapping apparatus, which is a key tool to achieve necessary phase–space densities for evaporative cooling. A short overview concerning the experimental realization of BEC is given in chapter 1. The second project focusses on the implementation of a frequency stabilization scheme of a ring–cavity laser. This laser is used for experiments with ^{87}Rb BECs in optical lattice potentials, where the transition from a BEC superfluid state to a Mott insulating state can be observed. A brief introduction to Mott insulators and the required optical lattice stability is presented in chapter 7.

Part I

Magnetic Trapping Apparatus Otago, New Zealand

Chapter 1

Introduction

Trapping and storing of particles is key to scientific results in a large range of physics experiments. In the low–energy regime, advances in laser cooling and trapping paved the road to new experiments and the realization of Bose–Einstein condensation (BEC). The production of a BEC from a bosonic dilute gas requires multiple refined mechanisms to function in immediate succession. The crucial steps are described briefly in the following paragraph. Excellent reviews on most experimental aspects of BEC formation can be found in a review by W. Ketterle *et al.* [Ket99], and references therein.

To create a BEC in a dilute gas, approximately 10^9 bosonic atoms are isolated in an ultra–high vacuum (UHV) chamber and confined in a Magneto–Optical trap (MOT). This trap consists of counter–propagating laser beams at appropriate wavelengths and polarizations. Laser cooling (Nobel Prize 1997) in three dimensions is used to slow and effectively cool the atoms down to micro–Kelvin temperatures. The first MOT was developed in 1987 [Raa87], but attempts to create BEC with the use of optical cooling and trapping techniques alone fail, because the number and density of atoms is then limited by inelastic collisions and absorption of scattered laser light. Instead, the pre–cooled atomic cloud is loaded into a magnetic trap, where the necessary phase–space densities can be achieved. In the trap, an inhomogeneous magnetic field exerts a force on the magnetic dipole of the neutral atoms. This force depends on their internal state, leading to trapping of specific hyperfine states only. On a conceptual level, the magnetic trap acts similarly to a thermos flask, keeping the atomic ensemble tightly confined and providing the necessary densities to allow effective evaporative cooling. This cooling technique, which achieves the necessary phase–space densities, is illustrated in figure 1.1. Evaporation is performed by applying radio–frequency (rf) sweeps to the thermal cloud. By adequately ramping the resonant frequency, the hotter atoms are removed by

inducing a transition to non–trapped hyperfine states. Resonant absorption depends on the magnitude of the magnetic field. Since the hot atoms populate different regions of the magnetic field than the colder ones, they can be removed selectively. Finally, the cloud effectively cools down due to rethermalization of the remaining atoms. The particle number depletes to about 10^5 and the critical temperature of approximately 100 nK is reached.

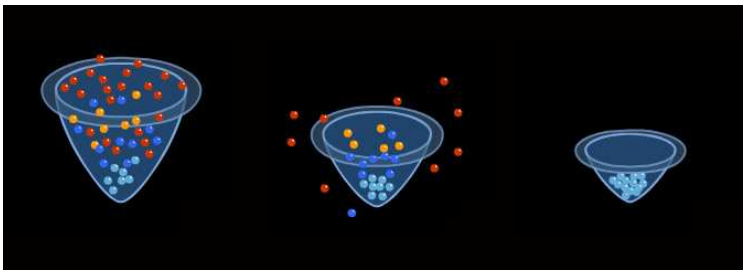

Figure 1.1: Illustration of evaporative cooling process in a magnetic trap. The deep trap contains hot and cold atoms. Hot atoms are ejected by rf–induced lowering of the trap. The ensemble cools down due to rethermalization. Figure courtesy of I. Bloch.

Magnetic traps are therefore a vital part towards reaching the necessary temperatures and densities for creating BEC: they isolate the atoms, keep them tightly compressed during evaporative cooling to achieve high collision rates, and finally hold the condensate for study. As evaporation is performed slowly ($\sim$ 30 seconds), magnetic traps require low heating and loss rates.

When designing and constructing a magnetic trap, there are many basic configurations available that can be extended to an arbitrary degree. General restrictions are imposed by the geometry of the coil or permanent magnet arrangement. Derived from the simple quadrupole trap, one of the pioneering advances in the field was the invention of the QUIC (quadrupole–Ioffe–configuration) trap. It was developed by T. Esslinger *et al.* [Ess98] in 1998 and is now widely used.

In course of a project at the "Ultracold Atoms Research" Group at the University of Otago, and under the supervision of A. C. Wilson, I have planned, modelled and built a magnetic trapping apparatus of the QUIC type. Basic principles of magnetic trapping of neutral atoms and the outline of the QUIC trap are presented.

Chapter 2

Background and basics

Unlike charged particles, which are subject to the relatively strong Coulomb interaction and can be trapped in electric fields, neutral atoms display much smaller interactions with external fields. Attempts to trap them in solely static electric fields by inducing a dipole fail, because the atoms are attracted to regions of high field. As Laplace's equation does not allow for a static local electric field maximum in free space, the atoms cannot be confined.

When placing neutral atoms into oscillating light fields or optical traps (e.g. standing wave) that are tuned near atomic transitions, they are subject to absorption and spontaneous emission of photons. The trap's performance is restricted by the so–called recoil limit: the radiation force one photon recoil exerts on one atom limits the lowest achievable temperature of the atomic cloud to approximately $10\,\mu$K. Optical dipole traps [Gri00], in contrast, employ far–detuned light and rely on the interaction of the electric dipole with the laser field. Dipole traps are used for achieving BEC, but they are generally shallow. The trap depth, which is defined as the temperature at which the atoms have sufficient kinetic energy to escape the trapping potential, is below one μK for optical dipole traps.

As magnetic forces are strongest for atoms with an unpaired electron, magnetic traps are a convenient starting point for successful BEC experiments using pre–cooled alkali atoms. A simple computation illustrates why pre–cooling of the atomic sample is important for the use of magnetic traps: consider the magnetic dipole moment of an alkali atom to be on the order of a Bohr magneton, μ_B. In order to produce a trap depth of 1 K, fields on the order of 1.4 T are required. Temperatures of a few μK are easily reached with

laser cooling and fields of only a few Gauss[1] are sufficient to tightly confine the atoms.

Magnetic trapping has the advantage that, in the absence of near–resonant laser light, no excited states are populated and spontaneous emission cannot occur. The trap depth is large and typically amounts to 100 mK. Due to a considerable trapping volume, fast and efficient evaporation can be performed and studies of the BEC benefit from an improved signal–to–noise ratio. A disadvantage of this trapping method is its dependence on the internal state of the participating atoms. Experiments concerning the internal dynamics are limited to a few special cases.

2.1 Neutral atoms in magnetic fields

When an atom with a magnetic dipole moment is exposed to an external magnetic field, the dipole experiences a torque. This results in a magnetic potential energy shift ΔE, which is called Zeeman effect and can be written as

$$\Delta E = -\vec{\mu} \cdot \vec{B}, \tag{2.1}$$

where $\vec{\mu}$ is the magnetic moment of the atom and $\vec{B}$ the magnetic field.

Neutral alkali atoms posses a large magnetic moment due to the single unpaired electron. In the case of ^{87}Rb, the resulting magnetic moment $\vec{\mu}$ is composed of the electron orbital and spin angular momenta, and contributions from the nucleus. The coupling between the angular momentum $\vec{L}$ of the outer electron and its spin angular momentum $\vec{S}$ results in a fine structure according to $\vec{J} = \vec{L} + \vec{S}$. The hyperfine structure results from the coupling of the total electron angular momentum $\vec{J}$ and the total nuclear momentum $\vec{I}$ to the total angular momentum $\vec{F} = \vec{J} + \vec{I}$. According to Bohr's quantization rule that angular momenta exist only in integer and half–odd multiples of Planck's constant $\hbar$, the magnetic moment $\vec{\mu}$ can be written as

$$\vec{\mu} = -g_F \mu_B (\vec{F}/\hbar), \tag{2.2}$$

where $\vec{F}/\hbar$ is dimensionless and $\mu_B = e\hbar/(2m_e)$ is the Bohr magneton. The gyro–magnetic ratio g_F can be calculated with

$$g_F = g_J \cdot \frac{F(F+1) - I(I+1) + J(J+1)}{2F(F+1)}, \tag{2.3}$$

where for the ^{87}Rb $5^2S_{1/2}$ electronic ground state, the Landé–factor $g_J \approx 2$ [Ste01]. For a magnetic field in the z direction, we obtain equally spaced

[1] Gauss is still commonly used and the conversion into the SI unit Tesla is $10^4\,\mathrm{G} = 1\,\mathrm{T}$.

energy levels

$$E_{m_F} = \mu_B g_F m_F B_z, \tag{2.4}$$

which scale with the magnetic quantum number m_F. As long as the energy shift due to the magnetic field is small compared to the hyperfine splitting (which is on the order of 7 GHz for ^{87}Rb), $\vec{F}^2$ and F_z commute with the Hamilton operator, and F and m_F are good quantum numbers. For given J, I, and F, we can label the appropriate energy levels using m_F.

Figure 2.1 shows the Zeeman splitting of the $5^2S_{1/2}$ hyperfine ground state of ^{87}Rb as calculated by the Breit–Rabi formula [Ste01, Eqn. (26)]. The abscissa shows the strength of the external magnetic field in two different regimes. The state is characterized by $I = 3/2$ and $J = 1/2$ (due to $L = 0$ and $S = 1/2$), so that the total angular momenta of $F = 1$ and $F = 2$ are present. The g_F–factors are calculated using equation (2.3) to be $-1/2$ and $+1/2$, respectively. Figure 2.1 (a) illustrates two different regimes: according to the Zeeman effect F is a good quantum number at low fields. In the region of the Paschen–Back effect at high fields on the right hand side, J is a good quantum number, and the grouping is done according to the appropriate quantum number m_J. Figure 2.1 (b) shows the linear regime that we are interested in. With the magnetic trapping employed here, we are interested in the very left hand limit on both figures.

Trapping neutral atoms requires a local minimum of the magnetic energy potential in equation (2.4). As can be seen there, for $g_F m_F > 0$, this requires B_z to have a local magnetic field minimum. States which satisfy this condition, are referred to as weak–field seekers. In contrast, the strong–field seeking states with $g_F m_f < 0$ cannot be trapped by static magnetic fields since Maxwell's equations do not allow for a magnetic–field maximum in free space. Referring to the ground state of ^{87}Rb, the following states can be magnetically trapped:

$$\begin{array}{llll} |F=2, & m_F=2\rangle & \text{with} & g_F=+1/2 \\ |F=2, & m_F=1\rangle & \text{with} & g_F=+1/2 \\ |F=1, & m_F=-1\rangle & \text{with} & g_F=-1/2 \end{array}$$

The other available states are either not trapped when $m_F = 0$, or are even anti–trapped for $g_F m_F < 0$. They escape the magnetic confinement and are lost. The states where $F = |m_F|$ are trapped most strongly, and due to their scattering properties, atoms in the largest F–state are favorable for the subsequent evaporation process.

When the atoms are trapped in a uniform magnetic field, the magnetic dipole precesses around the magnetic field direction with a constant angular

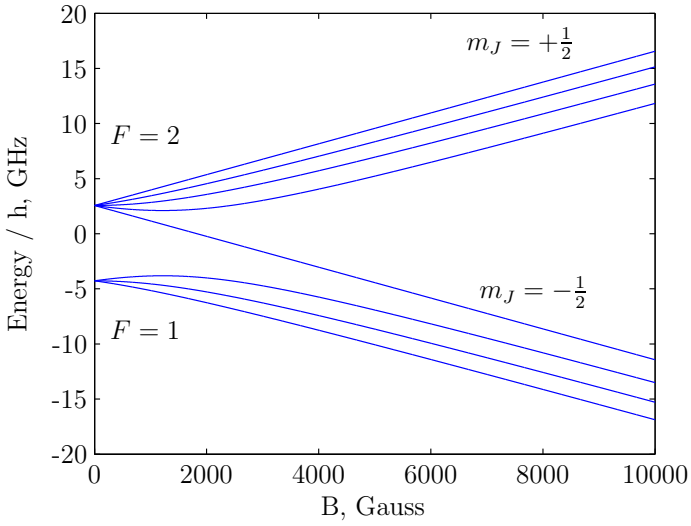

(a) Paschen–Back regime.

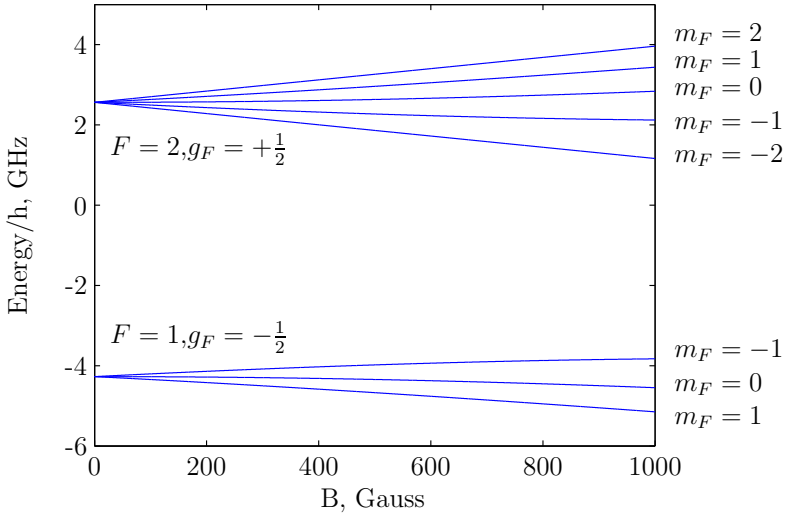

(b) Anomalous Zeeman effect.

Figure 2.1: The ^{87}Rb $5^2S_{1/2}$ ground state energy (and the resulting hyperfine structure) is shown as a function of an external magnetic field. In (a), the levels are grouped according to the value of F in the low field regime (anomalous Zeeman effect) and the value of m_J in the strong field regime (Paschen–Back effect). In figure (b), which shows the region of small fields, the levels are grouped according to F in the anomalous Zeeman effect regime.

frequency ω_L. The Larmor frequency

$$\omega_L = \frac{\mu_B}{\hbar}|\vec{B}| = \frac{e}{2m_e}|\vec{B}| \tag{2.5}$$

describes the motion of the dipole. In an inhomogeneous field, the atom experiences a net force proportional to the magnitude of the magnetic moment

$$\vec{F} = -\mu_B g_F m_F \vec{\nabla}|\vec{B}|. \tag{2.6}$$

The rate at which the magnetic field is changed needs to be sufficiently small so that the magnetic dipole can follow the changing magnetic field adiabatically.

2.2 Quadrupole trap

The most straightforward way to trap atoms magnetically is in a quadrupole field. This field is generated by two identical coils carrying equal currents running in opposite directions, as illustrated in figure 2.2. Near the center of the trap, the magnetic field is approximately homogeneous and its magnitude grows linearly with distance from the center, where it is zero. In this configuration, this field minimum is located at $x = y = z = 0$ and coincides with the symmetry center between the coils. In BEC experiments, both the thermal cloud and the condensate are smaller than 1 mm and we can safely assume only the linear field region to be of interest. This scheme was first employed in 1985 to trap sodium atoms [Mig85].

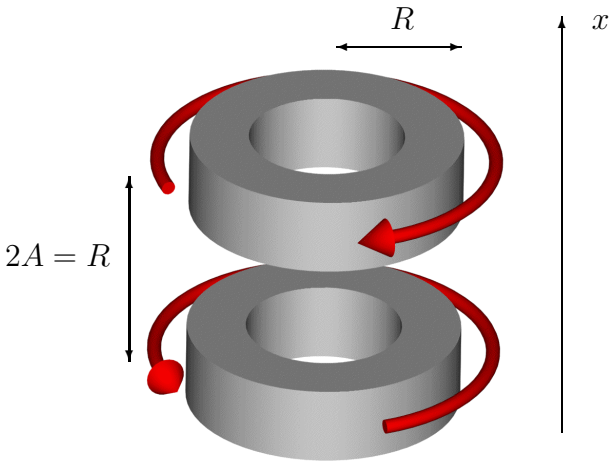

Figure 2.2: Coil configuration for a quadrupole trap. The direction of the current and spacing according to the Helmholtz configuration, $2A = R$, is indicated.

The linear potential is characterized by the magnetic field gradient given as

$$B_x = B'_x x, \quad B_y = B'_y y, \quad B_z = B'_z z. \tag{2.7}$$

Maxwell's equations demand the sum of the gradients to be zero and assuming rotational symmetry about the x–axis, this coincides with $B' \equiv -B'_x/2 = B'_y = B'_z$. Hence, the gradients in the y– and z–direction are half of that in x–direction. We obtain a spherical quadrupole field, which can be written as

$$\vec{B} = (-2x, y, z)B'. \tag{2.8}$$

There is no axial field component in the plane defined by $x = 0$ and no radial field component on the x–axis.

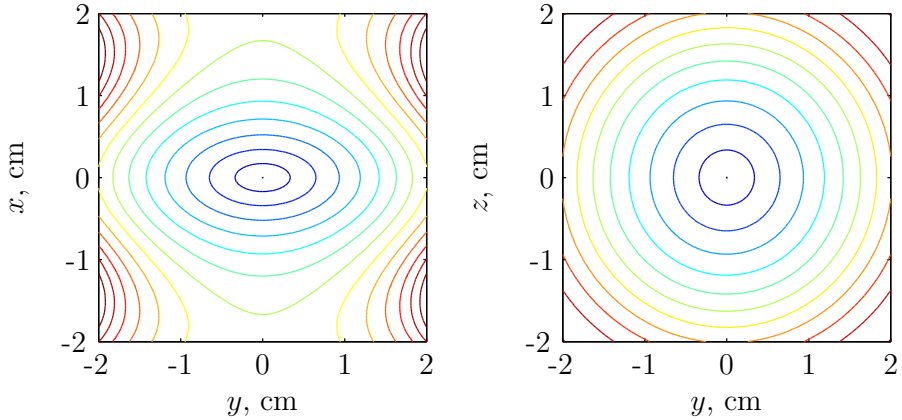

Figure 2.3: Field magnitude of the quadrupole trap in the x–z–plane on the left and along the symmetry axis (x) for a quadrupole trap in Helmholtz configuration. For coils with the radius $R = 3\,\mathrm{cm}$, spaced $A = 1.5\,\mathrm{cm}$, we obtain the shown symmetry, linear field variation near the trap center and a stronger gradient in the axial than the radial direction of the coil arrangement. Each contour line corresponds to a field increase of 0.5 G.

Figure 2.3 shows the field symmetry of the x–y–plane at $z = 0$ and centered on the symmetry axis cut at $x = 0$ in contour plots. The even spacing of the potential lines near the trap center illustrate the linearity of the field gradients. The left hand plot illustrates the difference in axial and radial gradient for the quadrupole trap: along the symmetry axis of the two coils (x–axis), the gradient is twice as large as along the radial direction. The right hand plot illustrates the radial symmetry along the rotation axis of the quadrupole coils.

Staying close to the Helmholtz configuration ensures strongest confinement as the linear gradient is maximized [Mig85].

For stable trapping and successful cooling, the following condition needs to be fulfilled: the atom only remains trapped if its magnetic moment follows the magnetic field adiabatically. The Larmor frequency must be large compared to the rate of field change so that

$$\frac{d\theta}{dt} \ll \omega_L = \frac{\mu_B |B|}{\hbar}. \tag{2.9}$$

An upper bound for the change of field rate $d\theta/dt$ is the trapping frequency, which is derived from the motion of the atom in the confining potential in equation (3.7) on page 24.

When cooling the atoms, they are forced towards the center of the quadrupole trap, where the magnetic field amplitude is zero. As equation (2.5) shows, the Larmor frequency even vanishes for areas of $B = 0$, so that the adiabatic following condition in equation (2.9) is violated. The orientation of the magnetic dipole moment is lost and the atoms can undergo a non–adiabatic transition to a non–trapped hyperfine state and are ejected from the trap. This transition in regions of low magnetic field is referred to as Majorana spin–flip [Maj32]. Atoms that are already cooled to lower temperatures are most likely to be lost, as they populate the bottom of the trap. Consequently, the quadrupole trap 'leaks' cold atoms - the cloud effectively heats up due to rethermalization. Various approaches have been applied successfully to stop this trap loss. The three most widely used solutions are:

1. With the **TOP** (Time–Averaged Orbiting Potential) trap, a rotating homogeneous bias field B_0 is added to the spherical quadrupole field. The frequency of the rotation must be larger than the orbiting frequency of the atoms, but much smaller than the Larmor frequency. The result is a harmonic potential that provides tight confinement [Pet95]. A TOP trap was used to create the first BEC at JILA [And95].

2. The **optical plug** makes use of optical dipole forces, and uses a tightly focussed and far blue detuned laser beam that forces atoms away from the trap center. Condensation of ^{23}Na was achieved using this technique at MIT in 1995 [Dav95].

3. The **Ioffe–Pritchard** (IP) traps originate from trapping schemes used for neutrons. They are characterized by a field minimum $B_{min} > 0$ and a harmonic potential near the trap center. They provide tight confinement for small clouds and feature large trap depths. The use for neutral atoms was first proposed by Pritchard [Pri84] in 1983 and IP traps are most

commonly used now. Details of this kind of trap are discussed in the following section 2.3.

2.3 Ioffe–Pritchard and QUIC trap

In the case of the quadrupole trap, the trapping potential rises linearly from the center of the trap, where the magnitude of the field is zero. As it is not possible to provide a non–zero magnetic potential with a linear field gradient, a harmonic potential is the tightest possible trapping potential that features a non–zero minimum. In the following, we consider a magnetic trap with a finite bias field along the z–direction and an axial field

$$B_z = B_0 + \tfrac{1}{2}B_z'' z^2. \tag{2.10}$$

In first approximation, the transverse field component B_x is linear

$$B_x = B' x. \tag{2.11}$$

If we now assume axial symmetry about the z–axis, applying Maxwell's equation yields a field configuration [Ber87] that can be written as

$$\vec{B} = B_0 \begin{pmatrix} 0 \\ 0 \\ 1 \end{pmatrix} + B' \begin{pmatrix} x \\ -y \\ 0 \end{pmatrix} + \frac{B_z''}{2} \begin{pmatrix} -xz \\ -yz \\ z^2 - \frac{1}{2}(x^2+y^2) \end{pmatrix}. \tag{2.12}$$

The minimum of the trap is located at $x = y = z = 0$, and the reference frame of the following equations is located around the potential minimum. The small thermal cloud or condensate, where[2] $k_B T < \mu_B B_0$, is subject to a three–dimensional anisotropic harmonic oscillator potential. Using $\rho^2 = x^2 + y^2$, the potential is given by

$$U = \mu_B B_0 + \frac{\mu_B}{2}\left(B_\rho'' \rho^2 + B_z'' z^2\right) + \mathcal{O}(x^3, y^3, z^3, x^2 y, x^2 z \cdots), \tag{2.13}$$

where

$$B_\rho'' = \frac{B'^2}{B_0} - \frac{B_z''}{2} \tag{2.14}$$

is the radial curvature.

All IP traps feature a non–zero minimum, but there are many possible coil configurations. A list and their basic properties can be found in the Varenna

[2]The magnetic moment μ of alkalis is on the order of a Bohr magneton μ_B, and for simplicity, we are using $\mu_B B_0$ for energy estimates.

School notes by Ketterle *et al.* [Ket99]. Most of these macroscopic trap arrangements dissipate many kilowatts of power, unless they are constructed with supra–conducting coils. They require high current supplies when built with ordinary copper wire. Cooling, stabilization and switching become problems and require creative solutions. Additionally, optical access to the atomic cloud as well as easy and reliable use are important considerations when designing a magnetic trapping apparatus. A special version of the IP trap, the QUIC trap, which consists of only three coils, provides successful solutions of these issues.

QUIC Trap

The QUIC (quadrupole–Ioffe–configuration) trap was introduced by T. Esslinger *et al.* in 1998. It is characterized by its simple build, easy use, and low power dissipation [Ess98]. Optical access to the MOT, thermal cloud, and condensate is achieved more easily and without loss of tight confinement. A schematic setup of the three–coil arrangement is shown in figure 2.4.

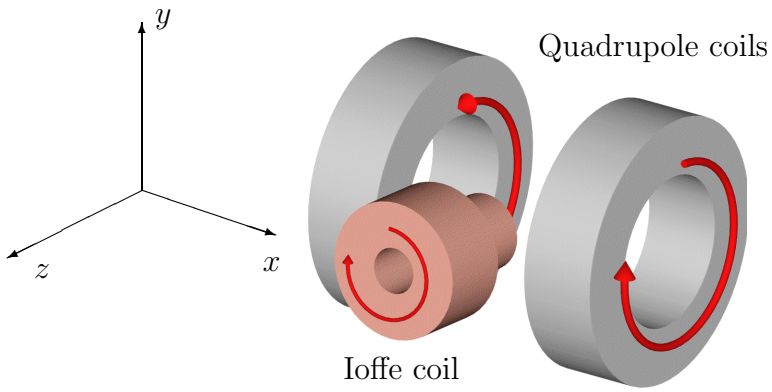

Figure 2.4: Coil configuration for a QUIC trap. The *axial* direction refers to the z–direction defined for the IP trap, which concurs with the symmetry axis of the Ioffe coil.

In this reference frame, the Ioffe coil is arranged along the z–axis, the quadrupole coils along the x–axis. The quadrupole field is produced with two coils running with opposite currents as described in section 2.2. In accordance with the mathematical expression derived earlier, the *axial* direction corresponds to the symmetry axis of the Ioffe coil, the z–direction in figure 2.4.

An important aspect for the successful implementation of an IP trap is the choice of bias field B_0. Its value is crucial in terms of reducing losses while

keeping tight confinement.

The different trapping potentials for varying offset fields are plotted in figure 2.5, adapted from Ketterle *et al.*[Ket99]. A large bias field softens the potential in the radial direction. An over-compensating bias field causes zero crossings and Majorana spin flips along the trap axis. With a correctly tuned field, there are no zero crossings and radial confinement is tight.

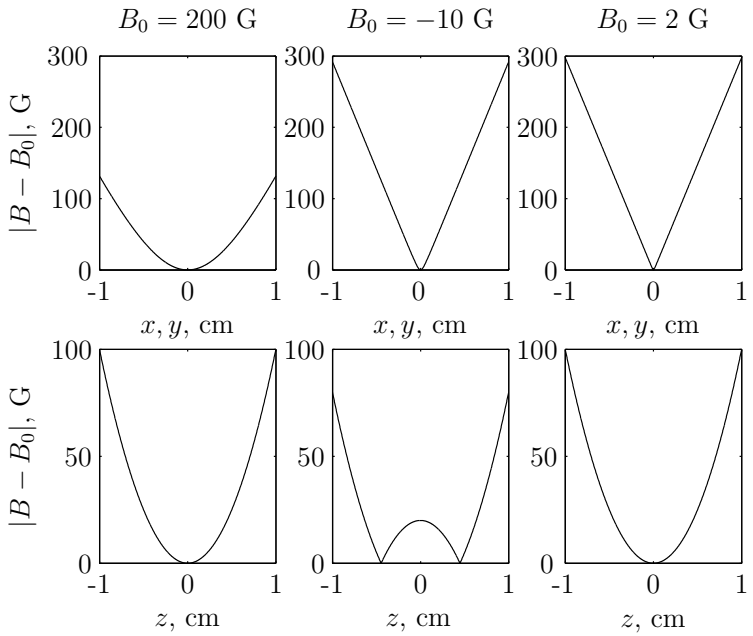

Figure 2.5: Bias field compensation is important for tight radial confinement in IP type traps. The illustrated magnetic field is characterized by a radial gradient of 300 G/cm, an axial curvature of 200 G/cm^2, and three different bias fields B_0. The upper row displays radial cuts, and the lower row axial cuts of the magnetic field profile. In the first column, radial confinement is softened as a result of the large bias field. The second column shows over-compensation by the bias field, resulting in two zero field crossings along the z-axis of the trap. In the third column, the bias field is tuned correctly, resulting in tight radial confinement and no zero field crossings. Adapted from [Ket99].

In the QUIC configuration, the confinement along z-axis is given by the field curvature of the Ioffe coil. The curvature scales with the current and radius of the coil as I/R^3. Therefore, if the Ioffe coil can be placed close to the center of the quadrupole coils, tight confinement can be achieved with small radii and moderately low currents.

Within the modelling task of the project, we observed the change of trapping potential when the quadrupole potential is slowly changed into the QUIC arrangement. Experimentally, this is done by running a current through the quadrupole coils only and then increasing the current through the Ioffe coil from zero. This has practical applications as a loading scheme. Details on this can be found in section 3.3 on page 27.

Chapter 3

Modelling of QUIC trap

The main challenge in designing and building an easy–to–operate magnetic trap for the use in BEC experiments lies in balancing considerations such as physical space, power dissipation, and optical access with the best possible trap parameters such as the axial curvature, radial gradient, corresponding trapping frequencies, and aspect ratio of the trapping potential at low magnetic fields.

During the course of the project the specifications of the physical space for the three coils changed tremendously. It evolved from the original idea to wind a small radius Ioffe coil from thin copper wire that would fit into a 1" diameter glass tube. This glass tube reaches into a vacuum chamber, ensuring close proximity between the coil to the center of a MOT arrangement, where the atoms are laser–cooled. Our results from the modelling revealed that the producible field parameters were well below our needs and expectations and the idea was therefore abandoned. Simultaneously, the ^{87}Rb atom source planned for this new experimental setup was found to produce a deviating velocity distribution, which put the feasibility of a Zeeman slower and described trapping arrangement in question.

Alternatively, a trap separated from the MOT and construction around a commercially available glass chamber (20 mm $\times$ 20 mm $\times$70 mm) is planned. The long direction is oriented horizontally. This arrangement is characterized by its flexibility, where loading schemes via magnetic transport over a succession of quadrupole coils [Gre01], a moving quadrupole trap [Lew03], or push beam [Woh01] can be implemented.

In the course of the project I developed a suitable code for modelling the coil arrangement of the QUIC trap. Nick Thomas, a senior PhD student at Otago at the time, provided partial MATLAB code he had previously written to calculate the magnetic field distributions of coaxial coils. All relevant code for modelling a QUIC trap is given in appendix A.

3.1 Magnetic field from a loop

All calculations are based on the idea of stacking up closed wire loops and adding up the magnetic field every single one produces at a certain point in space. The magnetic field $\vec{B}$ from a single perfect loop with radius R is calculated by integrating the vector potential $\vec{A}$ over the loop, and then applying $\nabla \times \vec{A} = \vec{B}$. The field components can be calculated according to Bergeman *et al.* [Ber87]. For a coil orientated along the z–axis, centered at $z = A$, and a current I, the field components are

$$B_z = \frac{\mu_0 I}{2\pi} \quad \frac{1}{[(R+\rho)^2 + (z-A)^2]^{1/2}} \quad \Big[K(k^2) + \frac{R^2 - \rho^2 - (z-A)^2}{(R-\rho)^2 + (z-A)^2} E(k^2)\Big], \tag{3.1}$$

and

$$B_\rho = \frac{\mu_0 I}{2\pi\rho} \quad \frac{z-A}{[(R+\rho)^2 + (z-A)^2]^{1/2}} \quad \Big[-K(k^2) + \frac{R^2 + \rho^2 + (z-A)^2}{(R-\rho)^2 + (z-A)^2} E(k^2)\Big], \tag{3.2}$$

and finally

$$B_\phi = 0. \tag{3.3}$$

Here, B_z, B_ρ, and B_ϕ are the axial, radial and azimuthal field components and μ_0 is the permeability of free space. Since we require axial field symmetry, there is no azimuthal field. K and E are the complete elliptic integrals with the argument

$$k^2 = \frac{4R\rho}{(R+\rho)^2 + (z-A)^2}. \tag{3.4}$$

These equations are used in the MATLAB function `b_loop_ex` to compute the magnetic field distribution far away from the origin. The conversion from cylindrical polar to Cartesian coordinates is performed with the function `coiloptions`.

3.2 Characteristic parameters

There are three degrees of freedom for optimizing the coil arrangement and output parameters with the restriction of a given wire diameter d and current I: the number of turns in each coil, their relative position, and the distance from the origin for the three coils.

Physically, the wire turns of a coil arrange as shown in figure 3.1. For simplicity, we use the indicated replacement picture and introduce an effective stacking distance in the radial direction of $s = \sqrt{3}/2 \cdot d$.

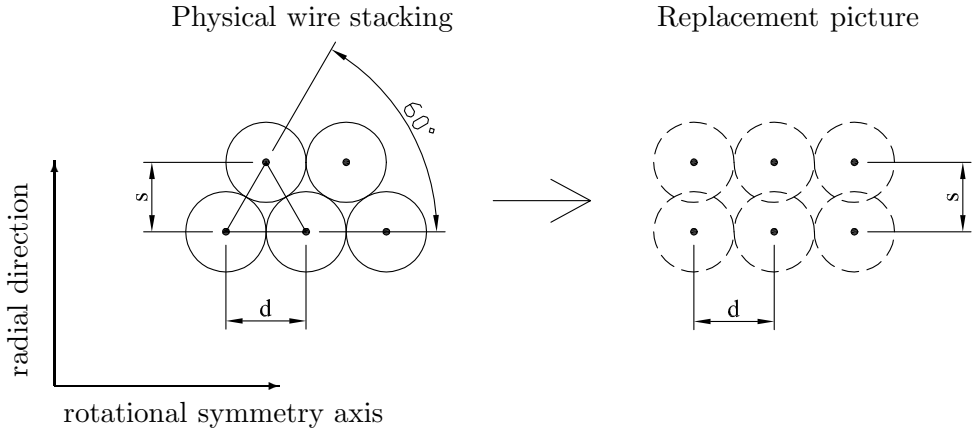

Figure 3.1: Illustration of the change in the radial wire stacking pattern used for magnetic field model. The left image shows the physical situation, where the turns in the radial layers slip in between the space formed by the underlying layer. The right image picture shows what is implemented into the code: the diameter of the wire d remains the wire–to–wire distance along the rotational symmetry axis of the coil, and along the radial direction, it becomes $s = d \sin 60\,^\circ$.

When designing the coil formers, the total height h of N turns in the radial direction is of interest. The height is calculated as

$$h = \left((N-1) \cdot \tfrac{\sqrt{3}}{2} + 1\right) \cdot d \tag{3.5}$$

where d is the true wire diameter. Experience has shown that using more than 7 layers of standard wire ($d \sim 2\,\mathrm{mm}$) when only the inside turns are in contact with a cooling surface, is not advisable as the coils are likely to overheat.

The magnetic field along each axis is treated in the harmonic oscillator model as described in section 2.3. Along the z–axis, we use the harmonic approximation given by equation (2.10),

$$B_z = B_0 + \tfrac{1}{2} B_z'' z^2, \tag{3.6}$$

so that the **axial curvature** B_z'' is related to the trapping frequency ω using $\mu_B B_z'' = m\omega^2$. A larger curvature corresponds to tighter confinement and we seek to maximize it, while keeping an offset field $B_0 \approx 1\,\mathrm{G}$. The **trapping frequency** ω is deduced for all three directions and the species in the trap, in our case ^{87}Rb. With $m_{Rb} = 1.44 \cdot 10^{-25}\,\mathrm{kg}$, the harmonic potential along z, for

instance, yields

$$U = \frac{1}{2}\mu_B B_z'' z^2 = \frac{1}{2} m_{Rb}\omega_z^2 z^2$$
$$\Rightarrow \omega_z = \left(\frac{\mu_B B_z''}{m_{Rb}}\right)^{1/2}, \tag{3.7}$$

where the value of the Bohr magneton is $\mu_B = 9.274 \cdot 10^{-24}\,\mathrm{J/T}$. Typical trapping frequencies are $2\pi \times 200\,\mathrm{Hz}$ in the radial (x and y), and $2\pi \times 20\,\mathrm{Hz}$ in the axial (z) direction.

The **power consumption** for the coils is calculated individually for each coil using

$$P = I^2 R = I^2 \frac{\varrho l}{Q}, \tag{3.8}$$

where $\varrho = 0.0175\,\frac{\Omega \mathrm{mm}^2}{\mathrm{m}}$ is the specific resistivity of copper at room temperature, I the current, and l the length of the wire. The length is extracted from the input parameters coil radius and number of turns. The cross sectional area of the wire diameter d is $Q = \pi(d/2)^2$. The power consumption is minimized and we anticipate a maximum of 500 W for all three coils combined, to be able to use only water cooling.

In the reference frame used for the coil arrangement in the MATLAB model, the Ioffe coil is arranged along the z–axis and the pair of quadrupole coils along the x–axis. The origin of this reference frame is located at the center between the quadrupole coils. The position of the potential minimum of the QUIC trap is axially displaced towards the Ioffe coil by $\hat{z}$. We use fit functions around this minimum to extract the characterizing parameters introduced in this section. The **position of the minimum**, $\hat{z}$, along the z–axis of the trap is of interest in order to provide optical access to the condensate through the quadrupole coils. It can be influenced by allowing for a higher bias field and in return decreasing confinement.

The radial gradient near the trap center is derived from a Taylor expansion to second order, so that with $\rho^2 = x^2 + y^2$

$$B = B_0 + \frac{1}{2}\left(\frac{B'^2}{B_0} - \frac{B_z''}{2}\right)\rho^2 + \frac{1}{2}B_z'' z^2, \tag{3.9}$$

and

$$B_\rho'' = \frac{B'^2}{B_0} - \frac{B_z''}{2} \Rightarrow B' = \sqrt{B_0\left(B_\rho'' + \frac{B_z''}{2}\right)}, \tag{3.10}$$

where B_0 the bias field, B_z'' the axial curvature, and B_ρ'' the radial curvature. The radial gradient B', which corresponds to the **stiffness** of the trap, is strongly influenced by the choice of bias field B_0 as illustrated in figure 2.5 on page 18.

The **anisotropy**, or **aspect ratio**, λ, of the atomic cloud inside the trap is of interest, because the radial curvature is usually substantially larger than the axial curvature. Accordingly, the atomic cloud is cigar–shaped with the long axis along the trap's z–axis. The aspect ratio scales as

$$\lambda = \sqrt{\frac{B_\rho''}{B_z''}}. \tag{3.11}$$

Since evaporative cooling becomes more effective with a moderately, not too large aspect ratio, we target a value $7 \leq \lambda \leq 12$.

The **geometric mean trapping frequency** is given by

$$\bar{\omega} = (\omega_x \omega_y \omega_z)^{1/3}, \tag{3.12}$$

and is a figure of merit for the trap, since the collision rate needed for evaporation increases proportional to $\bar{\omega}$ due to adiabatic compression [Ket99].

3.3 Computational results

The proposed coil arrangement is designed with the intention to allow optical access to the field minimum both through the Ioffe coil and through the quadrupole coils. This allows probing of the condensate both in the vertical and the axial direction, and gives about 300 ° access in the y–z–plane. Optical access to the origin of the reference frame, which is located at the center of the quadrupole coils, is easily implemented, as the x–axis coincides with the symmetry axis of the quadrupole coils. The schematic coil arrangement in figure 3.2 shows a cut at $y = 0$. The final trapping potential is shown in figure 3.3. It shows the axial magnetic field over a large region on the z–axis. The field produced by the quadrupole coils and the Ioffe coil are shown individually as well as the sum of both for a current of $I = 25\,\mathrm{A}$ through all three coils and a wire diameter $d = 1.2\,\mathrm{mm}$. The non–zero minimum is illustrated in the inset.

The output parameters and results of the MATLAB model of the presented coil arrangement are summarized in the following table. Details and photographs of the constructed setup can be found in chapter 4.

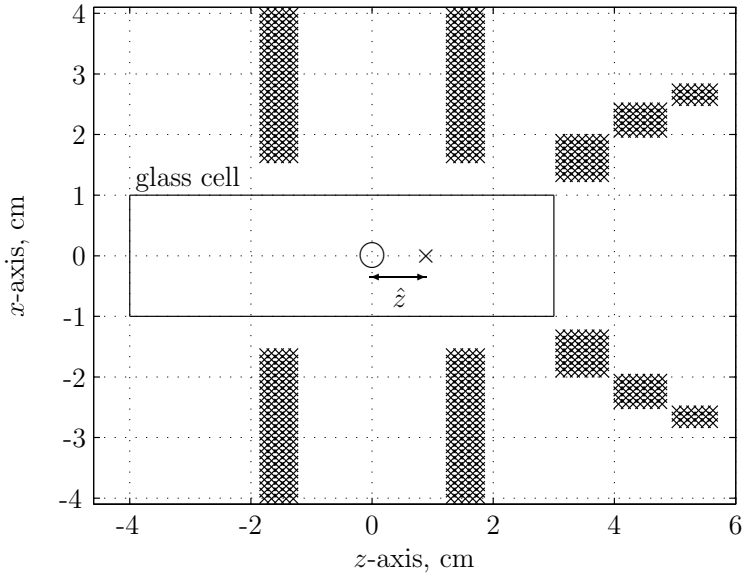

Figure 3.2: Cross section schematic of computed coil arrangement for QUIC trap cut at $y = 0$. The origin of the reference frame (◯) and the approximate position of the magnetic field minimum (×) are indicated. The position and size of the glass cell is shown. The copper wire turns of diameter $d = 1.2\,\mathrm{mm}$ are marked. The wire turns are stacked along their respective radial direction as indicated in figure 3.1.

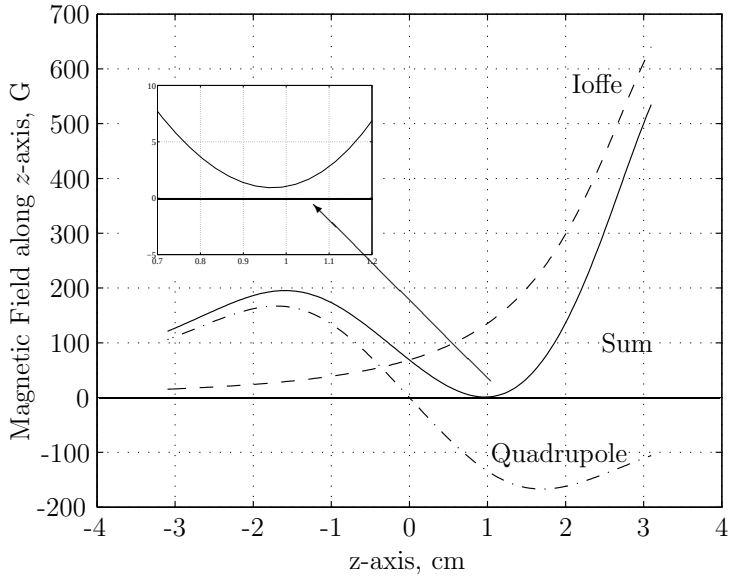

Figure 3.3: The magnetic field component of Ioffe coil field, quadrupole field, and their sum is shown for $I = 25\,\mathrm{A}$. The inset illustrates the non–zero minimum ($B_0 = 0.93\,\mathrm{G}$ at $\hat{z} = 0.96\,\mathrm{cm}$) of the QUIC configuration.

Bias field	$B_0 = 0.93\,\mathrm{G}$
Axial curvature	$B''_z = 204\,\mathrm{G/cm^2}$
Radial gradient	$B'_\rho = 147\,\mathrm{G/cm}$
Location of field minimum from origin	$\hat{z} = 0.96\,\mathrm{cm}$
Total power dissipation	$P = 422\,\mathrm{W}$
Aspect ratio	$\lambda = 10.70$
Trapping frequencies	$\omega_r = 194.8 \times 2\pi\,\mathrm{Hz}$ $\omega_z = 18.3 \times 2\pi\,\mathrm{Hz}$
Geometric mean trapping frequency	$\bar{\omega} = 88.5 \times 2\pi\,\mathrm{Hz}$

Table 3.1: Output parameters of computed coil arrangement.

The **Ioffe coil** has a total of 102 turns, which vary in radius between 13 mm and 27.6 mm. The coil dissipates 124 W. It is located 31.07 mm from the center of the quadrupole coils. The **quadrupole coils** consist of 160 turns each. The smallest turn has a radius of 13 mm, and the largest turn a radius of 17.8 mm. Each coil dissipates 149 W and the coil–to–coil distance is 32.2 mm (or origin to first turn 16.1 mm).

Transition to the QUIC configuration

We studied in detail how the trapping potential changes from the simple quadrupole to the QUIC trap when the current through the Ioffe coil is slowly increased at a fixed quadrupole current. This method finds experimental application in loading schemes from a Magneto–Optical trap (MOT) that contains pre–cooled atoms. Figure 3.4 displays the axial field magnitude and 3.5 shows the changing shape and position of the trapping potential in contour plots.

Figure 3.4 illustrates the magnetic field of the simple quadrupole trap along the z–axis that merges with a second magnetic field minimum, which is generated by the Ioffe coil, for increasing currents. In the process, the minimum moves along the axis towards the Ioffe coil and is lifted to non–zero field values[1].

Figure 3.5 shows the process of the two merging magnetic field minima in contour plots for views at $y = 0$, which corresponds to a view from the top, and a cut at $x = 0$, the view through the quadrupole coils. In the first row of

[1]The non–zero minimum is shown explicitly in figure 3.3.

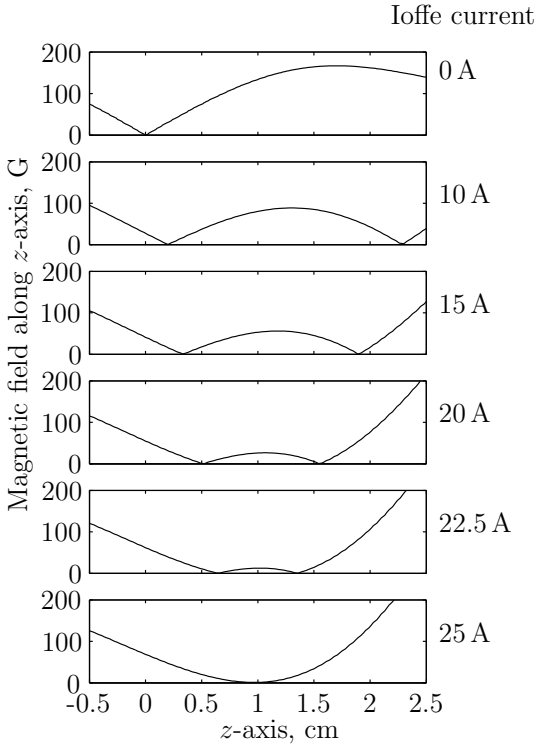

Figure 3.4: The magnetic field along the z–axis changes from the quadrupole to the QUIC configuration for increasing currents through the Ioffe coil. The current through the quadrupole coils is fixed at 25 A.

pictures, a current of $I = 25\,\mathrm{A}$ runs only through the quadrupole coils. This produces a cone–shaped quadrupole field with a field minimum at zero as laid out in section 2.2 on page 13.

In the second row of plots, the current through the Ioffe coil is increased to 10 A. On the side where the Ioffe coil is positioned, a second quadrupole potential is forming on the symmetry axis of the Ioffe coil (z–axis). It appears due to combination of the field gradients of the quadrupole and Ioffe configuration. It is visible in both plots that the long axes of the two potential minima are perpendicular to each other. For further increasing currents, the two potential minima merge and the overall cigar–shaped minimum is lifted up to $B_0 \approx 1\,\mathrm{G}$ as illustrated in figure 3.3 on page 26.

The series of contour plots along the vertical axis in the left hand column display a Y–shaped potential for currents between 20 and 25 A. These trapping instabilities occur because the radial gradient is cancelled by the axial curvature [Ket99]. One needs to consider atoms escaping the trap at a certain axial displacement over the threshold. Since the objective is to trap laser–cooled

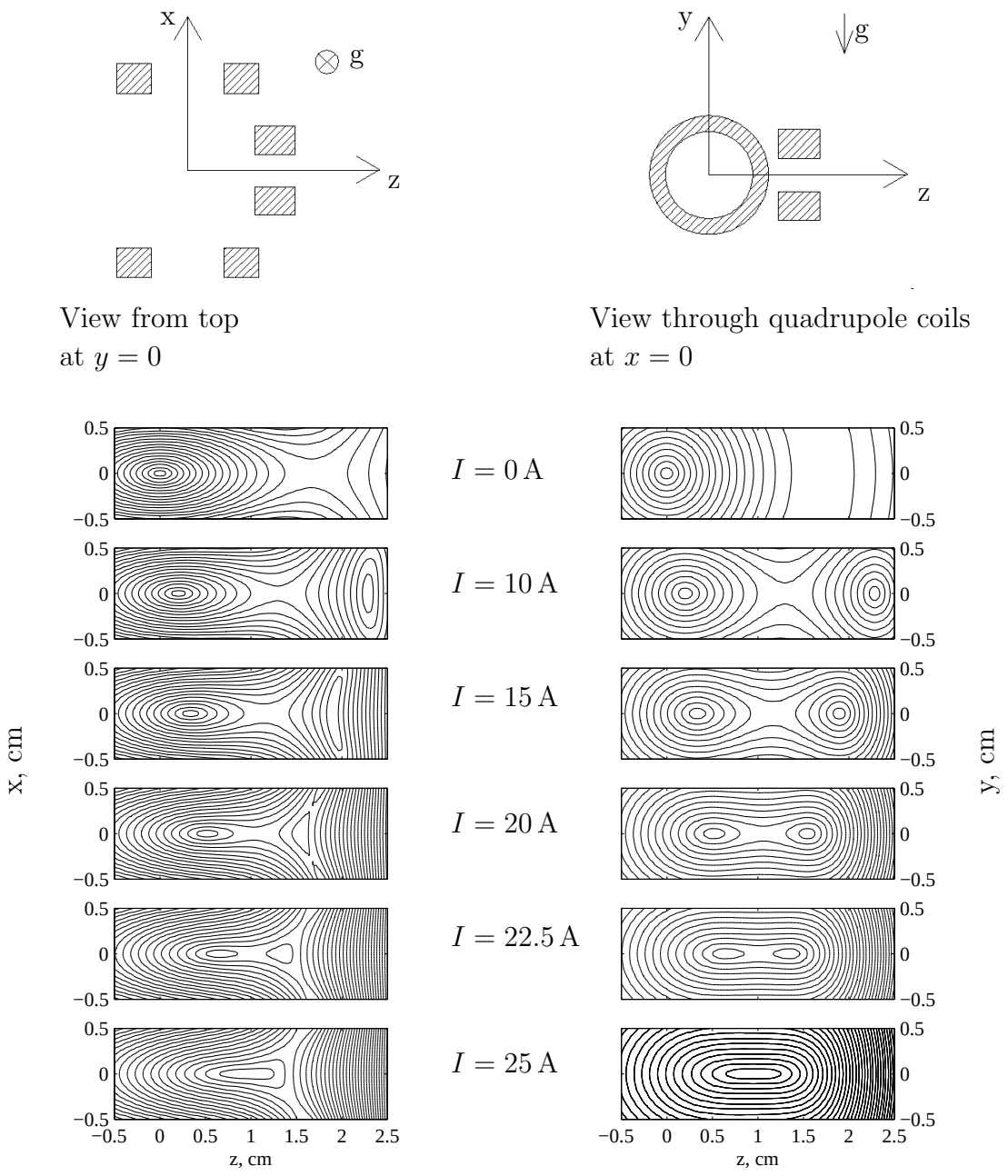

Figure 3.5: The trapping potential changes from the quadrupole into the QUIC configuration. With a steady current through the quadrupole coils of 25 A, the current through the Ioffe coil is gradually increased as indicated. We observe the transition cut at $y = 0$ (left) and cut at $x = 0$ (right). Each contour line corresponds to an increase of 10 G in the magnetic field amplitude.

atoms, the barrier indicated by the contour lines is too high for the atoms to escape.

For the transition from the quadrupole to the Ioffe configuration, the gradient of the quadrupole field decreases along the x–axis and increases along the y–axis. Additional radial compression is not necessary. The potential displayed in the last rows of both figures 3.4 and 3.5 correspond to the final modelling result presented in this section.

Chapter 4

Experimental implementation

All coil formers and parts of the mounting system were constructed in the Mechanical Workshop in the Physics Department at Otago by Peter Stroud. They are made from aluminum alloy and all screws and bolts are, apart from plastic water fittings, metric. The copper wire used for winding the coils is insulated with an enamel coating and has a nominal outer diameter of 1.2 mm. The coating is reasonable sturdy, but scrapes off easily when in contact with sharp objects. All corners and edges of the formers are therefore carefully polished with metal files and fine sandpaper. Edges in direct contact with the wire are covered with Kapton tape, a high performance polyimide film that withstands high temperatures and is backed by a silicone adhesive. The space between the copper wires is filled up with heat–conducting silicone paste to improve heat transport.

For the electrical connection, we use silver plated copper crimp contacts and single pole housings. They are approved for use up to currents of 30 A. Concerns over magnetic field switching stability dictate that the three coils should be connected in series. The one DC power supply available to us is from Agilent (Model E4356A) and delivers a maximum current of 30 A at up to 70 V. The laboratory features the necessary single phase outlet. We plan to use a maximum current of 25 A. The lack of a second power supply bears the disadvantage that the changeover from the quadrupole to the QUIC potential, which can find application as a loading scheme, illustrated in figure 3.5, can not be verified in scope of this thesis.

4.1 Magnetic field coils

The **Ioffe coil** follows the design of formers previously constructed at Otago. A schematic cross section and photographs are shown in figure 4.1 on page 33.

The wire is wound onto a piece of aluminum alloy which has been hollowed out to allow water flow within. The former features three different sections separated by disks. Towards the origin of the reference frame, the radius of the wire turns decreases, as the turns further away from the point of interest at the origin only contribute to the magnetic field if their radius is sufficiently large. A slit along the axial direction prevents eddy currents when the current is turned off suddenly, as will be the case when conducting expansion of condensates for time–of–flight (TOF) measurements. The slit widens towards the radial center and allows almost 6 mm of optical access along the z–axis as can be seen in figure 4.1.

In order to provide a large diameter hole to access the condensate vertically along the y–axis, the **quadrupole coils** are designed differently: the water–cooling is constructed to be on the outside of the former. This means that the outer turns of the coil, rather than the smaller ones on the inside, are indirectly water–cooled. The coil is wound onto a separate former, which is shown in figure 4.2 on page 34. A hollow tube is constrained by a disk in the front and back to prevent the wire slipping off. The center disk shown in the photograph in figure 4.2 is intended to improve the heat flux by providing an increased amount of contact area to the aluminum. It was removed during the winding process as it was impossible to wind a coil over two sections that would slide into the retainer without damage. At the cross–over point from one section to the next, the wire would protrude beyond all the other wire layers and the limiting disks on either side by approximately 1/4 mm. The insulation was rasped off the wire and coil was short–circuited.

The former fits tightly into the second piece, the retainer, which is shown in figure 4.3. It allows a water–flow around the former and prevents it from sliding after assembly. Both the former and the retainer are equipped with slits preventing eddy currents.

All coils are wound on a turning machine that ensures the wire is under tension at all times. For the first turn, a sharp 90 ° angle is formed with a well padded tool to force the wire to run parallel to the confining disk. The first layer is generously covered in heat–conductive paste and it is added whenever appropriate. The last 1 1/2 turns are glued to the underlying layers using TorrSeal. This vacuum approved two–component epoxy is solvent–free and can be used at temperatures up to 120 °C. For a full cure, the coils are left to dry at room temperature for 24 hours.

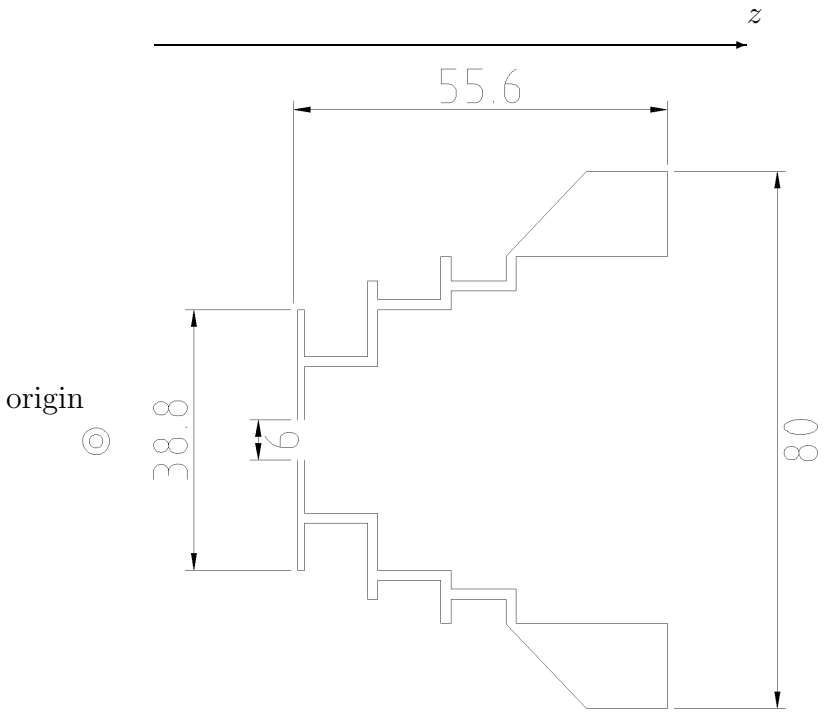

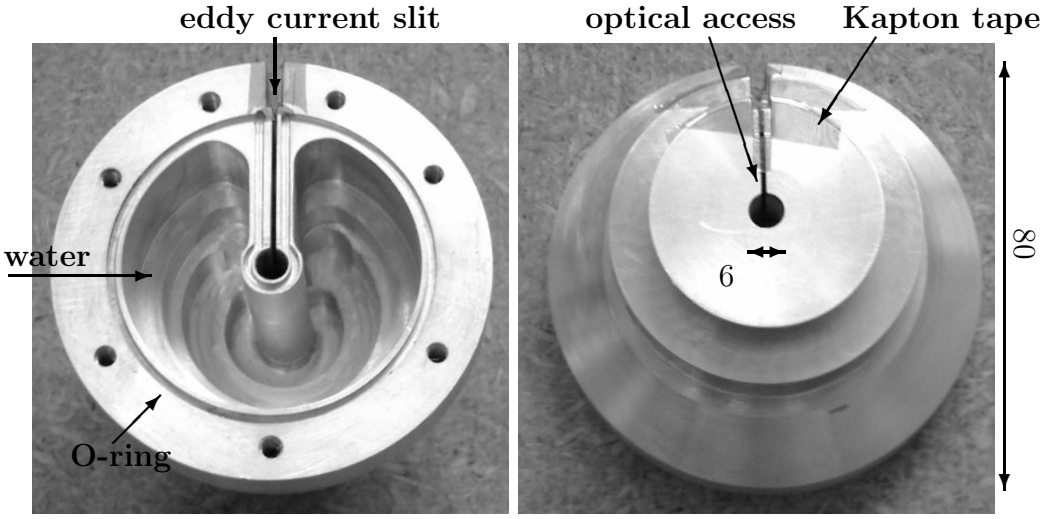

Figure 4.1: Schematic cross section, back and front view photograph of the Ioffe coil former. Eddy current slit, optical access, and dimensions are indicated. The origin relates to the center of the quadrupole coils. All dimensions in mm.

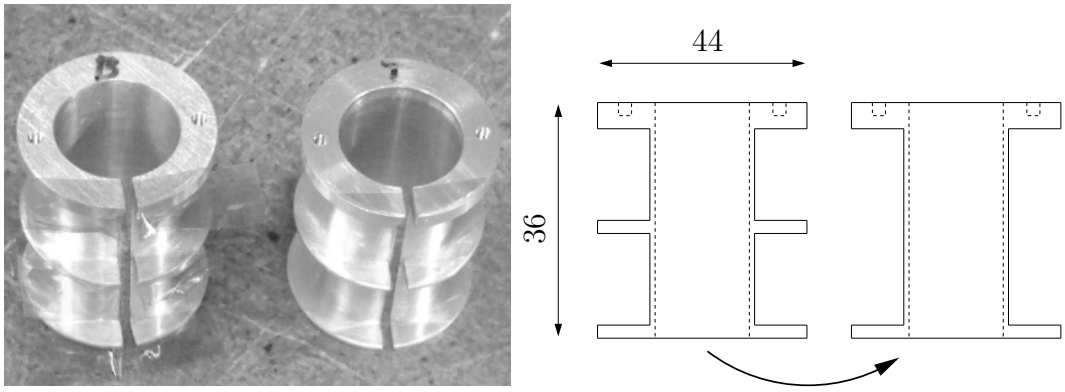

Figure 4.2: Former for the quadrupole coils. The photograph shows how the Kapton tape is applied to the edges only. 'B' and 'T' denote bottom and top coil. The schematic cross section shows the removal of the dividing disks. All dimensions are given in mm.

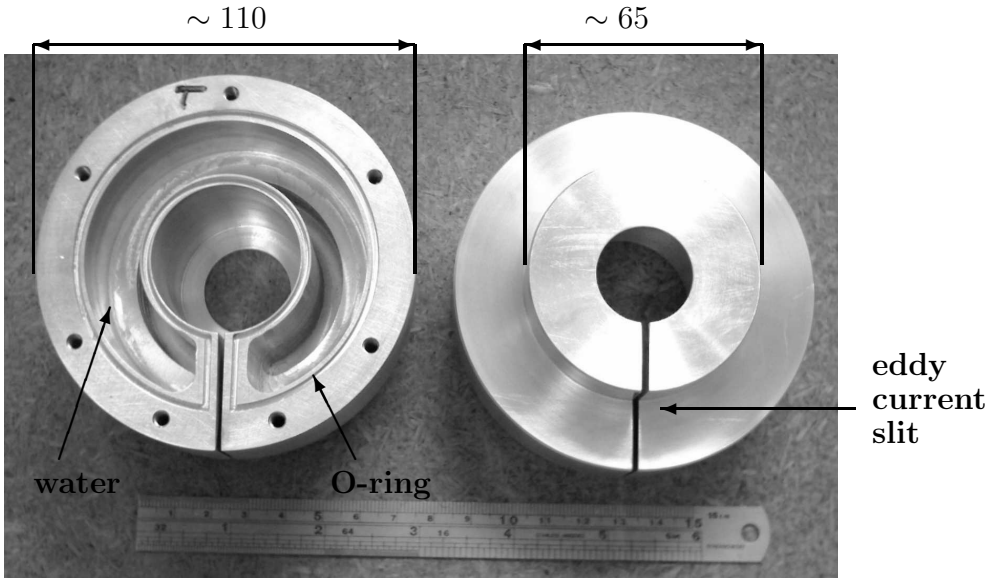

Figure 4.3: Retainer for quadrupole coils in an inside and outside view. The inner section that accommodates the former measures ∼ 39 mm across, the outer diameter of the lid side ∼ 110 mm. The groove for the rubber O–ring is indicated. The ruler in the bottom of the picture measures 170 mm. All dimensions are given in mm.

4.2 Mounting System

The mounting system can be seen on page 36. It is designed with the objective to provide an arrangement insusceptible to shocks caused by both mechanical influences and the current running through the coils. The compact mounting design of the quadrupole coils allows maximum optical access. All parts of the mounting system are constructed from (sandblasted) aluminum alloy. Care is taken to not block the optical access and only add solid pieces of aluminum where no eddy currents can develop.

The mounting of the Ioffe coil allows it to be moved in vertical direction with a clearance of ±5 mm. In accordance with the typical beam height in the lab, the optical access is positioned 15 cm above the optical table. The lid of the coil is securely attached to the vertical piece of the mount. The base plate of the Ioffe coil mount rests on the laser table. The base plate can be moved closer towards the origin, but its movement is controlled by the U–formed base plate on which the quadrupole coils are attached.

The bottom quadrupole coil is secured on a plate and four pegs. The plate is equipped with appropriate clearings preventing eddy currents and providing optical access from below the trap. For adjustment of the height of the coil, the pegs can be removed and re–machined. The top quadrupole coil is suspended by a pair of legs and arms. The legs are the vertical bars, the arms the horizontal ones as marked in figure 4.4. The width of the arms can be adjusted to change the total height of the coil with respect to the bottom coil and laser table.

4.3 Water–cooling

All three coils are closed with plane aluminum alloy lids secured with multiple screws to the formers and retainers. Rubber O–rings close the coils water-tight. The grooves cut for the O–rings are visible in figures 4.1 and 4.3. They surround the water carrying volume. The edge that supports the O–ring is only a few millimeters thick, and therefore challenging to machine. Angled plastic water fittings connect the coils to a high pressure water supply with $1/4''$ plastic tubing. The threading of the water fittings are covered with sealing Teflon tape. The water enters and exits the formers in close proximity to the eddy–current slits to create a large water flux and provide best possible cooling.

A distribution system made from a single aluminum block was planned but not finished within the time of the project. Filtered water will be piped to the laser table in one 12 mm tube, so that each coil is equipped with an

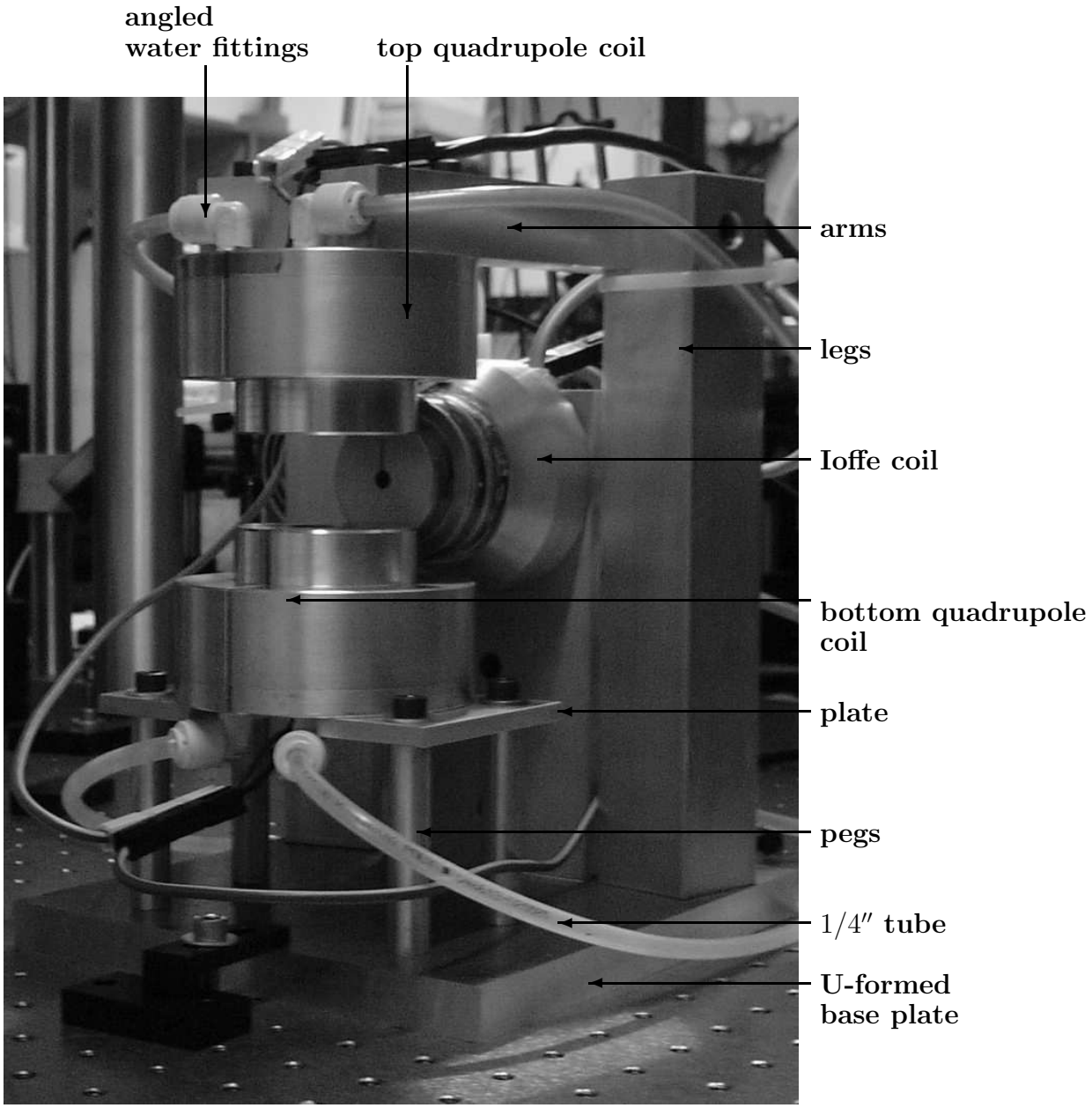

Figure 4.4: Mounting system of constructed QUIC trap with quadrupole coils in the foreground and Ioffe coil in the background. Note that the reference frame has been rotated for constructional reasons. The symmetry axis of the quadrupole coils is oriented vertically.

individual circuit that can be locally interrupted. This facilitates effective and safe cooling and allows sufficient flexibility to position all tubing away from optical access to the trap.

Temperature performance of coils

All three coils heat up with higher current flow. The performance of the (low pressure and provisional) water–cooling is tested for current induced temperature increase. As a precaution, the current is only ramped up to 20 A and interpolation performed for larger values. The surface temperature of the formers should not exceed 75 °C.

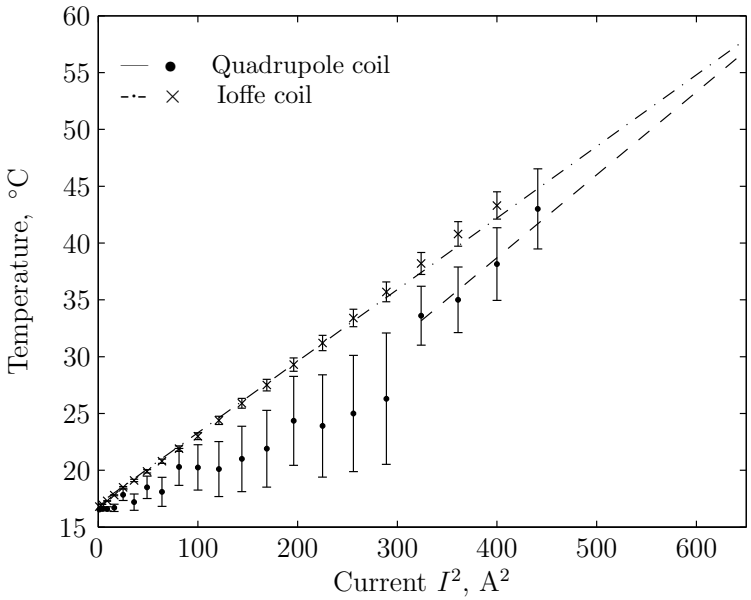

Figure 4.5: Measurement results for surface temperature dependence with increasing currents I^2. Data for the Ioffe and one quadrupole coil is shown. The quadrupole data points at currents up to $\sqrt{300}$ A remain disregarded, as we are interested in the maximum surface temperature. The data points at higher currents are averaged over multiple probe positions. The linear approximations shows the surface temperature to remain below 60 °C when extrapolating to $(25\,\mathrm{A})^2 = 625\,\mathrm{A}^2$.

The temperature probe, which consists of a two–metal contact, is attached to the hot regions of the formers using heat conducting silicone paste. For the Ioffe coil, this is the wire itself in the region where the largest number of coil turns is stacked. In the case of the quadrupole coil, we placed the probe halfway into the center clearance, which is the location furthest away from

the water–cooling and closest to copper wire turns. The system is allowed to thermalize for 2 minutes at each current value.

Figure 4.5 illustrates the result for the coils. As the power consumption scales with $P = I^2R$, we choose a linear display and can extrapolate, assuming constant cooling performance with the high–pressure water supply, to a maximum surface temperature of 60 °C at 25 A for all three coils. The performance of the water–cooling is satisfactory.

Chapter 5

Verification of magnetic field

We measure the axial magnetic field of the quadrupole coils and the Ioffe coil individually and compare them to the modelled values. The results corroborate the model of the QUIC trap, but due to time constraints, the resulting overall magnetic field of the QUIC arrangement could not be verified. The field is mapped with a Gauss meter. The Hall probe is embedded near the tip of the approximately 20 cm long probe stick shown in figure 5.1. The stem is attached to a translation stage.

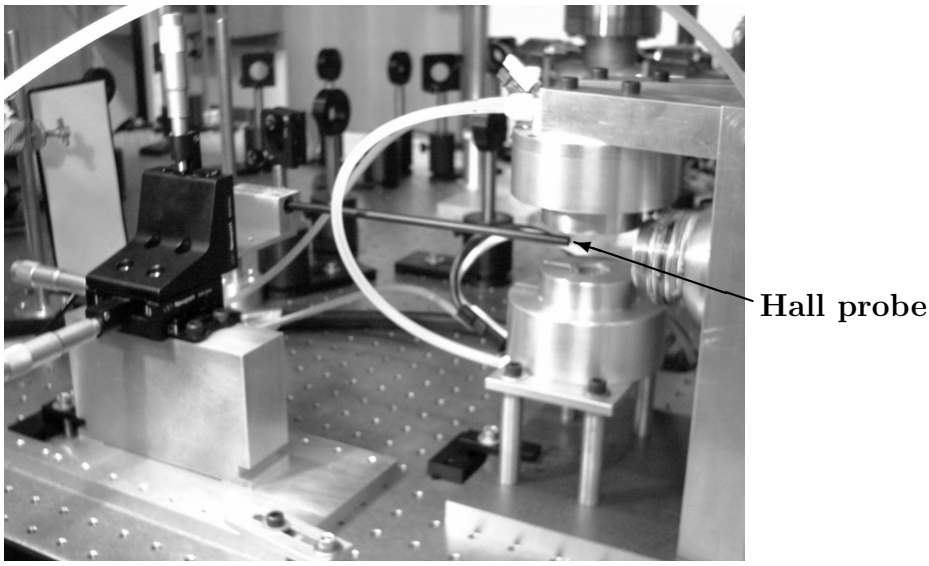

Figure 5.1: Setup for field verifying measurements showing the mounted constructed coils and Hall probe on a translation stage.

5.1 Ioffe coil field

For the measurement of the Ioffe coil field, the probe is carefully adjusted along the symmetry axis of the coil. The total range of one data set is limited by the scope of the translation stage in the horizontal direction. The result of a typical measurement is shown in figure 5.2. For orientation, the Ioffe coil is positioned on the far right hand side of the figure and the z–axis zero corresponds to the center of the quadrupole coils. The distance a_1, measuring from the origin to the first turn of the Ioffe coil, is the free parameter when comparing the measured values with the computational model. Analysis of the data using the model delivers a value of $a_1 = (32.8 \pm 0.3)\,\mathrm{mm}$. In the range of interest on the z–axis from 0 to 2 cm, the deviation in the magnetic field amplitude is less than 4 %.

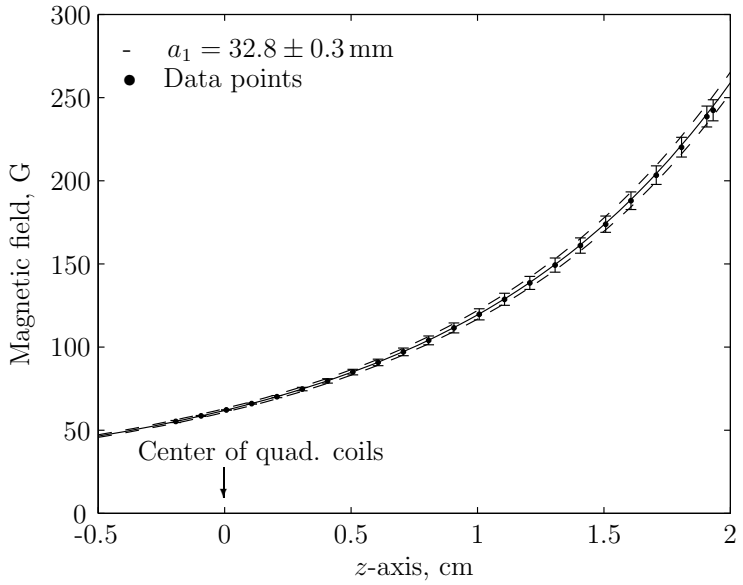

Figure 5.2: Measurement results of the axial magnetic field of the Ioffe coil. The z–axis zero corresponds to the origin of the frame of reference, hence the center of the quadrupole coils. The data shows good agreement for the given a_1, the origin to first turn distance.

On the physical setup, we measured a_1 using calipers, and obtained $a_1 = (31.7 \pm 0.8)\,\mathrm{mm}$ bearing a comparably large error, which is composed of the uncertainty of the position of the Hall probe inside the stem, $\delta = (0.38 \pm 0.25)\,\mathrm{mm}$, and the position of the first turn of the coil on the former. When assuming the overall shift of the data points on the z–axis to be on the order of $\pm 1\,\mathrm{mm}$, we find that the level of consistency concerning the magnetic field values in the

range of interest is not altered. The modelled curves are shifted along the axis accordingly. Errors arising from moving the measuring probe in a slight angle off axis are allowed for by an estimated uncertainty in the magnetic field value, which is shown in figure 5.2. For completeness, we measured the resistance of the Ioffe coil to be $(1.41 \pm 0.08)\ \Omega$, and the inductance $(130 \pm 2)\ \mu$H. The inductance is of interest when testing the turning–off behavior of the coils and estimating the induction voltage.

5.2 Quadrupole field

For the measurements of the gradient produced by the quadrupole coils, the two formers are carefully lined up as shown in figure 5.1. The measurements are performed at a fixed spacing of the coils $2a_2$, where, in accordance with the model, a_2 is the distance from the origin to the first turn of each coil. The result is shown in figure 5.3.

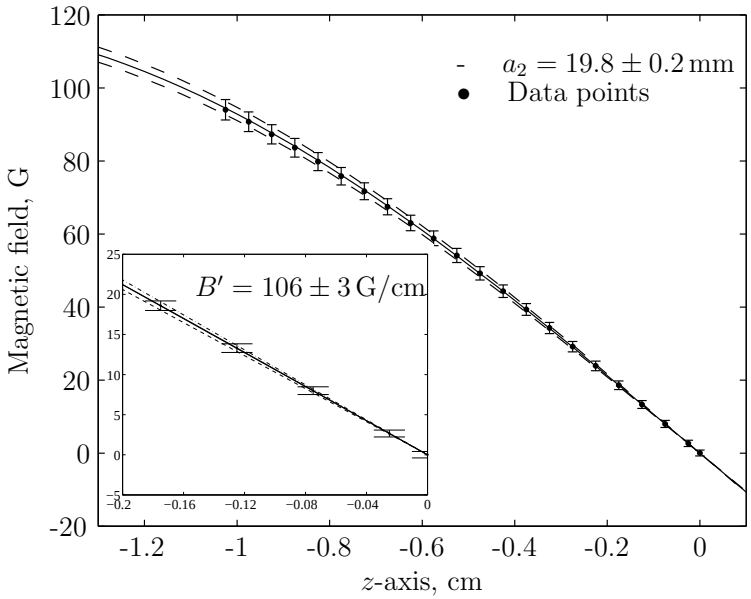

Figure 5.3: Measurement results of the axial magnetic field of the quadrupole coils. The data shows good agreement over the measured range for the given a_2, which is the distance from the origin to the first turn of each coil. The inset illustrates the linear gradient of 106 ± 3 G/cm near the center.

Analysis of the data using the model delivers a value of $a_2 = (19.8 \pm 0.2)$ mm. Near the center, this corresponds to a linear gradient of $B' = (106 \pm 3)$ G/cm,

which was introduced in section 3.2 on page 22. We take into account non–perfect alignment of the coils by introducing an estimated uncertainty of the magnetic field value shown in figure 5.3.

On the physical setup, a_2 is measured to be $a_2 = (17.9 \pm 1.5)\,\mathrm{mm}$. This value includes the physical spacing of the two coils, and takes into account a rough approximation of the position of the first turn inside the former. The deviation from the physical spacing to the fitted result amounts to approximately 10 %, which is well within the expected deviation.

To verify whether the two quadrupole coils deliver equivalent field strengths, we measure the resistance of the coils using a low precision current of 1 mA, so that heating effects can be neglected. We find the difference to be on the same order as the measurement uncertainty, when taking fluctuations caused by connecting leads into account. The top coil has a resistance of $(0.51 \pm 0.08)\,\Omega$, the bottom one $(0.61 \pm 0.08)\,\Omega$. The inductance of the coils amounts to $(293 \pm 2)\,\mu\mathrm{H}$ for the top and $(292 \pm 2)\,\mu\mathrm{H}$ for the bottom coil, respectively. These encountered differences are well within the expected deviation for hand–made coils, where the total wire length is expected to have an error on the order of 2 %.

In conclusion, the reported deviation from the modelled to the measured magnetic field distribution are within the expected range.

Chapter 6

Conclusions

In the first part of this thesis, the construction of a QUIC (quadrupole–Ioffe–configuration) magnetic trap is documented. The related theoretical background for trapping neutral ^{87}Rb atoms, and the fundamental theory of quadrupole and Ioffe–Pritchard traps was given along with the computational results delivered by a MATLAB code, which was developed within the scope of the project. The coils built based on the computational results were described and measurements verifying the performance of the coils were shown. The largest deviations encountered are below an acceptable value of 10 %. This leads to satisfactorily agreement for the magnetic field properties. The coil arrangement design allows for flexible use and is delivered with a compact mounting and water–cooling system, which both need minor mechanical work (e.g. hollowing out the bottom of the mount's base plate for secure positioning) and implementation of safety provisions concerning the cooling circuit.

The trapping frequencies for ^{87}Rb should be verified as soon as the vacuum system, atom source, MOT cloud, and loading scheme are developed. The coil arrangement needs to be tested for both magnetic field stability and switching properties, before it can be used in the second BEC experiment at the "Ultracold Atoms Research" Group at the University of Otago, New Zealand.

Part II

Frequency stabilization of a ring cavity laser Innsbruck, Austria

Chapter 7

Introduction

When a Bose–Einstein condensate (BEC) is confined in a three–dimensional optical lattice potential, the Hamiltonian of the appropriate theoretical model yields two possible ground states of the system: in the superfluid limit for small lattice depths, the atoms are delocalized over the entire lattice potential and a single macroscopic wavefunction describes the system. In the Mott insulating limit for large lattice depths, the strictly localized atoms are described by Fock states, and overall coherence is lost. The Mott transition describes the reversible change from the superfluid to the insulating state.

Experimentally, the three–dimensional optical lattice potential is implemented with three retro–reflected, red–detuned laser beams. To observe the Mott transition, the potential depth of the periodic lattice is adiabatically increased. Figure 7.1 shows the arrangement of the six laser beams and the resulting optical lattice.

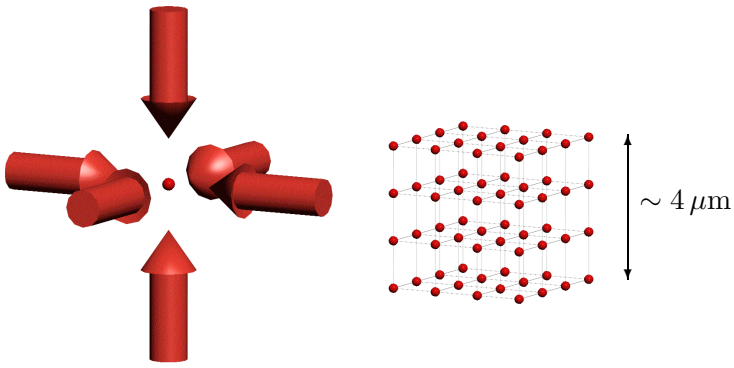

Figure 7.1: Schematic of optical lattice beams and BEC on the left, and the resulting three dimensional optical lattice potential with occupied lattice sites on the right for a wavelength of 830 nm.

Performing experiments with Mott insulators is currently one of the focal points in the research field of ultracold bosonic quantum gases. Pioneering proposals involving ultracold gases in periodic potentials were made by the group of P. Zoller in Innsbruck in 1998 [Jak98] and the transition was first observed by the group of T. Hänsch and I. Bloch in Munich in 2002 [Gre02] with a BEC of ^{87}Rb.

So far, experimental work performed with Mott states includes measurements of the excitation spectra of both the superfluid and Mott insulating state [Gre03], coherent transport of atoms in the lattice [Man03a], controlled collisions and entanglement [Jak99, Man03b], as well as the realization of a strongly interacting Tonks–Girardeau gas [Par04, Kin04], to name only a few. Mott insulators constitute a starting point for the formation of deeply bound Rb_2 molecules. By placing two atoms per lattice site, the molecule transition can be performed using magnetically tunable Feshbach resonances [Don02] or photoassociation [Wyn00]. The use of optical Raman transitions to transfer these highly vibrational state molecules into low vibrational states has been proposed. Using these deeply bound molecules with sufficiently small collision rates, a molecular BEC can be produced by "melting" of the insulator [Jak02]. Furthermore, proposals have been made to employ the atomic lattice crystal for quantum information processing [Cir04].

In the scope of a visiting stay at the "Ultracold atoms and quantum gases group" of Prof. Dr. Rudolf Grimm at the University of Innsbruck, I implemented a scheme to frequency–stabilize the laser producing the optical lattice potential.

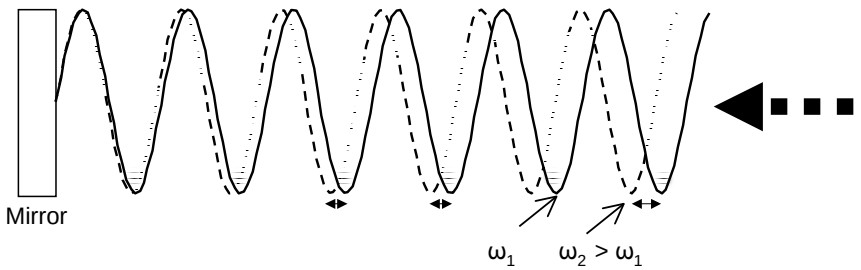

Figure 7.2: The drawing illustrates the importance of short–term frequency stabilization of the optical lattice laser beams. The position of the potential wells is, for simplicity, illustrated in one dimension only. For a slight change in the laser frequency, the shift of the potential minimum increases for larger distances from the mirror.

For this purpose, the optical lattice needs to feature short–term frequency stability. As illustrated in figure 7.2, a change in frequency causes noise in the position of the standing wave minima that contain the atoms. If this oscillation is driven near the magnetic trapping frequencies on the order of approximately 10 kHz, the motion of the atoms will be resonantly enhanced. This constitutes effective heating that can destroy the BEC. Following the advice of two other research groups who have experience with Mott insulators (T. Esslinger, ETH Zürich and I. Bloch, Mainz), we aimed to frequency lock the optical lattice laser to better than 1 MHz for time durations of a few seconds.

For the experiment planned in the rubidium laboratory, and under the supervision of Dr. Johannes Hecker Denschlag, the three dimensional optical lattice is realized with a Titanium–Sapphire (Ti–Sa) laser. Using an external optical cavity, which satisfies the demand for short–term stability, and the Pound–Drever–Hall technique [Dre83], the line width of this ring cavity laser is stabilized to below 150 kHz. Its long–term frequency stability is reduced to a drift of 5 MHz per day, which is of interest to keep the laser within a lockable range and avoid mode hopping. This is done by placing the cavity in vacuum and actively stabilizing it against changes in the surrounding temperature. For the laser lock presented, acoustic noise is reduced by means of a large servo to a bandwidth of approximately 30 kHz, which is limited by natural resonances of the Ti–Sa's piezo–electric transducers.

Chapter 8

Background and basics

To frequency–stabilize our laser, we use an external optical cavity and the Pound–Drever–Hall technique [Dre83]. The basics of optical cavities and the locking method named after the contemporary physicists Pound, Drever, and Hall is introduced in the following.

8.1 Optical cavities

An optical cavity resonator consists of two mirrors that are arranged facing each other along an optical axis, spaced by a distance d. The cavity built in the course of this work is constructed with a planar and a concave mirror, but the underlying physics and the parameters describing the system are best derived from the simpler case of two plane mirrors.

In the case that all dimensions of the cavity are much larger than the wavelength of the electromagnetic radiation, λ, the modes of a cavity (i.e. the field distribution, position and spacing of the eigenfrequencies) can be described, to good approximation, by scalar field theory. Scalar fields can be added following the principle of superposition, and their dispersion is calculated using Huygens' principle of spherical waves. Additionally, the true vector fields have to fulfill two conditions: they must be linearly polarized, and orthogonal to the optical axis. The latter ensures that the fields are transverse to the direction of propagation and all considerations can be confined to the transversal electromagnetic or, in short, TEM–modes.

When a plane wave encounters the input cavity mirror with the reflectivity R, it is divided into two partial waves (neglecting absorption). One part is transmitted through the mirror, the other is reflected. The transmitted and

reflected electrical field amplitudes can be written as

$$\begin{aligned} E_t &= tE_i, \\ E_r &= rE_i, \\ \text{using} \quad 0 &\leq t, r \leq 1, \end{aligned}$$

where E_i is the incident electrical field amplitude, r and t are the reflection and the transmission coefficient, respectively. The light intensity is proportional to $|E_i|^2$ and using energy conservation (and neglecting scattering and absorption losses), we find

$$|E_i|^2 = r^2|E_i|^2 + t^2|E_i|^2 \Rightarrow 1 = r^2 + t^2. \tag{8.1}$$

By definition, the reflectivity R of the mirror is given by $R = r^2$, and the transmittance is $T = t^2$.

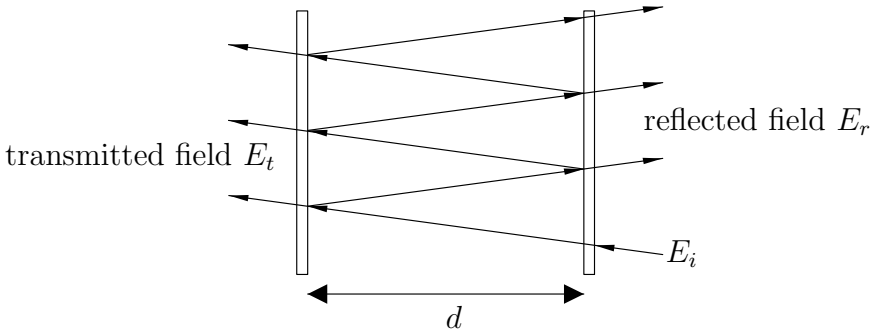

Figure 8.1: Schematics of interference inside an optical cavity. The incident light field, total reflected, and total transmitted field are indicated. Here, the angle of the incident light is chosen large to illustrate the interference effect, but is approximately zero in the experimental setup.

Considering a plane wave that is reflected back and forth between two mirrors as indicated in figure 8.1, we are interested in the overall transmitted and reflected electrical field amplitudes. For simplicity, we assume the refractive index of the cavity medium is $n = 1$. We need to account for interference between the initially reflected or transmitted beams and those that complete one or more round trips inside the cavity before leaving it again. For each round trip, the partial wave acquires a phase shift φ that is related to the cavity length d and the radiation wavelength λ as

$$\varphi = \frac{4\pi d}{\lambda}. \tag{8.2}$$

It takes the time

$$\tau = \frac{2d}{c} \tag{8.3}$$

to complete one round–trip inside the cavity.

The reflected and the transmitted beam

For an infinite number of reflections inside the cavity, we obtain a geometrical series for the overall field amplitudes. The reflected electrical field amplitude is

$$E_r = E_i r_1 + E_i t_1 r_2 t_1 e^{i\varphi} + E_i t_1 r_2 r_1 r_2 t_1 e^{i2\varphi} + \cdots \tag{8.4}$$

$$= E_i \Big(r_1 - t_1^2 r_2 \frac{e^{i\varphi}}{1 - r_1 r_2 e^{i\varphi}} \Big), \tag{8.5}$$

where r_1, r_2 are the reflection coefficients of the first and second mirror. The field amplitude can be written in a geometrical series and assuming $r \equiv r_1 = r_2$, $t \equiv t_1 = t_2$, and $t^2 + r^2 = 1$, we obtain

$$E_r = E_i \frac{(1 - e^{i\varphi})\sqrt{R}}{1 - Re^{i\varphi}}, \tag{8.6}$$

where E_i is the amplitude of the incident light and φ is the phase shift from equation (8.2). Using the substitution $S = 4R/(1-R)^2$, the intensity of the reflected wave, which is detected with a photo diode, is

$$I_r(\varphi) = I_0 \frac{S \sin^2 \varphi/2}{1 + S \sin^2 \varphi/2}. \tag{8.7}$$

The transmitted light intensity through the the cavity, using $I_0 = I_t + I_r$, is

$$I_t(\varphi) = I_0 \frac{1}{1 + S \sin^2 \varphi/2}. \tag{8.8}$$

The transmission through the cavity peaks when $\sin^2 \varphi/2 = 0$. For cavity mirrors with large reflectivities, the transmittance quickly drops to small values when the incident light is off resonance. This result can also be derived from the picture of an intra–cavity standing wave. The cavity length provides the boundary conditions for the TEM–wave whose transverse electrical fields have to vanish on the mirror surfaces. Only waves with discrete wavelengths obeying

$$d = q \cdot \frac{\lambda_q}{2}, \quad \text{where} \quad q = 1, 2, 3, \ldots \tag{8.9}$$

can exist. Around the minima of $\sin^2 \varphi/2$, we can use equations (8.2), (8.9), and the Taylor expansion

$$\sin^2 \varphi/2 \approx \left(\frac{\varphi - 2\pi q}{2}\right)^2 + \mathcal{O}\left((\varphi - 2\pi q)^4\right), \tag{8.10}$$

so that equation (8.8) can be rewritten using the discrete wavelength condition,

$$I_t(\varphi) \approx I_0 \frac{1}{1 + \frac{4R}{(1-R)^2}\left(\frac{\varphi - 2\pi q}{2}\right)^2}, \quad \text{where} \quad q = 1, 2, 3, \ldots \tag{8.11}$$

As the spacing of the cavity mirrors is much larger than the wavelength, $d \gg \lambda$, the number of longitudinal nodes q is large. The TEM_{00q} modes are the standing wave ground modes associated with each q. Accordingly,

$$\nu_q = \frac{c}{\lambda_q} = q\frac{c}{2d} \tag{8.12}$$

is the associated resonance frequency, where c is the speed of light in the cavity medium. The phase φ is related to the frequency ν as

$$\varphi = 2\pi\nu\tau, \tag{8.13}$$

where τ is the time derived in equation (8.3). The transmitted intensity as a function of frequency in the vicinity of a resonance can be written as

$$I_t(\nu) = I_0 \frac{1}{1 + 4\pi^2 \frac{R\tau^2}{(1-R)^2}(\nu - \nu_q)^2}. \tag{8.14}$$

We introduce the detuning

$$\Delta = 2\pi(\nu - \nu_q) \tag{8.15}$$

and rewrite equation (8.14) in order to recognize the Lorentzian shape of the transmission peaks,

$$\frac{I_t(\Delta)}{I_0} = \frac{1}{1 + (\frac{\Delta}{\Gamma})^2} \tag{8.16}$$

with the line width

$$\Gamma = \frac{1 - R}{\sqrt{R}} \frac{c}{2d}. \tag{8.17}$$

We will frequently use the Full Width at Half Maximum (FWHM) line width for simplicity, where FWHM$= 2\Gamma$. The FWHM is illustrated in figure 8.2. Two

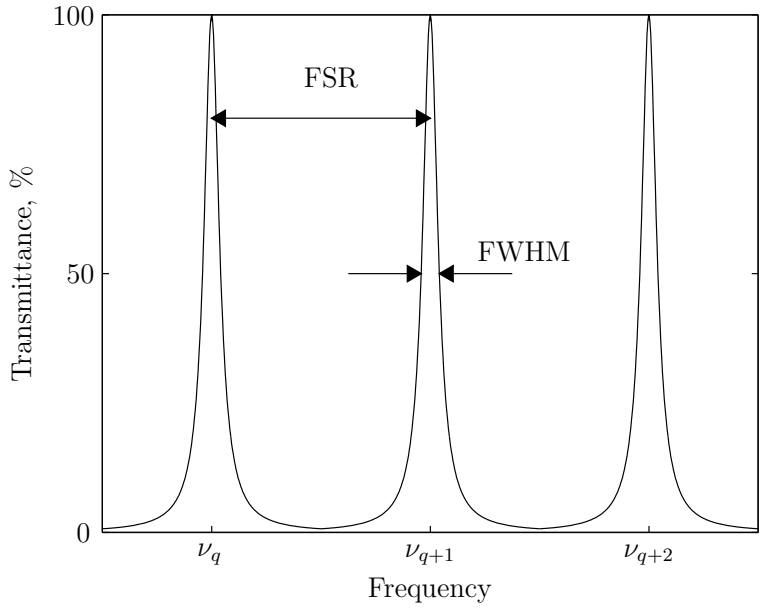

Figure 8.2: Transmission spectrum of an optical cavity. Transmission peaks appear according to the resonance condition and equation (8.14). The free spectral range (FSR) and full line width at half maximum (FWHM) are illustrated. The peaks are Lorentzian shaped.

neighboring ground modes TEM_{00q} and TEM_{00q+1} are separated in frequency by the Free Spectral Range (FSR), defined as

$$2\pi\left(\nu_{q+1}-\nu_q\right)=2\pi\frac{c}{2d}, \tag{8.18}$$

which is illustrated in figure 8.2. The finesse $\mathcal{F}$ of a cavity is defined as the ratio of the Free Spectral Range and the width of the resonance, $\mathcal{F}$ =FSR/FWHM. If the transmission of the mirror $t \ll 1$, the finesse can be approximated by

$$\mathcal{F}\approx\pi\sqrt{R}/(1-R), \tag{8.19}$$

depending only on the reflectivity of the mirrors.

We can rewrite the reflected field amplitude of equation (8.6) in terms of the line width Γ and detuning Δ and obtain

$$E_r\approx E_0\frac{\Delta(\Delta+i\Gamma)}{\Delta^2+\Gamma^2}, \tag{8.20}$$

which is useful for deriving the expression for the error signal generated by the Pound–Drever–Hall method introduced in the following.

8.2 The Pound–Drever–Hall method

The method introduced in this chapter to frequency–stabilize a laser was first employed by R. Pound [Pou46] for microwave oscillators in 1946. R. Drever, J. Hall *et al.* [Dre83] extended the work to optical resonators in 1983. A comprehensive theoretical discussion of the line shapes and signal–to–noise analysis was done by G. Bjorklund *et al.* [Bjo83].

This technique uses the fact that a phase difference arises between sidebands of a laser, which are generated using radio–frequency (rf) modulation, and its center frequency upon reflection from the input mirror of an optical cavity. In this scheme, the laser frequency fulfills the cavity's resonance condition. The obtained antisymmetric beat signal can serve as the input of a suitable feedback circuit. The lock is capable of high precision, low noise and fast response time that is not limited by the cavity.

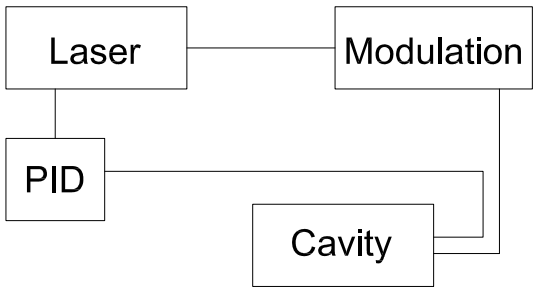

Figure 8.3: Basic principle of the Pound–Drever–Hall lock. The laser light is modulated before irradiating the cavity. The reflected light is used to lock the laser to the cavity by means of a PID–(Proportional plus Integral plus Derivative) controller.

The general arrangement is shown in figure 8.3. The system is controlled by means of a feedback loop that detects the system's state and relates it to a reference. The state is accordingly changed by an actuator and then maintained by means of controlling electronics. If the feedback loop is set up correctly, the system goes to the desired state quickly, and deviations from the reference value are suppressed. For the task of laser stabilization, the system is the laser and its output frequency. The actuator is a PZT (piezo electric transducer) and a galvanometer that move the grating or Brewster mirror inside the laser. In our setup, we use a PID–controller (Proportional plus Integral plus Derivative) to control the deviations from the reference value.

Theoretical background

When applying a periodic radio–frequency (rf) signal of the frequency Ω to a laser running at a single frequency ω, the light is phase modulated and the electric field amplitude is given by

$$E(t) = E_0 e^{i(\omega t + m \sin \Omega t)}, \tag{8.21}$$

where m is the modulation depth. It is defined as the ratio of the modulation amplitude to the modulation frequency. Expansion into a Fourier series yields the electric field amplitude as

$$E(t) = E_0 \sum_{n \in \mathbb{N}} J_n(m) e^{i(\omega + n\Omega)t}, \tag{8.22}$$

where the amplitude of the sidebands is determined by the value of the respective Bessel function $J_n(m)$. For small modulation depths $m \ll 1$, we can limit our considerations to the carrier and the first sidebands with the frequencies ω and $\omega \pm \Omega$. These sidebands are imprinted onto the original carrier signal. They are located spectrally well outside the resonator passband. As $J_{-n}(m) = (-1)^n J_n(m)$, the electrical field can be written as

$$E(t) = E_0 e^{i\omega t}(-J_1(m)e^{-i\Omega t} + J_0(m) + J_1(m)e^{i\Omega t}). \tag{8.23}$$

The phase difference between the left and right sideband amounts to 180 °, as we employed *phase–* rather than *amplitude–*modulation.

The modulated light signal encounters the cavity mirror, as suggested in figure 8.3. We are interested in the total reflected field amplitude. As demonstrated by Bjorklund *et al.* [Bjo83], it is useful to define amplitude attenuation factors and acquired phase shift separately for the three incoming beams, the carrier and the two sidebands. Every summand of equation (8.23) is multiplied by the appropriate frequency dependent term, which can be written as

$$r_0 = \frac{\Delta(\Delta + i\Gamma)}{(\Gamma^2 + \Delta^2)} \quad \text{and} \quad r_{\pm 1} = \frac{(\Delta \pm \Omega)(\Delta \pm \Omega + i\Gamma)}{\Gamma^2 + (\Delta \pm \Omega)^2}, \tag{8.24}$$

and we obtain

$$E_r(t) = E_0[-r_{-1}J_1(m)e^{i(\omega - \Omega)t} + r_0 J_0(m)e^{i\omega t} + r_{+1}J_1(m)e^{i(\omega + \Omega)t}], \tag{8.25}$$

accordingly. With the laser frequency matching the cavity resonance, the rf–sidebands are totally reflected off the cavity input mirror. We observe a build–up of intra cavity standing wave intensity at the laser frequency.

Concerning the total reflected beam, there is an additional *leakage field* from the cavity back towards the laser source, which is in anti–phase with the directly reflected laser field. A fast photo diode detects the resulting power of two superimposing fields: the immediately reflected beam, which contains the phase information between the sidebands, and the *leakage* field of the cavity. The 180 ° phase difference of the two fields at resonance is the key to the Pound–Drever–Hall technique. The total reflected beam is therefore almost cancelled on resonance. Using phase sensitive demodulation techniques, the signal is mixed (multiplied) with the original modulation signal, $\sin(\Omega t + \phi)$, and terms proportional to $2\,\Omega$ are disposed of using a low pass filter. The resulting beat signal is antisymmetric and features a sharp flank at the position of the cavity resonance frequency. We are interested in the intensity of the resulting signal. Combining equations (8.24) and (8.25), we calculate the beat signal $\varepsilon(\Delta)$ as a function of the detuning Δ, which is expressed in terms of the modulation frequency, Ω, and the line width Γ of the cavity. Here, ϕ determines the phase between the signal from the photo diode detecting the reflected beam and the source of oscillation. In accordance with the thesis by G. Thalhammer [Tha00], we obtain the DC component of the signal

$$\varepsilon(\Delta) = kJ_0J_1\frac{\Gamma\Delta\Omega[\sin(\phi)(\Gamma^2+\Delta^2+\Omega^2)+\cos(\phi)\Omega(\Gamma^2-\Delta^2+\Omega^2)]}{(\Gamma^2+\Delta^2)[\Gamma^2+(\Delta+\Omega)^2][\Gamma^2+(\Delta-\Omega)^2]}, \quad (8.26)$$

where the factor k depends on the light intensity, efficiency of mixer and photo diode and $J_0 \equiv J_0(m)$ and $J_1 \equiv J_1(m)$ are the values of the Bessel function. The corresponding calculated error signal is plotted in figure 8.4. The modulation frequency is $\Omega = 20\,\mathrm{MHz}$ and the line width $\Gamma = 1\,\mathrm{MHz}$. We will see later that from a given error signal one can obtain the line width Γ and finesse $\mathcal{F}$ of the optical cavity if the modulation frequency is known.

This rf–modulation technique for producing an error signal provides its locking point, or reference value, at the zero crossing of the center flank, which coincides with the cavity resonance peak. The lock is capable of good performance as the lock range is large, but remains sensitive fluctuations of the resonance peak. Assuming the modulation frequency is larger than the line width of the cavity itself, we can extract the terms linear in the detuning Δ from equation 8.26 and find that the center slope is dominated by the line width Γ. We can write

$$\varepsilon(\Delta) = 2kJ_0J_1\frac{\Delta}{\Gamma(1+\frac{\Gamma^2}{\Omega^2})} + \mathcal{O}(\Delta^3) \backsimeq 2kJ_0J_1\frac{1}{\Gamma}\Delta. \quad (8.27)$$

It is desirable that the slope of the center flank has an opposite sign to the flanks at the sideband frequencies. The frequency range in which the beat signal has

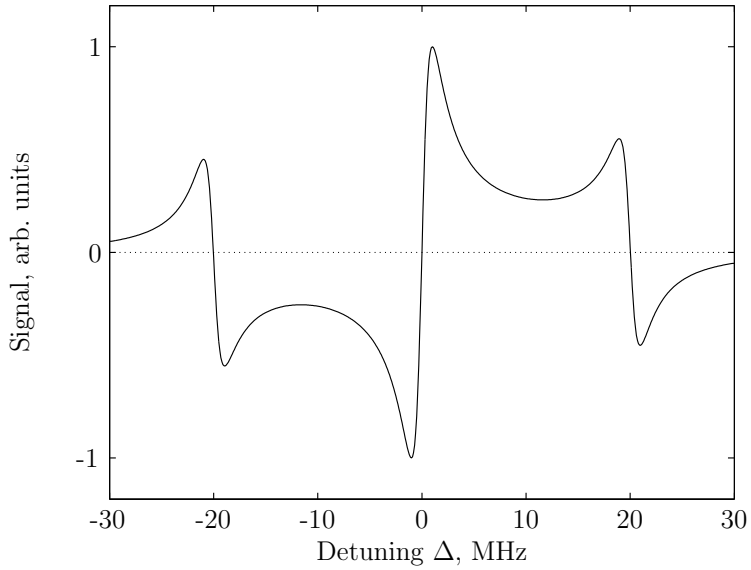

Figure 8.4: The plot shows a typical Pound–Drever–Hall error signal calculated with equation (8.26) and the input parameters: modulation frequency $\Omega = 20\,\mathrm{MHz}$, line width $\Gamma = 1\,\mathrm{MHz}$, phase $\phi = 0$, and prefactor $kJ_0(m)J_1(m) = 1$.

the desired sign amounts to twice the modulation frequency Ω. This property is visible in figure 8.4. The Pound–Drever–Hall technique allows tuning the capture range and center slope of the beat signal independently.

Chapter 9

Implementation of the laser lock

In this chapter, an overview of the parts constructed for the laser lock is given. The optical mirror cavity and related electronics are described in detail. The results for short–term frequency stability are shown in section 9.4.

9.1 Experimental setup

Figure 9.1 shows details of the signal and optical pathways for the Pound–Drever–Hall lock. Laser light is modulated using an electro–optical modulator (EOM), before it irradiates the optical cavity resonator. With our setup tuned correctly and the laser or cavity sweep covering a range of approximately 100 MHz, centered near the cavity resonance, only one frequency results in an intra cavity standing wave intensity. For other frequencies, the input light is reflected off the cavity input mirror. The cavity transmits the center frequency and the sidebands. The total reflected beam, which consists of the immediately reflected and the *leakage* field from the cavity is detected with a fast photo diode. The beat signal that serves as the input of the feedback loop is generated using rf–techniques, where the photo diode signal is mixed with the original modulation signal. The photo diode signal of the transmission through the cavity and the error signal are shown in section 9.4 and discussed there in more detail.

9.2 Optical cavity

For the optical cavity resonator in this laser lock setup, we use two round, high reflecting fused silica mirrors and a low–expansion glass spacer (Zerodur). A schematic cross section drawing can be seen in figure 9.2 on page 64.

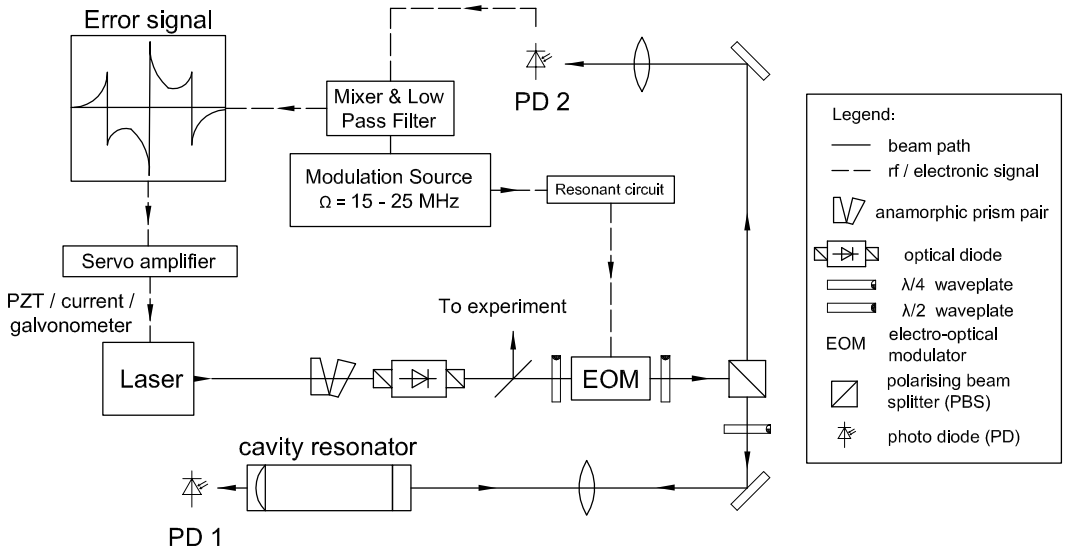

Figure 9.1: Experimental setup showing signal and optical pathways for the Pound–Drever–Hall lock. The laser is locked to the cavity actively stabilizing the laser frequency. Single frequency laser light (at 780 nm for our diode laser and at 830 nm for our Ti–Sa, each with a line width on the order of 100 kHz) passes through a pair of anamorphic prisms to correct for the elliptical shape of the beam, making it circular. We use an optical diode to prevent optical feedback, since this can cause instabilities in the laser. Two rotatable $\lambda/2$–plates adjust the polarization of the beam to allow for maximum phase modulation with an electro–optical modulator (EOM). After passing through a $\lambda/4$–plate, the beam is focussed onto the input mirror of the optical cavity resonator, where most incident light is immediately reflected. A photo diode (PD 1) detects the transmission light through the cavity. The total reflected beam, which consists of the immediately reflected light and the *leakage* field from the cavity is directed towards a fast photo diode (PD 2). The beam passes again through the $\lambda/4$–plate, and has now acquired a total polarization change of 90 °. A typical antisymmetric beat signal is generated using standard rf–techniques, where the signal is filtered and mixed with the modulation signal that also supplies to the EOM. The beat signal features a large center flank and feeds into the servo amplifier that adjusts the laser's current, PZT mounted grating, or galvanometer.

The two round, 1/2–inch diameter, mirrors possess a reflectivity of $(99 \pm 0.5)\,\%$ on the inward facing side and feature an anti–reflective (AR) coating for the wavelength range $680 - 1100\,\mathrm{nm}$ on the outward side. The input mirror, which has two plane faces, is directly glued onto the spacer using an epoxy glue that hardens quickly with exposure to UV light. On the output side of the cavity, a highly reflective concave mirror with a radius of curvature of 250 mm is used. The curved, high reflecting side faces inwards. The output mirror is not glued directly onto the Zerodur surface, but attached with a stack of Piezo electric transducers (PZTs), which are shown in figure 9.3 on page 64 and described in the following paragraph.

In order to be able to scan the length of the cavity, the PZTs are used for changing the relative position of the output mirror in a controlled manner. The PZTs expand and contract according to the applied driving voltage. Our setup uses the PZT material called Pz27. According to its manufacturer, Ferroperm, Pz27 is a soft material that features low aging rates and high sensitivity. The effective length of the cavity can be changed by a few micrometers with a driving voltage of up to approximately 100 V. PZT materials typically show a comparably large coefficient of thermal expansion of $\alpha = 4 \cdot 10^{-6}\,1/\mathrm{K}$. Our PZT tubes are 4 mm thick, and using

$$\frac{\Delta d}{d} = \alpha \Delta T, \tag{9.1}$$

we obtain a length change on the order of 16 nm/K. We will show in section 10.1, where we study the temperature dependence of the cavity's transmission frequency, that this length change can cause a frequency shift of the center frequency on the order of 60 MHz/K.

The Zerodur glass that serves as the spacer for the cavity is hollow so that the cavity medium is air. With the mirrors sealed to both ends, air pressure equalization takes place through a small hole in the Zerodur located at about equal distance between the two mirrors. The Zerodur material features a zero crossing, at room temperature, for the coefficient of thermal expansion. For temperatures ranging from 0 to 50 °C the manufacturer quotes $\alpha = (0 \pm 0.10) \cdot 10^{-6}\,1/\,\mathrm{K}$. For the cavity spacer of length $d = 10\,\mathrm{cm}$ that we use in the laboratory, with an average air temperature of 22.5 °C, we can calculate the temperature induced length change Δd. Using equation (9.1) and a change of temperature of $\Delta T = 1\,\mathrm{K}$ we obtain $\Delta d = (0 \pm 10)\,\mathrm{nm}$. The uncertainty gives an upper bound for the change in the effective cavity length on the order of $\pm 10\,\mathrm{nm/K}$. Employing the estimation laid out in detail in section 10.1, this corresponds to a shift of the transmission frequency in the regime of

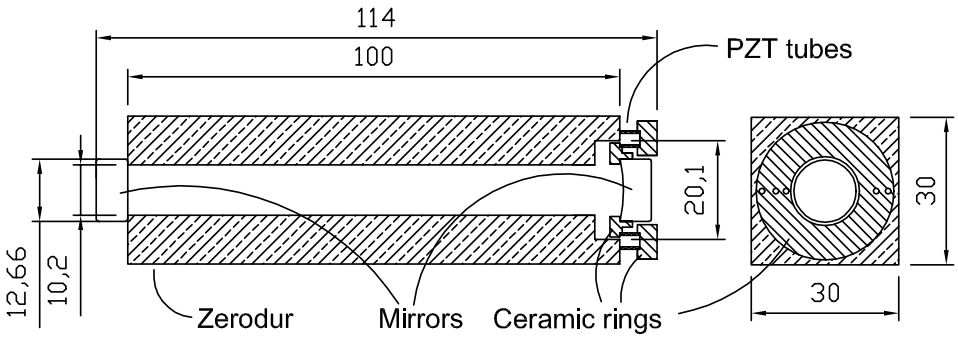

Figure 9.2: Schematic cross section drawing of the constructed cavity. The Zerodur spacer, PZT tubes, mirrors, and ceramic rings are labelled. The PZT arrangement on the right hand side is shown in greater detail in figure 9.3. Laser light is coupled into the cavity from the left hand side. The end view shows the ceramic rings and output mirror construction and illustrates the rectangular shape of the Zerodur glass spacer. All dimensions are given in mm.

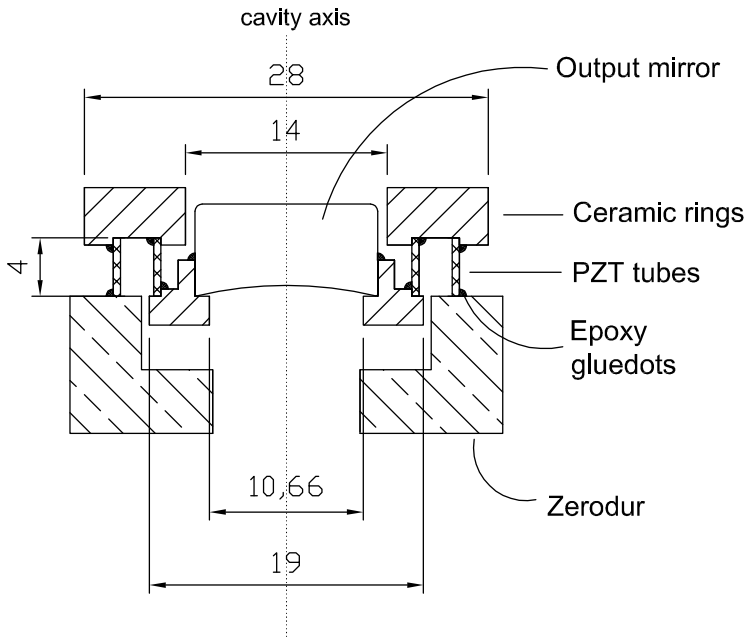

Figure 9.3: The PZT configuration scheme displayed in detail. Only part of the Zerodur spacer is shown, and the rotational axis of the cavity is indicated. The output mirror of the cavity is supported by the smaller of the Macor ceramic rings. Two PZT tubes of equal length (4 mm) but different radii (outer diameter 18.3 mm and 24 mm) connect it to a second ceramic ring, which features feed through holes for the electrical connections, and the Zerodur block. The position of the epoxy glue dots is indicated. Drawings of the ceramic rings are shown in the appendix in figure B.2 on page 115. All dimensions are given in mm.

$\mp 40\,\mathrm{MHz/K}$ [1].

For our cavity, this means that the Zerodur and the PZT contribute to drifts of the resonance frequency caused by thermal expansion on the same order of magnitude. In the case of the Zerodur, we have no design options to counteract its thermal expansion. On the other hand, for the PZT structure, we choose to use two PZTs in such a way, that when the outer temperature conditions cause contraction or expansion of the PZT material, there is no net effect on the cavity length. The design is recommended to us by F. Schmidt–Kaler, who also provided the drawings shown in the appendix in figure B.2, and recommended the use of Macor, a machinable ceramic, for the construction of the parts. To implement this scheme, two piezo tubes of different radii but the same thickness and length are used. The arrangement is shown in figure 9.3 and specific details are given in the caption. Assuming that the two PZTs of the same material and thickness are contracting or expanding in the same manner, the mirror can be assumed to not be subject to thermal movement of the PZTs.

An advantage of this stacking scheme is that both PZTs can be wired and driven together in order to double the travel of the mirror and thus the scanning of the cavity length. For this purpose, one of the PZTs needs to be wired opposite to the other. For flexibility, they are electrically wired individually to BNC connectors. When not in use the BNC plugs are connected to a $50\,\Omega$ load each, to prevent radio–frequency (rf) pick–up effects. The electrical connections only need to carry small currents, and we used thin multi strand wire and conductive silver glue to connect the PZTs. Attachment using soldering can also be done, but care has to be taken to not overheat the PZT and cause damage to the material. For the material we used, the Curie temperature is $350\,^{\circ}\mathrm{C}$. Care must be taken in handling the PZT tubes, since they are very prone to breaking when applying pressure along their radial direction. In order to maintain axial alignment of the mirror to the cavity, care is taken to not leak the glue between the touching surfaces of the ceramics, mirrors and Zerodur body. Therefore, the epoxy is only applied on the edges as illustrated in figure 9.3. We used two to three glue dots for each connection.

With all the described preparations, we expect the Zerodur and PZT stack to contribute to a thermal drift on the order of $50\,\mathrm{MHz/K}$ for changes in the surrounding air temperature. We will see in chapter 10, that experimental results show a relatively large thermal drift of the resonance frequency even with the use of Zerodur and a PZT stack.

[1] Equation (10.5) in section 10.1 calculates the drift of the cavity transmission frequency as a function of temperature, and the sign denotes drifts to smaller or larger frequencies.

Properties of the optical cavity

We construct the cavity as described in the previous paragraphs and place it in the respective beam paths to allow the following characterizations. We refer to the Free Spectral Range (FSR), line width Γ of the ground transmission mode, and the finesse $\mathcal{F}$ which are derived in section 8.1.

Figure 9.4 shows the transmission signal through the cavity. It is taken with a fast photo diode and the Titanium–Sapphire (Ti–Sa) laser running at a wavelength of 830 nm. One single sweep of the PZT voltage easily covers one FSR of the cavity (observed by the repetition of the transmission signal) as marked in the figure. Generally, the FSR can be calculated using equation (8.18). For our cavity of $d = 0.1\,\mathrm{m}$ length, we obtain a FSR of 1.5 GHz. This result is typical for optical mirror cavities.

Figure 9.5 shows the large left most transmission peak of figure 9.4 in detail. By scaling the abscissa using the FSR, we can derive the approximate line width (FWHM) of $2\Gamma = (5 \pm 1)\,\mathrm{MHz}$ for the cavity. Using equation 8.19, this results in a finesse of

$$\mathcal{F} = \frac{1.5\,\mathrm{GHz}}{5 \pm 1\,\mathrm{MHz}} \approx 300 \pm 60. \tag{9.2}$$

As noted in section 8.1, in the limit of high reflectivity, the finesse of an optical cavity can be derived from the reflectivity of the mirrors. In this case, with equation (8.19) from page 55 and a reflectivity of the mirrors of $(99 \pm 0.5)\,\%$, we arrive at a result of $\mathcal{F} = 300$, where within the given uncertainty of the reflectivity, we can give bounds as $210 < \mathcal{F} < 620$. From the beat signal that is generated with the Pound–Drever–Hall method, we can derive the line width Γ, and hence finesse $\mathcal{F}$ using a fit function. These results are discussed in section 9.4 on page 70.

9.3 Light modulation

The modulation and the subsequent demodulation of the laser light are essential for the Pound–Drever–Hall method to lock a laser to a cavity. The electronics for both are accommodated in different housings. This minimizes the generation of higher harmonics and any offset in the photo diode signal. A self built modulation source feeds to an electro–optical modulator (EOM) and a mixer, which multiplies the modulation and the photo diode signal of the light that is reflected from the cavity input mirror. Details to the constructed parts needed for the light modulation are described in this section.

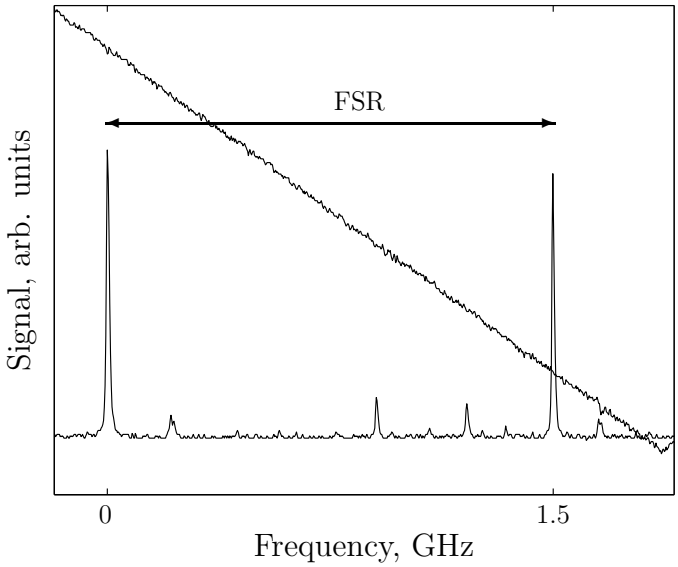

Figure 9.4: Typical transmission signal through the optical cavity irradiated with the Ti–Sa laser (wavelength of 830 nm) and scanned cavity length. The Free Spectral Range (FSR) of 1.5 GHz is covered by one flank of the PZT sweep. After scaling the abscissa with the Free Spectral Range (FSR), the line width Γ of the transmission mode in figure 9.5 can be estimated.

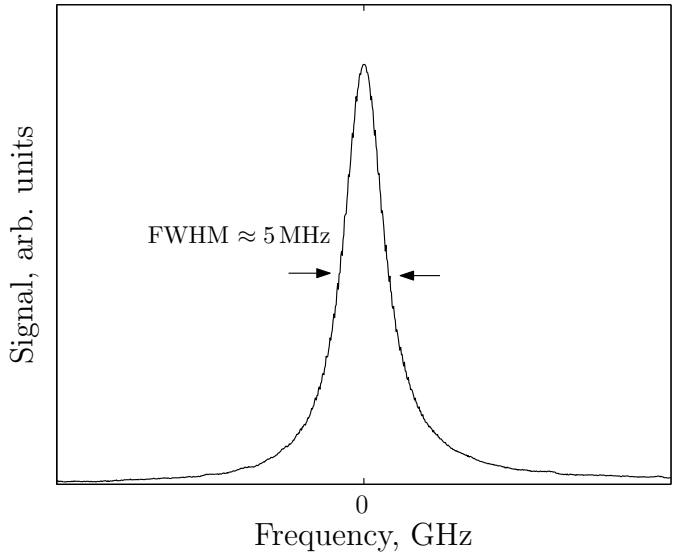

Figure 9.5: The transmission mode (left peak in figure 9.4) of the cavity, using the Ti–Sa laser, shows a FWHM line width of approximately 5 MHz. The abscissa is scaled using figure 9.4. The peak feature appears slightly skewed and we attribute this to the laser and finite response time of the photo diode.

9.3.1 Electro–optical modulator

Using an electro–optical modulator (EOM), the laser light of frequency ω is superposed with a time–dependent signal of the form

$$V(t) = V_0 \sin(\Omega t), \tag{9.3}$$

where Ω is the modulation frequency and V_0 is the signal amplitude. Our EOM consists of a $LiTaO_3$ crystal and appropriate electrical contacts. The electrical field inside this crystal changes its birefringent properties. This phenomenon is described by the Pockels effect which can be reviewed in many standard optics textbook, e.g. [Dem93]. The EOMs we use are schematically shown in figure 9.6. The electrical field is applied perpendicularly to the direction of light propagation, classifying our EOMs to be transverse Pockels cells. One obtains a large pure phase modulated signal when the electrical field and light polarization are truly parallel. Otherwise, amplitude modulation occurs as a side effect causing the beat signal, which is generated by the Pound–Drever–Hall setup, to be stretched unevenly. Two EOMs are at our disposal: one featuring a 60 mm long crystal, and a shorter one with a 30 mm long crystal, which we will refer to as EOM 1 and EOM 2. Generally speaking, the longer the path of modulation, the stronger the modulation signal. With properly adjusted electronics that provide large signal strengths at the required frequencies, we preferred to use EOM 2 in order to make the setup as compact as possible.

The EOM is driven by a rf–sine–wave that has been enhanced by a resonant circuit. The resonant circuit is based on a transformer consisting of a primary coil with an inductance of $100\,\mu$H and a secondary copper coil of about 12 windings, which is secured around the primary coil. The resonant circuit's resonance frequency needs to match that of the modulation source. We made the transformers ourselves and used a commercial modulation source (e.g. Stanford function generator) to determine the resonances.

In order for the modulation frequency Ω to be clearly visible as sideband features to either side of the transmission peak of the cavity, and to successfully apply the Pound–Drever–Hall locking method, Ω needs to be larger than twice the line width of the transmission mode Γ. This results in a clear and distinguishable flank to lock to. The resonance frequency of the EOM depends on the length of the modulation path (i.e. crystal length) and we obtain the resonance frequencies $f_0 = 17.7\,$MHz for EOM 1 and $f_0 = 19.2\,$MHz for EOM 2.

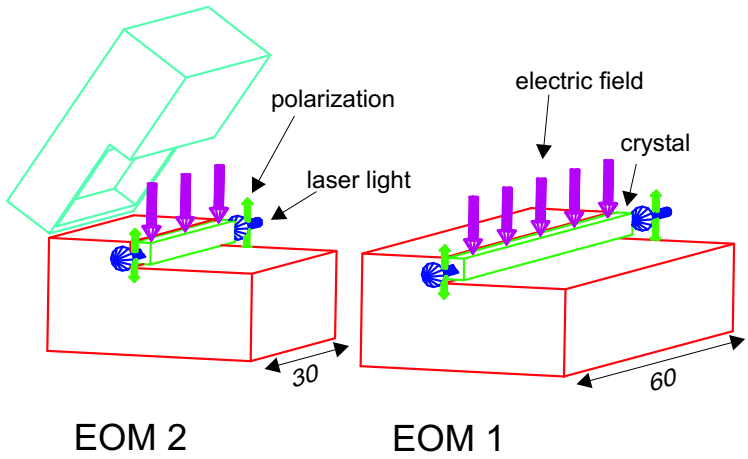

Figure 9.6: Schematic drawing showing the two EOMs at our disposal. The distance of modulation is, as laid out in the text, 30 mm and 60 mm respectively. The electric field direction and ideal polarization of the laser light are indicated by arrows. Electrical contacts and mounting arrangements are omitted. All dimensions are given in mm.

9.3.2 Modulation source

The modulation source feeds to the EOM and the local oscillator (LO) input of the mixer. As described in the previous section, the EOM is used to modulate the laser light. The mixer demodulates the photo diode signal of the reflected light, and the the antisymmetric beat signal is generated. Our self–built modulation source provides output frequencies ranging from 15 to 25 MHz. The circuit schematics of figure 9.7 and experimental details are described in the following.

We use a voltage controlled oscillator (VCO) (Mini Circuits part POS–25) with an output range of 15 – 25 MHz. The frequency is controlled with an operational amplifier (op–amp), which references to a fixed 10 V supply. The output signal of the VCO is then amplified, split, and sent to the EOM and mixer. The VCO is specified to deliver a 7 dBm sine–wave output signal in the frequency range given above. We experimentally verified the output power as a function of frequency and found that it was not constant over the whole range, but varies between approximately 8.3 dBm at 15 MHz and 5.1 dBm at 25 MHz. The VCO requires a 12 V supply and is grounded using a 0.1 μF capacitor. The op–amp that determines the oscillators output frequency (Analog Devices part OPA177GP) works in the following way: a 50 kΩ trimmer resistance is used with the steady 10 V reference (Analog Devices part REF–01) on the

op–amp's $\oplus$ input. It requires a 15 V supply itself. The gain of the amplifier is fixed to a factor of 2 using two resistors of $R_3 = 7.5\,\mathrm{k}\Omega$ and $R_2 = 15\,\mathrm{k}\Omega$ on the $\ominus$ input. The gain is given by $g = 1 + R_2/R_3$, where R_2 is connected to ground and R_3 (referred to as the feedback resistance) is connected to the output. The closed–loop bandwidth depends on the feedback resistance, and to adjust the gain, this resistor must be changed. Reducing R_2 establishes small signal response in the amplifier and large gains can be produced. The input voltage to the VCO can be varied between 0 V and 15 V. The trimmer resistance on the REF–01 is adjusted from the the outside of the housing to determine the appropriate modulation frequency.

The output signal of the VCO is amplified using a second op–amp (National Semiconductor part LM–6181). Its gain is adjusted with a 100 Ω trimmer resistance to a factor of approximately 20. The frequency response of this op–amp displays a low pass behavior that is also present on the respective outputs. Measurements showed the amplified output signal of the POS–25 to vary between 24 dBm at 15 MHz and 21.4 dBm at 25 MHz. At the frequency of $f_0 = 19.2\,\mathrm{MHz}$, which we are interested in when using EOM 2 for the light modulation, the amplifier delivers approximately 23 dBm.

The amplified signal is then split into two signals using a directional coupler (Mini Circuits part PDC–10–1). The coupled ("CPL") output receives (11.5±0.5) dB of the signal, and the "OUT" output receives the rest apart from approximately 3 dB mainline loss. For a modulation frequency of 19.2 MHz, we measured the EOM output (directly connected to "OUT") to deliver 22.3 dBm. The "CPL" output passes through a low pass filter first, then delivers 11.8 dBm for the local oscillator ("LO") output feeding to the mixer.

As shown in figure 9.7, the supply voltages of +15 V, +12 V and −15 V are regulated using fixed output regulators (ON Semiconductor parts MC7815, MC7812 and MC7915). They are grounded to the housing and capacitors are added as buffers as specified in the respective data sheets. These prevent stray high frequency signals from appearing in the circuit's power supply lines. BNC connectors for +18 V and −18 V input are used and protected by diodes.

9.4 Transmission and error signal

The two photo diodes shown in the setup in figure 9.1 detect the transmission signal from the cavity (PD 1), and the reflected light off the cavity input mirror (PD 2). When the light is not modulated, the reflected signal displays a dip where there is transmission through the cavity. When the signal of PD 2 is mixed with the original modulation signal, we obtain an error signal similar to that calculated in section 8.2. A typical error and transmission signal using

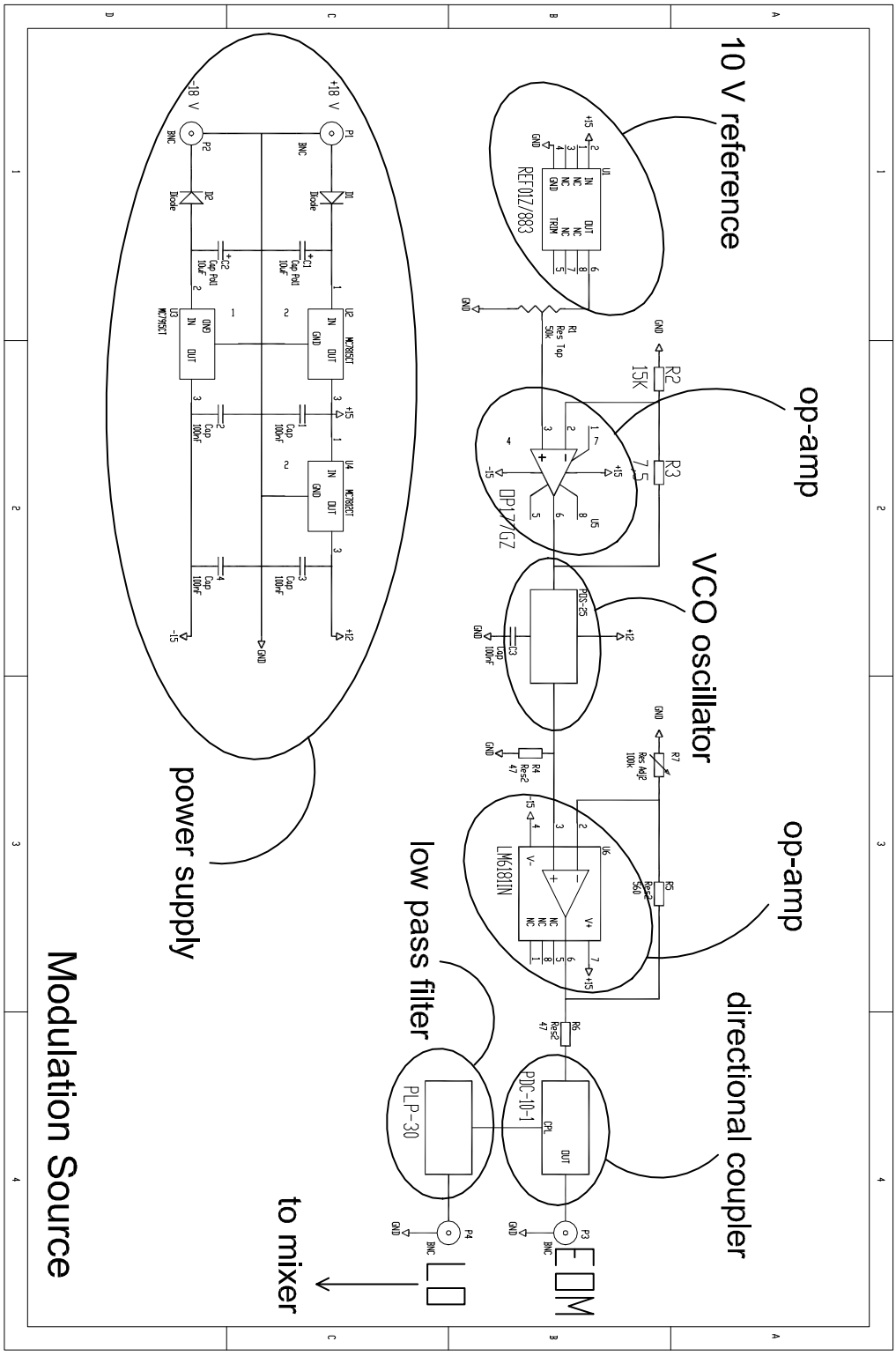

Figure 9.7: The circuit diagram shows the self built laser modulation source for an output frequency range of 15 – 25 MHz. Details are described within the text.

our setup are plotted in figure 9.8. Note that this data was taken using the diode laser at a wavelength of 780 nm.

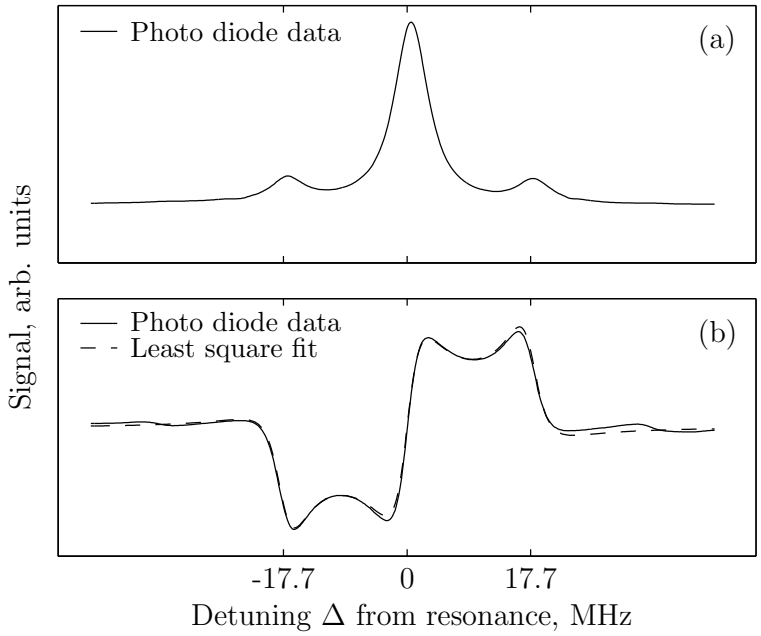

Figure 9.8: Typical transmission and error signal. The modulation frequency $\Omega = 17.7\,\mathrm{MHz}$ (using EOM 1) shows up as side peaks in the transmission signal in plot (a). Plot (b) shows the data of the error signal and a least square fit. With the input parameter Ω, equation (8.26) delivers a FWHM line width of $2\Gamma = 5.65\,\mathrm{MHz}$, and phase $\phi = 0.758 \approx \pi/4$.

If the modulation frequency is known, a fit using equation (8.26) can be done to extract the line width Γ of the transmission peak and finesse $\mathcal{F}$ of the cavity from the error signal data. The line width of the diode laser is typically 500 kHz and does not play a role on this scale. Both photo diode signals are shown in figure 9.8. We obtain a FWHM line width of $2\Gamma = 5.6\,\mathrm{MHz}$. With the free spectral range of 1.5 GHz this yields a finesse of 266. This result is in full agreement with the values that are obtained by scaling the frequency axis by means of the FSR in figures 9.4 and 9.5 on page 67, where $2\Gamma = (5 \pm 1)\,\mathrm{MHz}$ and $\mathcal{F} = 300 \pm 60$ were estimated, as well as with the value for the finesse that is calculated on page 51 using the reflectivity of the mirrors only, where $\mathcal{F} \approx 300$.

The fit shows the phase to be $\phi \approx \pi/4$. When used to lock the laser, the shape of the error signal in figure 9.8 (b) has the advantage that the laser cannot easily jump to a nearby slope with the same sign. We choose to not use a phase adjustment device as the phase can be simply adjusted with the

length of the BNC cable that feeds the photo diode signal into the mixer. The phase remains constant once a suitable cable length is found.

The edges of the plot of the error signal in figure 9.8 (b) show small deviations from the zero signal at about twice the modulation frequency. This suggests that there is modulation with a higher modulation depth m than assumed in the theory. But the amount of laser power going into this higher order side band is negligibly small.

9.5 Properties of the laser lock

The beat signal serves as the input signal of a PID–controller. To take the system into lock, the PZT sweep of the cavity is turned off and the reference value is set to the center flank of the error signal. The electronics feed back to a grating and Brewster mirror of the laser, keeping its output frequency on the frequency of the error signal's zero–crossing. The error and locking signal produced with the Titanium–Sapphire (Ti–Sa) laser running at a wavelength of 830 nm and our cavity setup are shown in figure 9.9.

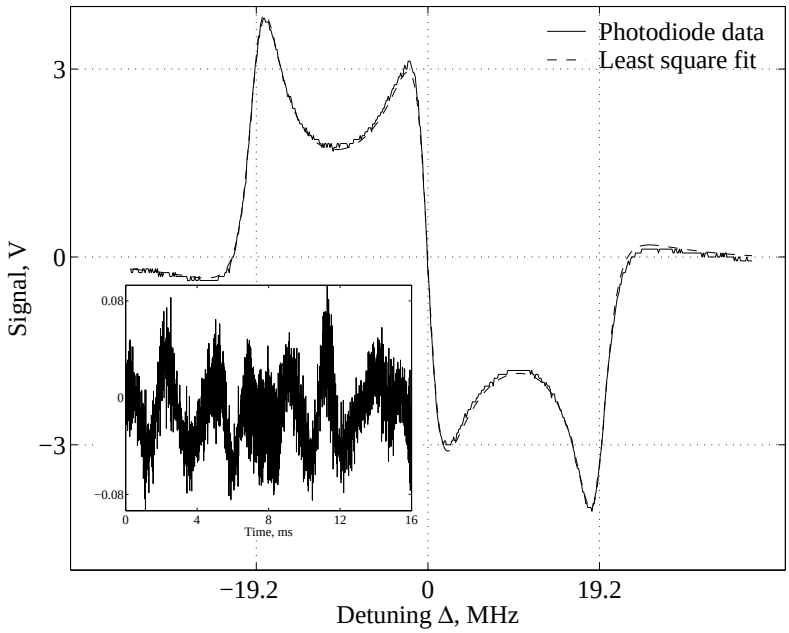

Figure 9.9: Error signal of Ti–Sa (wavelength of 830 nm) laser featuring a center flank of 6 V peak–to–peak. The signal fluctuations of the locking signal in the time domain is shown in the inset. We can derive a frequency fluctuation of 140 kHz. The least square fit of the error signal delivers a cavity line width line width of $2\Gamma = 4.4$ MHz and a phase $\phi = 4.01$.

The center flank displays a 6 V strong signal. When locked, the signal has maximum amplitude fluctuations of ± 0.08 V, which are shown in the inset of figure 9.9. With equation (8.27) and the modulation frequency $\Omega = 19.2$ MHz (using EOM 2), we find that this signal fluctuation translates to a frequency uncertainty of approximately 140 kHz. We are interested in the position uncertainty of the standing wave minima as illustrated in figure 7.2 on page 48. In the experimental setup in the Innsbruck ^{87}Rb laboratory, the BEC is located approximately 20 cm away from the mirror surface. The frequency noise of the laser corresponds to a position fluctuation of the potential wells at that distance of approximately ± 100 pm. This is a satisfactory result concerning the short–term stability of the optical lattice.

We furthermore consider the step response of the system. For this purpose, the system is taken into lock before we apply a square wave voltage onto the locking signal. The disturbance is chosen to be sufficiently small ($< \pm 3$ V), in order for the system to remain in lock. For our considerations, we focus on a downwards step from approximately 1 V to zero as this describes a realistic situation of a short–term disturbance that the locking system strives to compensate for.

We monitor the locking signal in the time domain for sufficiently long times to observe full decay of the disturbance. Figure 9.10 shows the result. Graph (a) shows the signal in the time domain, where the disturbance takes place at $t = 0$. We observe a transient response and a heterodyne beat signal. After 4 ms, the system returns to the initial value with residual noise of less than ± 0.08 V amplitude. Figure 9.10 (b) shows the corresponding frequency domain. We observe a low–pass behavior and hence only show frequencies up to 50 kHz. On this scale, we note peaks in the spectrum at approximately 22.5, 25.6, 30.6, 31.7, and 32.6 kHz. We attribute these peaks to natural resonances of the PZT ceramics.

In first approximation, the system reacts like a low pass filter when progressing from the disturbed state into the desired one, but we observe resonances and a resulting beat signal. From the top graph in figure 9.10, we derive the system bandwidth to be approximately 30 kHz. We conclude that the Ti–Sa's PZTs are the limiting components concerning the reaction time of the lock.

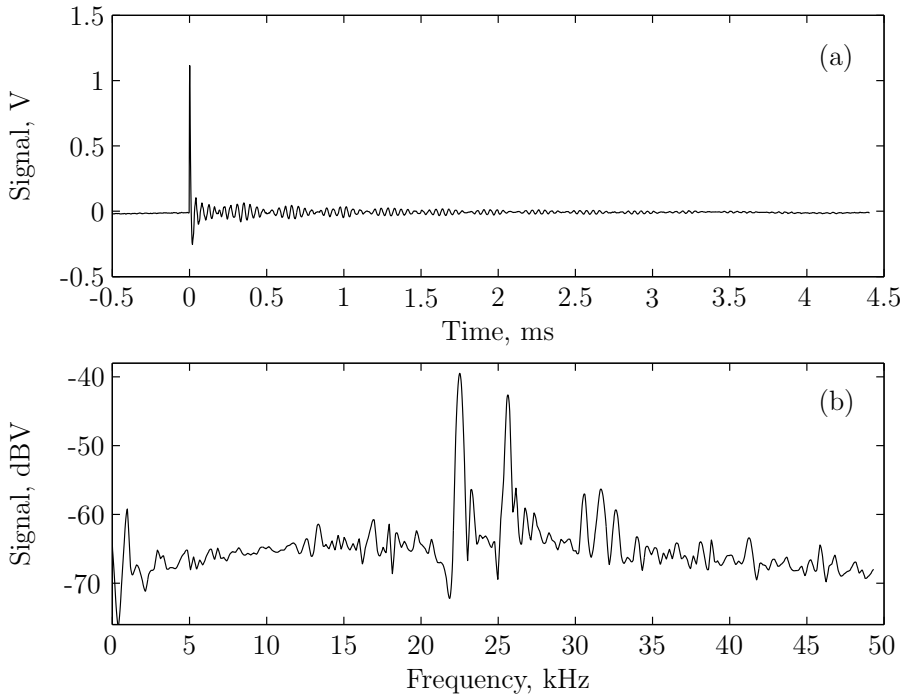

Figure 9.10: The figure shows the step response function of the locking signal in the time domain in graph (a), where we observe a beat signal. The corresponding Fourier transformed signal is shown in graph (b). The resonant features in the frequency spectrum are ascribed to the eigenfrequencies of the Ti–Sa PZTs.

Chapter 10

Stabilization of the cavity

In the previous chapter, we discussed locking the laser to the cavity and found that the laser's frequency stability on the time scale of an experiment ($\sim 1\,\mathrm{s}$) is given by the frequency uncertainty of the locking signal, approximately 140 kHz. In this chapter, we present the causes of the cavity's frequency drift on a time scale of hours and days, as well as the methodology and results of these measurements. We observe that the stability of the cavity transmission relates to changes in air temperature and pressure, but is largely limited by the expansion behavior of the Zerodur spacer. We are able to reduce the overall frequency drift to approximately 5 MHz per day by pressure– and temperature–stabilization of the cavity.

10.1 Origin of the cavity transmission drift

The cavity's resonance frequency is determined by the effective length of the cavity. We are interested in the change in length of the cavity spacer and PZT stack along the optical cavity axis. Since the cavity medium is air, we also study the change of refractive index inside the cavity. These properties alter the effective optical path length. An overview of the effects and their magnitude is given in table 10.1 on page 80.

Generally, the transmission frequency depends on the effective optical path length, l composed of the cavity length, d and the index of refraction, n as

$$l = nd. \tag{10.1}$$

The transmission frequency, according to equation (8.12) on page 54, is

$$\nu = q\frac{c}{2l}, \tag{10.2}$$

where q is the number of nodes of the standing wave and c the speed of light in vacuum. If l increases because the cavity length or refractive index increase, the transmission frequency will decrease. Combining equations (10.1) and (10.2), the resonance frequency depends on the refractive index and effective cavity length. Considering small changes in n and l, this correlation can be written as

$$\frac{\Delta\nu}{\nu} = -\frac{\Delta n}{n} - \frac{\Delta l}{l}. \tag{10.3}$$

In first approximation, the change of the refractive index n, which is proportional to the density, ρ of the gas, is given by ideal gas theory,

$$(n-1) \sim \rho = \frac{p}{RT}, \tag{10.4}$$

where p is the pressure, T the temperature, and R the universal gas constant. We are using this relation separately for an open and a closed system to derive the dependencies on the air temperature and pressure later in this chapter.

Thermal expansion

The Zerodur glass, described in section 9.2, has a thermal expansion coefficient, α, that is dependent on the working temperature. Around room temperature, α features a zero–crossing and is given as $\alpha = (0 \pm 0.10) \cdot 10^{-6}\,1/\mathrm{K}$. Since we calculate the effect of thermal expansion based on the uncertainty limit, we determine the worst case scenario, the upper bound for the influence of the cavity spacer.

To estimate the impact on the transmission frequency, we transform the length change calculated in section 9.2, equation (9.1), into a frequency change by using equations (10.1) and (10.3) to obtain

$$\frac{\Delta\nu}{\Delta T} = -\alpha\nu. \tag{10.5}$$

For the frequency of the diode laser ($\nu = 3.5 \cdot 10^{14}\,\mathrm{Hz} \approx 780\,\mathrm{nm}$), we therefore expect an upper and lower bound for the shift of the cavity's transmission frequency of $\mp 40\,\mathrm{MHz/K}$. Here, the negative value denotes decreasing frequencies, and positive values increasing frequencies, which in this case depend on the sign of α. Similarly, the frequency drift caused by *one* PZT is $-60\,\mathrm{MHz/K}$. The thermal expansion and relaxation behavior of the other cavity parts, e.g. mirrors, are estimated to be much smaller and therefore their effects are neglected.

Influence of the air under atmospheric conditions (open system)

In an *open* system, where the air within the cavity is in contact and exchangeable with the air in the room, the following relation applies: if the surrounding air pressure (density of the gas) increases at constant temperature, the refractive index of the cavity medium increases. We therefore expect the transmission frequency to decrease. Similarly, if the surrounding air temperature increases at constant pressure, the density of the gas inside the cavity decreases, and we expect the transmission frequency to increase.

Under atmospheric conditions of the open system, we can expect the pressure $p \approx 1000\,\mathrm{mbar}$ and the refractive index to be $n \approx 1.00028$. Combining equations (10.3) and (10.4), the dependence of the refractive index on the pressure is given by

$$\Delta n = (n-1)\frac{\Delta p}{p}, \tag{10.6}$$

where the typical change in air pressure over one day amounts to $\Delta p/p \approx 10^{-3}$ and causes $\Delta n \approx 2.8 \cdot 10^{-7}$. For the transmission frequency this means while the cavity length l is regarded as fixed, that the change in frequency with respect to change in air pressure is

$$\frac{\Delta \nu}{\Delta p} = -\frac{(n-1)}{n}\frac{\nu}{p}, \tag{10.7}$$

and we obtain a dependence of $-100\,\mathrm{MHz/mbar}$.

We use equation (10.4) to calculate the explicit temperature dependence. The ideal gas equation delivers the change of the density for small temperature changes, at constant pressure p, and with $\Delta\rho/\rho = \Delta T/T$, we obtain

$$\Delta n = -(n-1)\frac{\Delta T}{T}. \tag{10.8}$$

Using equation (10.3), the drift with respect to temperature is

$$\frac{\Delta \nu}{\Delta T} = \frac{\nu}{T}\frac{(n-1)}{n} \tag{10.9}$$

and yields a value of $330\,\mathrm{MHz/K}$. Using $n \approx 1.00028$ and $\nu = 3.5 \cdot 10^{14}\,\mathrm{Hz}$, we can calculate a change in refractive index of $\Delta n \approx -9.4 \cdot 10^{-7}$. If we assume a typical temperature fluctuation of $\Delta T = 1\,\mathrm{K}$ which yields $\Delta T/T = 3.4 \cdot 10^{-3}$, the absolute change in refractive index is more than 3 times than that caused by the typical change of pressure. We can therefore conclude that within the anticipated fluctuation range for pressure and temperature, the surrounding temperature has larger influence on the transmission frequency than the surrounding air pressure.

Influence of air under constant volume conditions (closed system)

For the *closed* system, the air inside the cavity is not in contact with the air in the laboratory. We create the closed system conditions by placing the cavity into a vacuum chamber with a valve, that makes pumping down to moderate vacuum possible. The valve is located at one of the flanges (see figure 10.4 on page 87). Any pressure change in the system scales with the dependence given in equation (10.7), with the restriction that Δp is small. An increase in temperature constitutes an effective rise in pressure. Once the system is fully thermalized, the density is constant as neither the volume nor the number of particles change.

If we assume the process of rethermalization inside the vacuum body to be slow, we also have to take into account that temperature– or pressure–gradients have an impact on the frequency stability of the system. Figure 10.5 on page 88 shows that the air volume inside the cavity is much smaller than for the rest of the vacuum body. When the vacuum body is heated up rapidly, and if we assume the instantly heated air volume is larger than the air volume inside the cavity, we can expect an inhomogeneous density distribution to develop: the warmer air outside the cavity compresses the colder air inside the cavity. This constitutes an effective pressure increase for the cavity medium. Therefore, when doing rapid temperature changes using the heating arrangement around the vacuum body, the resulting pressure increase causes a drift to smaller frequencies. Without measuring the volumes of the layer of the warmer air and the inner layer of compressed air, it is troublesome to estimate this effect quantitatively.

Effect	System	Drift
Material	thermal expansion Zerodur spacer	$\mp 40\,\mathrm{MHz/K}$
Material	thermal expansion of *one* PZT	$-60\,\mathrm{MHz/K}$
Air	open system	$-100\,\mathrm{MHz/mbar}$ $330\,\mathrm{MHz/K}$

Table 10.1: Summary of effects for drift of cavity transmission. Positive values denote drifts to larger frequencies, negative values to smaller frequencies.

10.2 Saturation spectroscopy

We use Doppler–free saturation spectroscopy on rubidium gas using a diode laser running at a wavelength of 780 nm to monitor the drift of the cavity's resonance frequency. The setup can be seen in figure 10.1, and a typical photo diode signal is shown in figure 10.2. For these measurements, the diode laser is not locked to the cavity, but only internally stabilized onto a grating.

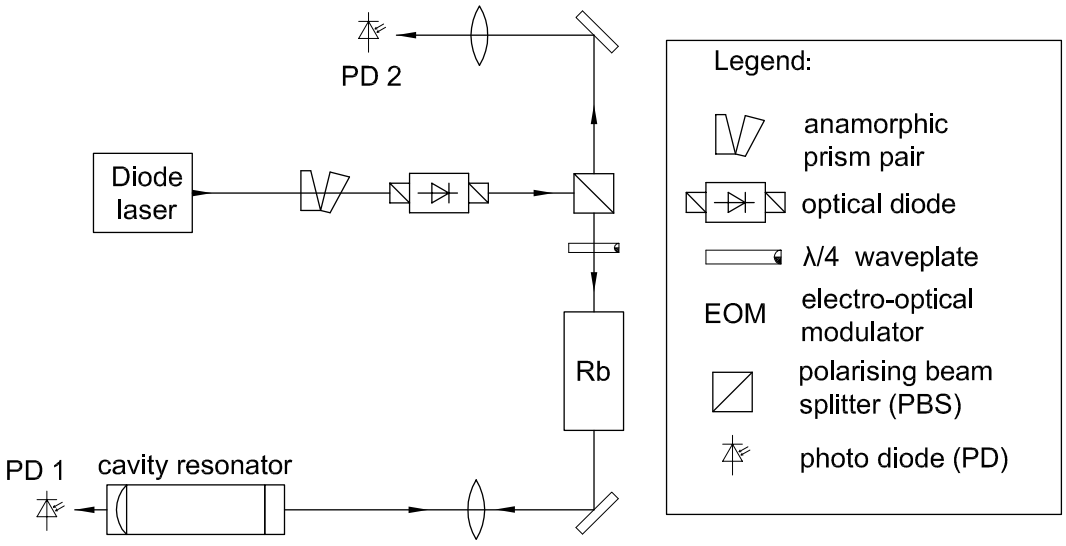

Figure 10.1: Optical setup used for the frequency drift measurement. The diode laser's beam shape is adjusted by a pair of anamorphic prisms and the laser is protected from feedback light by a 60 dB optical diode. After passing through a polarizing beam splitter (PBS) cube, the beam passes through a $\lambda/4$–plate and pumps the rubidium atoms in the glass cell (vapor of natural isotope mixture containing 72 % ^{85}Rb and 28 % ^{87}Rb) before entering the cavity. We use a lens ($f = 300$ mm) to focus the beam onto the plane–plane cavity mirror. The total reflected beam shows a dip at cavity resonance. The reflected beam probes the rubidium atoms in the cell and passes though the $\lambda/4$–plate again. The total polarization shift for the reflected beam now adds up to 90 °, and it is transmitted through the PBS. The beam incident on PD 2 carries the information from the rubidium spectroscopy, and displays dips at cavity resonance. A typical signal delivered by PD 2 is shown in figure 10.2 on page 83.

The light incident onto the cavity serves as the pump beam, and the reflected light as the probe beam, for our saturation spectroscopy setup. The saturating pump beam is stronger than the probe beam as the transmitted intensity is lost into the cavity. The pump beam limits the number of atoms

in the lower state of the transition by equalizing the population of initial and final state atoms. Therefore, the probe beam finds very few atoms to interact with. It travels through the vapor cell without being depleted, even though it is resonant with the electronic transition of interest. We observe features of reduced absorption in the spectrum delivered by PD 2. This effect is called saturation of a transition, and the peaks are referred to as Lamb dips. Cross–over peaks (CO) are a special feature of saturation spectroscopy. They occur because the pump beam and the probe beam can be on resonance with the same atoms of a velocity class with finite velocity component in the beam propagation direction. If the beams evoke transitions from the same initial to different final hyperfine states, we observe peaks at the frequency corresponding to the arithmetic mean value of the two final hyperfine states. Cross–over features are commonly larger than the true hyperfine transitions. A good review of saturation spectroscopy can be found, for instance, in the textbook by Demtröder [Dem93].

We are interested in the rubidium D_2–line, which is the transition from the $^5S_{1/2}$ ground state to the $^5P_{3/2}$ excited state in ^{87}Rb and ^{85}Rb. The two Doppler broadened peaks of the $F = 2$ transition are separated by 4.5 GHz. Their width is on the order of 700 MHz. The frequency spacing of the hyperfine structure is given in table 10.2. Within the resolution obtained, there are three distinct features from the ^{87}Rb D_2–line visible, they are marked as saturation peaks in figure 10.2. A partial rubidium energy level scheme is given in the appendix in figure B.1 on page 114. It contains all the hyperfine spacings of the D_2–line needed to calculate the relative spacing of the peaks.

^{87}Rb $F = 2 \mapsto$	1	CO(1,2)	2	CO(1,3)	CO(2,3)	3	
	0	78.5	157	212	290.5	424	MHz
^{85}Rb $F = 2 \mapsto$	1	CO(1,2)	2	CO(1,3)	CO(2,3)	3	
	0	15	30	46.5	61.5	93	MHz

Table 10.2: Relative peak spacing of the resonance and cross–over (CO) features of the rubidium D_2–line are given.

During all of the presented drift measurements, the diode laser PZTs are scanned with a frequency of 50 Hz. In order to keep the offset range of the PZTs large and be able to conveniently sweep over more than one free spectral range, we use a high voltage amplifier on the PZT$\ominus$ input of the diode laser to provide a large offset. We sweep the PZT$\oplus$ input using a function generator with a 15 V peak–to–peak output. The injection current of the diode laser is used to adjust the laser frequency and, using the strong fluorescence we observe at the electronic transitions, we tune it to the $F = 2$ transition of interest.

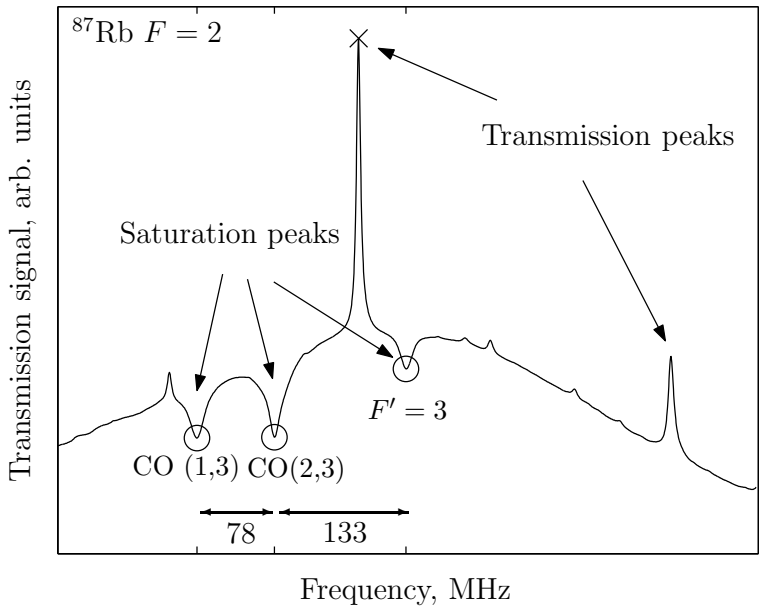

Figure 10.2: Typical signal delivered by PD 2 in the pump and probe experiment with ^{87}Rb. We observe a Doppler broadened overall shape of the $F = 2$ transition. The signal shows multiple distinct peaks. The ordinate is the transmission signal, so that the cavity transmission features show up as peaks. The absolute frequency increases along the abscissa. The light is intentionally coupled into the cavity poorly in order to ensure the saturation peaks and transmission features are reasonably close in frequency. We therefore observe additional peaks to the TEM_{00} ground mode peak. The main transmission peak, whose drift we track, is marked by a cross ($\times$). The three distinct peaks of reduced absorption (Lamb dips and CO peaks) are marked by circles ($\circ$). Their relative spacing is given on the abscissa in MHz. These fixed spacings are used for the scaling of the frequency axis.

The signal from PD 2 is shown in figure 10.2. The Doppler–broadened Gaussian absorption profile of the ^{87}Rb $F = 2$ transition shows signs of reduced absorption (dips) for the electronic and cross–over resonances. Along with this hyperfine structure, we observe peaks at the resonance frequency of the cavity. The relative spacing of two of these features is tracked over time to determine the drift of the transmission resonance. The frequency axis (abscissa) is scaled using two saturation peaks, as their spacing can be regarded as fixed for lab conditions. The temperature, as shown in the following measurements, is always stable to within one Kelvin. Changes in the surrounding magnetic field, that would change the hyperfine splitting and therefore the spacing of our scaling standards are typically on the order of $\frac{1}{10}$ G in the laboratory. As the

magnetic moment of alkali atoms is on the order of 1 MHz/G, we can assume out transition lines to be stable to within 1 MHz.

The use of only one diode laser for the measurement makes the experiment independent of the drift of the diode laser, as both features of interest move in the same way. With a line width of 5 MHz for the transmission mode and approximately 15 MHz for the saturation features, determining the relative position of the peaks depends on the distance between the compared features and their position in the Doppler broadened spectrum. The situation we found to be close to ideal, in this respect, is shown in figure 10.2. The scattering of data points can, depending on which transmission mode is being tracked, vary between ± 2 and ± 6 MHz for the same data set. We refrained from using fit functions to determine the center of the peaks, so that the uncertainty for finding the peak center is estimated to be 1 MHz. Intensity fluctuations and an uneven sweep of the laser add to the measurement uncertainty.

Alternatively, we considered splitting the beam and taking two individual signals with two photo diodes of the transmission and the saturation spectroscopy, also enabling us to subtract the Doppler profile. This has the advantage that when the resonance features of the cavity transmission and the saturation are very close to each other, the position shift that occurs as they overlap does not affect the measurement. Generally speaking, the position measurement of two peaks depends on their relative spacing. If they are separated by less than their line width, the distance between the peaks appears larger, as the peaks effectively repel each other.

10.3 Components for cavity stabilization

The cavity is placed in a vacuum housing and actively temperature stabilized against the changes of the surrounding air temperature. The involved construction task is briefly introduced in the following and all relevant parts are shown in figures 10.3 to 10.7.

10.3.1 Vacuum housing

The cavity is placed inside a small vacuum tube so that the changing air pressure does not affect the cavity medium. Initially, we planned to evacuate the chamber by pumping it with a turbo pump for a finite time, disconnecting the pump and then using the cavity with the valve closed. We were aiming for a stable vacuum in the mbar regime. The total size of the cavity is $114\,\text{mm} \times 30\,\text{mm} \times 30\,\text{mm}$ (made up by the spacer and the mirrors as illus-

trated in figure 9.2 on page 64) and we desire the most compact setup possible. The arrangement of the cavity in the vacuum housing and the flanges are shown in figures on page 86 and 87. Details on the individual components can be found in the respective captions.

Quality of vacuum

We found that our original plan of pumping the chamber down to approximately 10^{-4} mbar, then closing the valve and expect only a negligible change of the inside pressure was too optimistic. We experienced the vacuum to perform very poorly once the pump was disconnected. In hindsight, we believe that dirt and out–gassing (e.g. tin solder used for PZT wiring) effects are responsible for this.

The quality of the vacuum improved for considerably longer pumping times, and we attribute part of the problem to the small diameter connecting tube from the vacuum body to the pump. It measures approximately 4 mm in diameter (see figure 10.7) and limits the flow. We can not rule out leakage problems entirely. The valve and BNC connectors were welded onto the flanges and we think it likely that a hairline crack is responsible for the bad performance of the vacuum. Due to time constraints and lack of better equipment (i.e. pump stand with leak detector), the search for the problem could not be continued.

The only available measuring device was a Pirani probe capable of detecting pressures down to 10^{-3} mbar. On multiple occasions and for various pumping times, we timed the pressure increase from 10^{-3} mbar to 10^{-2} mbar. Assuming a linear pressure increase, we can extrapolate to larger values. As a typical result, we obtain a 35 minute time interval, which leads to a leakage rate of $5 \cdot 10^{-6}$ mbar l/s. Unfortunately, we were also not equipped to track the pressure inside the chamber while conducting stability measurements using the saturation spectroscopy. Long–term measurements shown in section 10.4.2, however, display the loss of vacuum and verify the estimated leakage rate. The frequency drift induced by the loss of vacuum amounts to approximately -6 MHz per day.

We conclude therefore that apart from a possible leakage, contamination effects also play a role as longer pumping times improve the overall vacuum stability.

10.3.2 Temperature stabilization

The overall temperature of the cavity in its vacuum housing is stabilized by means of a two–stage heating arrangement. Both circuits are controlled with

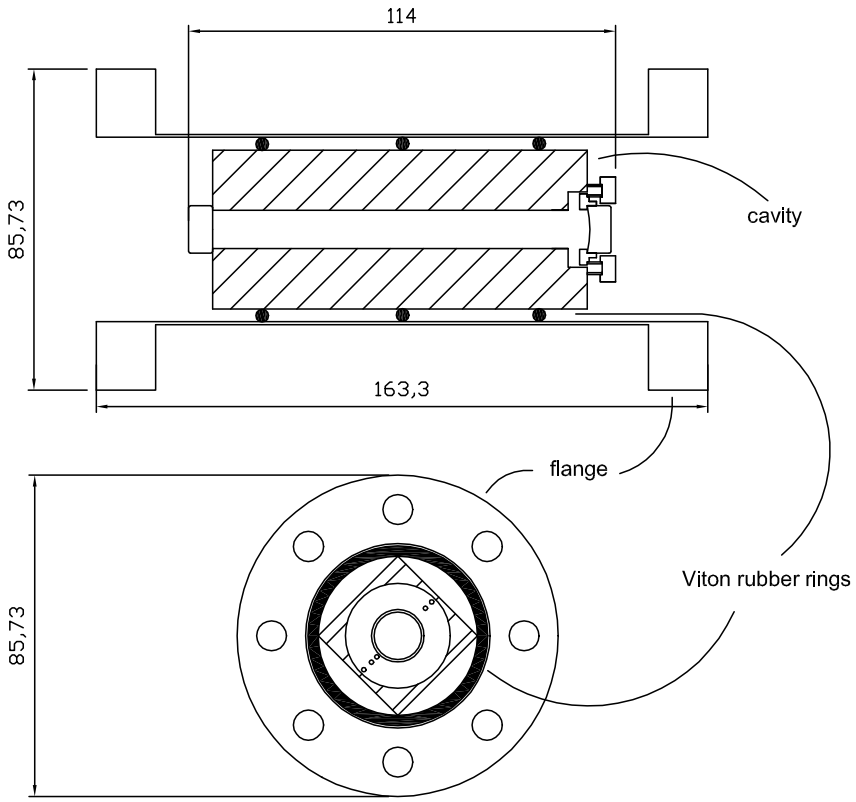

Figure 10.3: Schematic axial cross section drawing of the cavity inside the vacuum tube. The components has US standard size 3 3/8" ConFlat flanges. The cavity is secured inside the chamber by three Viton rubber rings, which fit snugly over the glass block. Inside the tube, these rubber rings are tightly wedged between the corners of the Zerodur block and inside wall, as can be seen in the front view. This structure was found to be very reliable. The closing flanges are illustrated separately in figure 10.4 on the following page. All dimensions are given in mm.

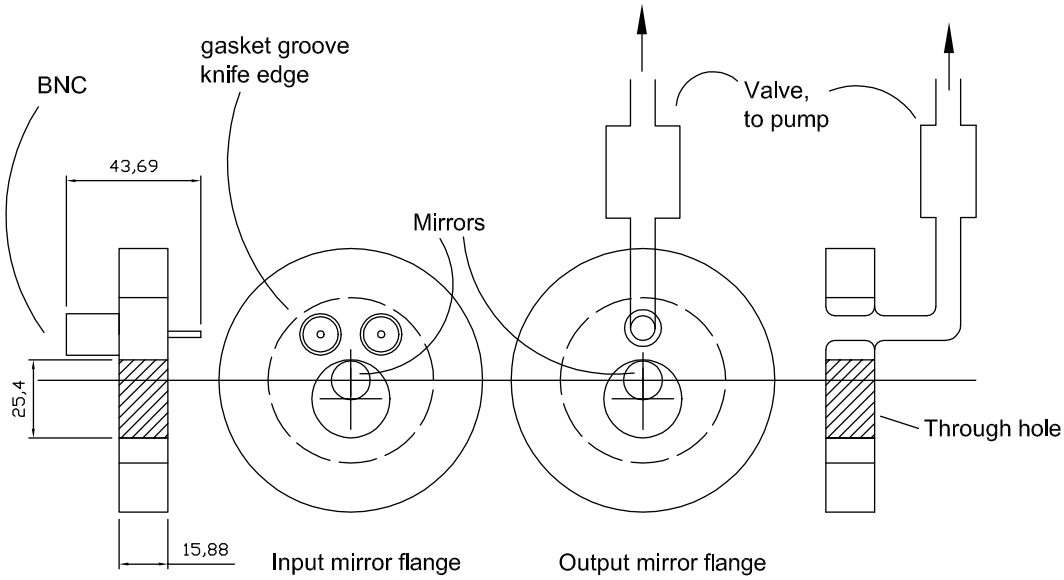

Figure 10.4: Schematic drawings of the two 3 3/8" flanges used for closing the vacuum component shown in figure 10.3. The first flange (input mirror side with BNC feed throughs) is shown in a cross section on the very left hand side. Next to it, the front view is shown. The front view of the second flange (output mirror side with valve) is shown along with the cross section next to it. The position of the mirrors of the cavity is indicated. Bolt holes are omitted, but the outer knife edge of the gasket groove is shown as a dashed line. Optical access is provided through the flanges, where uncoated substrates are fitted into a provided groove using two component UHV glue. We found that etalon effects between the two windows played no role. The substrates in the feed through holes are located off center with respect to the flange. We used weldable BNC connectors for the PZT connection. They are grounded onto the vacuum body. Due to problems with grounding and 50 Hz pick–up effects, a proper connection to a large ground, i.e. the laser table, is advisable. On the inside of the vacuum housing, we soldered the PZT wires to the adapters. We used ordinary tin–solder, but found it to contribute negatively to the quality of the the vacuum. All dimensions are given in mm.

a slow PID box. The controller was adapted from an existing design and assembled by Charly Pilch, and will not be described here in detail. Background information can be, for instance, found in the textbook by Tietze and Schenk [Tie02]. The inner heating stage is kept at a nominal value of $\sim 30\,^{\circ}\mathrm{C}$ and the outer one at $\sim 28\,^{\circ}\mathrm{C}$. The setup is illustrated in a schematic cross section in figure 10.5.

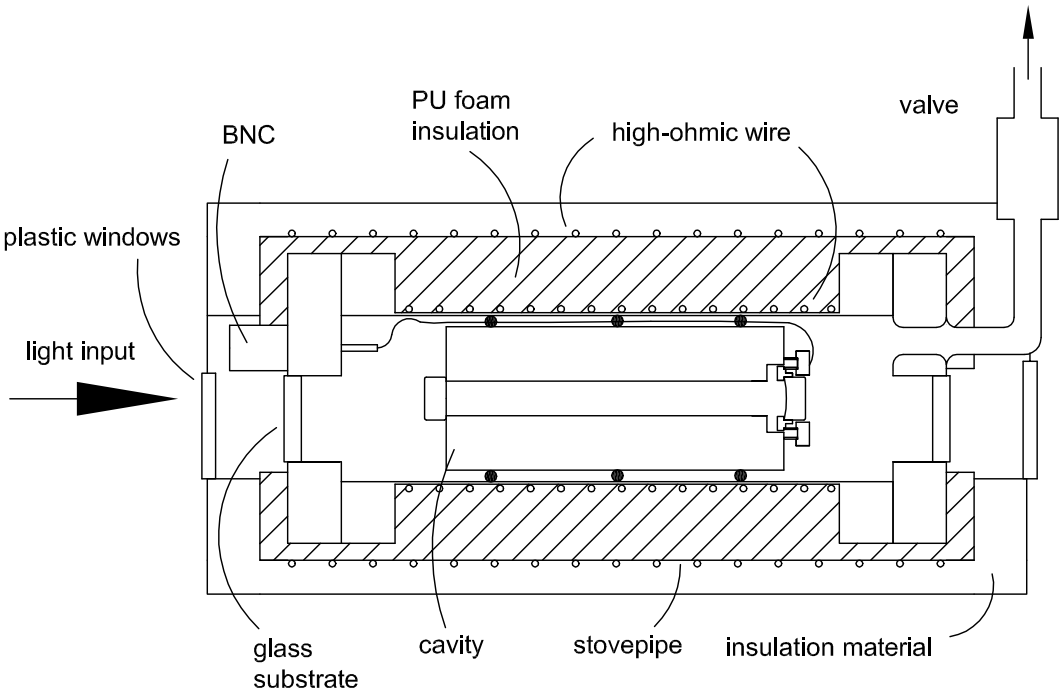

Figure 10.5: Schematic cross section of temperature stabilized and insulated cavity in vacuum housing. High–ohmic wire ($3.9\,\Omega$/m, $\varnothing = 0.4\,$mm), which is used for heating, is secured around the center part of the vacuum tube. The tube is passively insulated by a form fitting shape that is moulded with fast drying two–component PU (polyurethan) foam. This first stage is placed in a simple aluminum pipe (stovepipe), which is temperature stabilized in the same manner and insulated with foam plastic. Lids with plastic windows are fitted over the stovepipe. The wrapped cavity rests on two sturdy feet cut from dense insulating material, which are not shown. Also omitted is the position of the circuit boards that accommodate the sensor loops. They are attached to the flanges and are shown in figure 10.7.

We use 0.4 mm diameter wire with a resistivity of $3.9\,\Omega$/m. The total resistance amounts to approximately $13\,\Omega$ for the inside stage and $22\,\Omega$ for the outside stage. Three $100\,\mathrm{k}\Omega$ thermo–resistors with negative temperature

coefficient (NTC) are placed onto the vacuum body and outer aluminum pipe housing. One of these three is used to monitor the local temperature and the other two feed back to the regulating electronics. The two controlling NTCs of each stage are well spaced to obtain a total resistivity that corresponds to the average actual temperature value. They are connected in series and are part of a bridge circuit that determines the desired temperature value. The sensor circuit is shown in figure 10.6. Each circuit is accommodated on a 6 cm $\times$ 4 cm circuit board and attached to the flange of the vacuum tube as shown in figure 10.7.

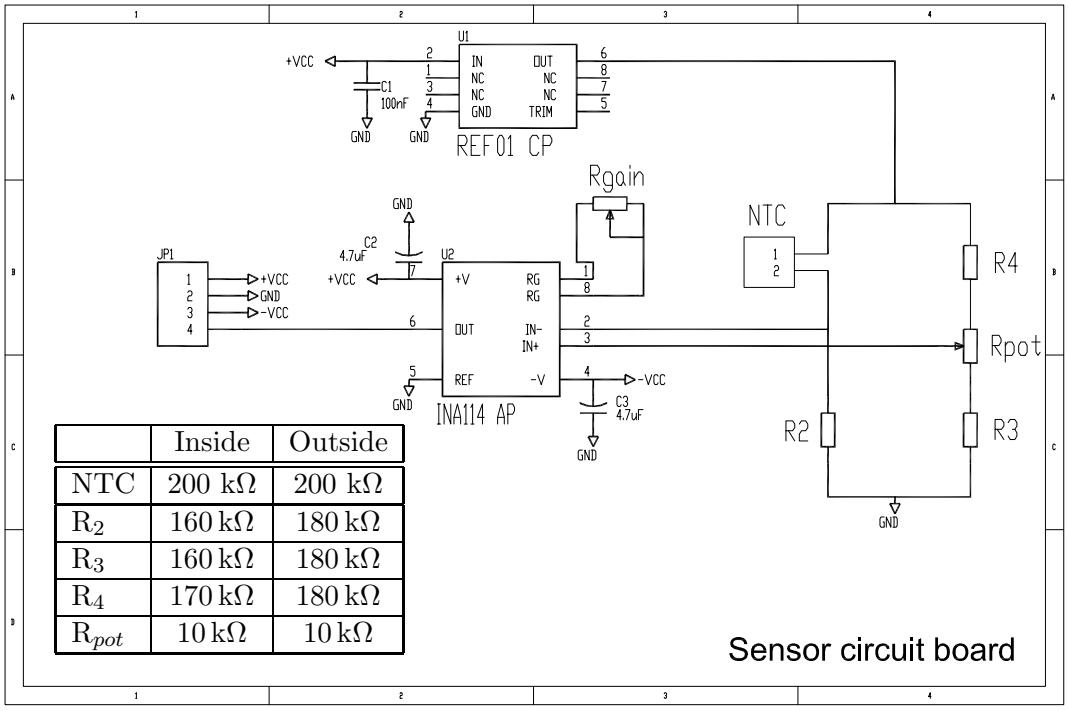

	Inside	Outside
NTC	200 kΩ	200 kΩ
R_2	160 kΩ	180 kΩ
R_3	160 kΩ	180 kΩ
R_4	170 kΩ	180 kΩ
R_{pot}	10 kΩ	10 kΩ

Figure 10.6: Circuit diagram of sensor circuit used for active temperature stabilization of the cavity. Two potentiometers adjust the desired temperature value and the gain of the instrumental amplifier (INA114). Bipolar capacitors are used on the signal cord to filter 50 Hz noise. Long transmission of the non–amplified signal is therefore avoided. This prevents undesirable pick–up effects of rf–noise and enables reliable functionality of the feedback circuit. Each of the circuits (inside and outside temperature) is accommodated on a 6 cm $\times$ 4 cm board that is attached to the flange below the valve as shown in figure 10.7. The resistances for the bridge are given in the table.

The amplified signal from the temperature bridges serve as the input signal for the feedback servo. When tuned correctly, the system goes slowly into the desired temperature state. We observe adjustment times on the order of

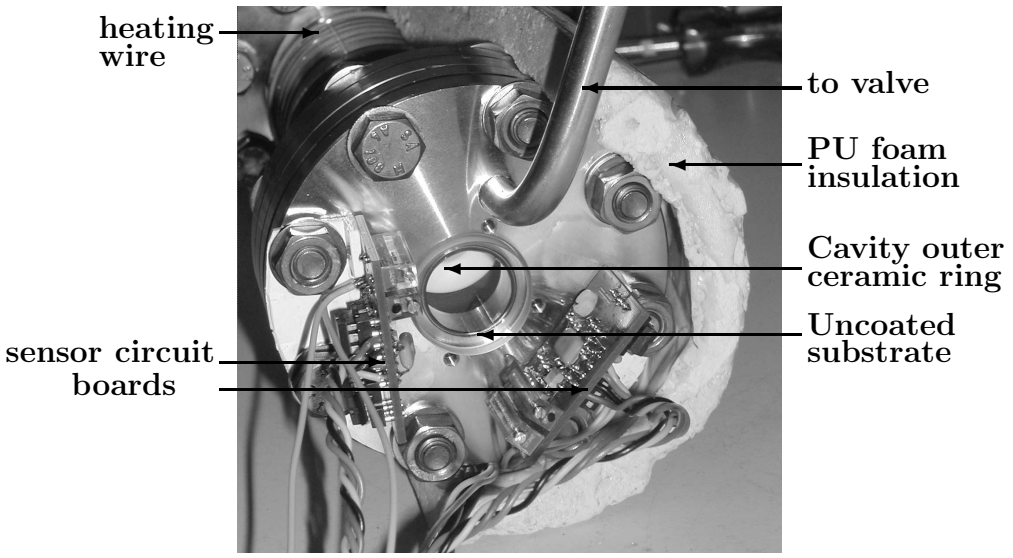

Figure 10.7: The photograph shows the valve side (output mirror) of the vacuum housing with the cavity inside. The sensor circuit boards are attached to the flange screws without obscuring optical access. Long transmission pathways are omitted with this design. The form fitting PU foam insulation is partially shown.

30 minutes. We want to ensure that cooling (strictly passively) and heating over the same temperature range takes approximately the same time. With a well insulated system, this requires small heating rates and gain factors. Measurements show that it can take hours for the system to arrive at a steady state when disrupted severely. This is partly caused by the slow thermalization of the steel housing, cavity, and other components.

With the setup built in scope of this project, the monitoring NTCs of both heating stages display drifts in the resistivity reading with an amplitude of $\pm 100\,\Omega$. This corresponds to a temperature fluctuation of $\pm 40\,\mathrm{mK}$. Regarding the inside heating stage, we observe this fluctuation on a time–scale of 24 hours, and concerning the outside heating arrangement, on the scale of 2 hours. This behavior is shown in figure 10.12 on page 97, where we show the results of the frequency drift and the temperature variation of the heating arrangements over the course of 35 hours. Even though the frequency of this fluctuation is sufficiently small, the PID–controller does not compensate for the deviations, as their amplitude is smaller than the noise signal. We assume that by choosing a larger capacitor and small gains in the control loop, the deviation could be reduced in turn for accepting a larger tune in time.

The valve of the vacuum body, which was wrapped with insulating material but not actively stabilized, proved to be a problem for the temperature

stability of the system. The valve is not actively heated, but heat loss is prevented passively by wrapping the valve in insulating material. We found the valve to have a large impact concerning the temperature homogeneity within the vacuum body. Local heating of parts of the valve to approximately 38 °C showed instant drifts of the transmission frequency on the order of up to 100 MHz.

10.4 Measurements of long–term frequency stability

To determine the relative drift of the transmission frequency, we used the optical setup shown in figure 10.1 and took photo diode signals similar to those in figure 10.2 on page 83 in regular intervals under different conditions. The results are shown in the following.

10.4.1 Cavity under atmospheric conditions

Using the bare, unstabilized cavity, we measure the relative frequency drift on a short–term timescale and take data points every 8 minutes for $7\frac{1}{2}$ hours. We record the room temperature and air pressure at the same time. Consequently, we obtain information about the frequency drift per mbar and Kelvin. The surrounding air temperature is measured using a digital thermometer with a limited resolution of $\pm 0.1\,°\mathrm{C}$. The air pressure is taken with a aneroid barometer. The uncertainty for reading off this device is in the $\pm 0.1\,\mathrm{mbar}$ regime. The resolution and accuracy of the frequency data set is estimated to carry fluctuations on the order of the line width of the cavity, approximately $\pm 3\,\mathrm{MHz}$.

Figure 10.8 shows the result of the measurement. Larger positive values for the transmission frequency on the ordinate denote a drift to larger frequencies, while drifts to smaller frequencies are denoted by negative values. The first data point is used as reference zero for the frequency drift.

We observe a correlation between the three parameters frequency drift, air temperature, and air pressure. The frequency drift is inversely proportional to the surrounding air pressure and proportional to the air temperature. As laid out in section 10.1, we can estimate the frequency drift the three parameters cause. The total drift we observe is a combination of both effects, and the values given are upper bound dependencies.

In detail, the **air pressure** (figure 10.8 (a)) increases steadily over the observed period by approximately $\Delta p = 1.5\,\mathrm{mbar}$. This corresponds to a relative increase of 0.2 % and yields $\Delta p/p \approx 2 \cdot 10^{-3}$. The change of the

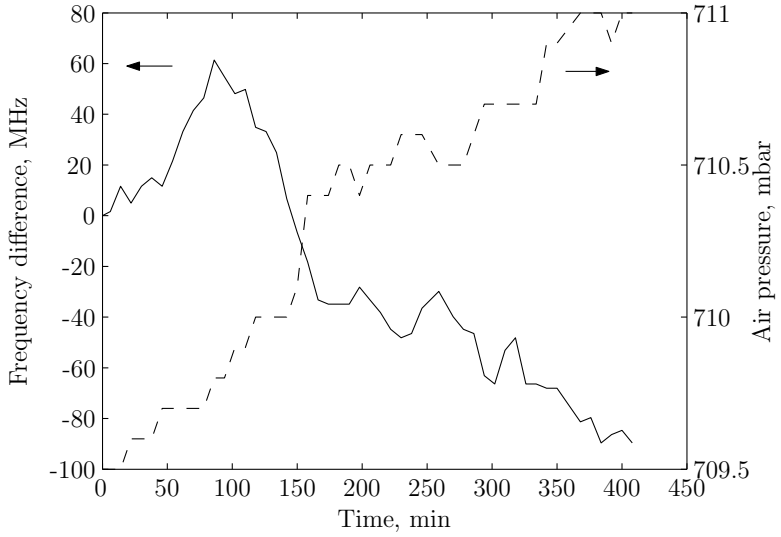

(a) Air pressure.

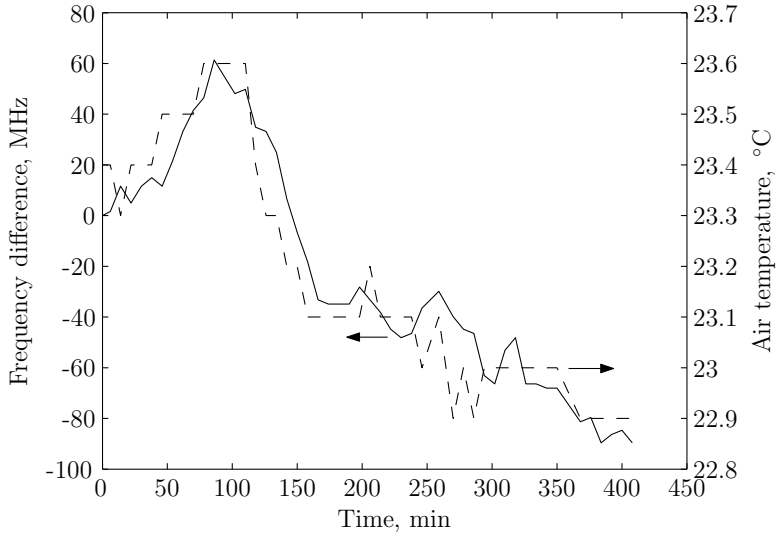

(b) Air temperature.

Figure 10.8: Frequency drift measurement using the unstabilized cavity under atmospheric conditions. Frequency drift as a function of air pressure (a), and of air temperature (b). The solid line denotes the relative drift in MHz and scales with the left hand axis. The dashed line denotes the air pressure (air temperature) and values are shown on the right hand axis.

refractive index, Δn is on the order of $6 \cdot 10^{-7}$. Using equation (10.6), we can derive the quantitative dependence of $-100\,\mathrm{MHz/mbar}$. The sign and amplitude of the frequency drift meet our expectation, and we observe that the transmission frequency is reacting quickly to changes in the refractive index of the cavity medium. The **air temperature** surrounding the cavity (figure 10.8 (b)) shows a general downwards trend. The variation is $-0.7\,^{\circ}\mathrm{C}$ or $-0.2\,\%$. Considering equation (10.9), we find that the cavity is subject to a drift of approximately $200\,\mathrm{MHz/K}$, which is in agreement with the values presented in section 10.1, where we give estimates for the frequency drift based on the ideal gas.

The observed drift is a combination of both the cavity medium and thermal expansion effects. The data shown in figure 10.8 does not allow for a clear distinction between influences of the cavity medium and thermal expansion contributions, which in the case of the Zerodur spacer, are expected to be in the range of $\mp 40\,\mathrm{MHZ/K}$. We repeated above measurements with the cavity under vacuum conditions ($\sim 10^{-1}\,\mathrm{mbar}$) and learned that the amplitude of the drift can be lowered by a factor of two on the same time scale.

10.4.2 Cavity under vacuum conditions

The long–term drift of the transmission frequency was measured over 12 consecutive days. We measured the drift as described before and noted the temperature of the air surrounding the cavity housing. The same digital thermometer with a resolution of $\pm 0.1\,^{\circ}\mathrm{C}$ was used. We took an average of 8 data points per day. Concerning the vacuum quality inside the housing for this measurement, we pumped the cell for multiple days and then disconnected the turbo pump before the measurement started.

Figure 10.9 shows the result of the long–term measurement. The zero point on the frequency axis denotes the value of the first data point taken. From there, we observe the signal to move to decrease (negative values) or increase (positive values). We note a clear correlation in the daily change of the air temperature and the position of the transmission signal, namely an increasing frequency for increasing temperatures. Additionally, we observe an overall downslope drift of the transmission frequency.

The daily temperature dependence is shown in figure 10.10, where we show the change in temperature ΔT versus the frequency for the different days. It is approximated to $55\,\mathrm{MHz/K}$. This correlation is attributed to thermal expansion effects of the cavity and, as derived in section 10.1, is in accordance with thermal expansion calculated for the Zerodur cavity spacer of $\mp 40\,\mathrm{MHz/K}$.

We attribute the overall downward slope on the frequency data visible

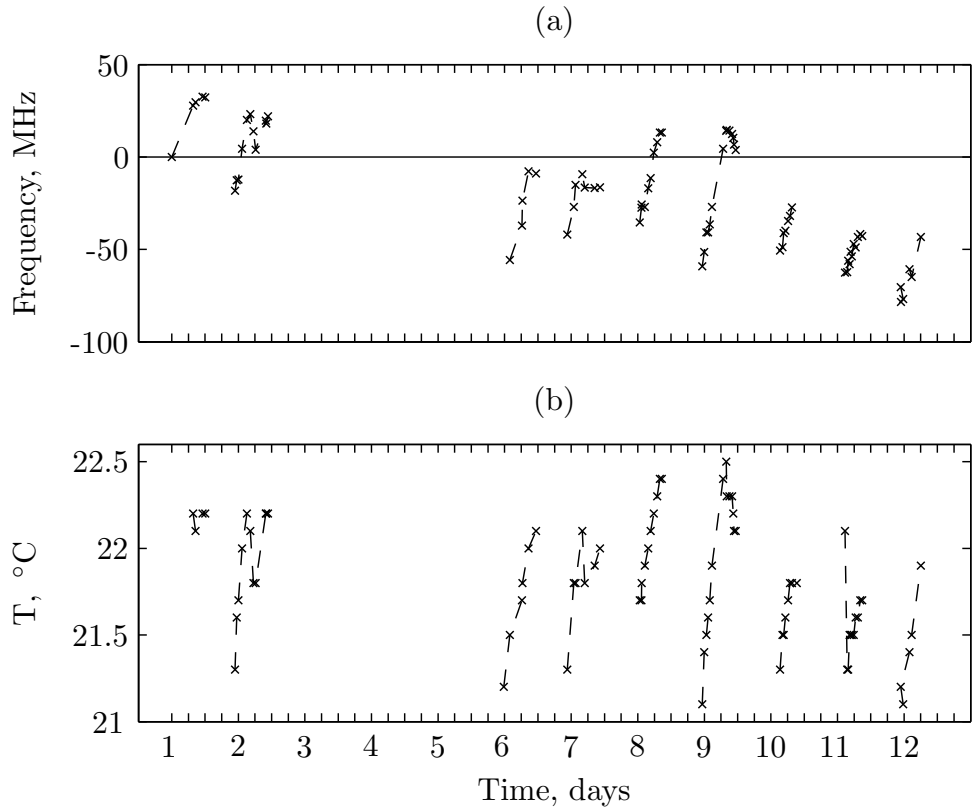

Figure 10.9: Frequency drift measurement under (leaking) vacuum conditions. The top graph (a) shows the drift of the transmission peak in MHz vs. time and the bottom graph (b) the air temperature on the outside of the vacuum cell in °C. Both plots refer to the same time axis explicitly plotted in figure (b).

in figure 10.9 (a) to loss of vacuum in the system. From figure 10.11, we can approximate an overall drift of (-5 ± 2) MHz/day, when using a linear approach that assumes a constant pressure increase. We note that over the course of 12 days, the transmission peak is shifted by approximately -80 MHz. Using our analysis from section 10.1, where we show the frequency drift dependence on changes in air pressure and temperature for the ideal gas, this corresponds to an increase in pressure of approximately 1 mbar. From the leakage rate derived in section 10.3.1 on page 85, where we study the quality of the vacuum, we can expect a residual pressure of 5 mbar inside the vacuum housing, which seems to be consistent with the vacuum quality we observed all along.

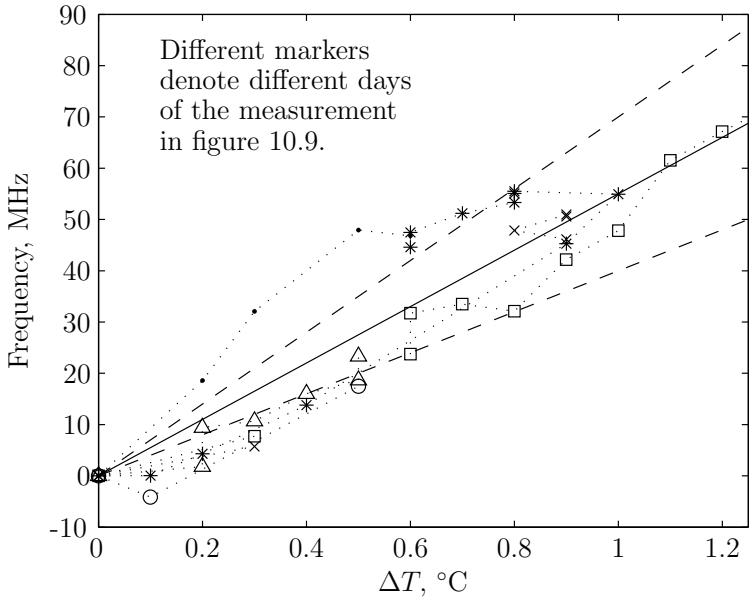

Figure 10.10: The drift of the cavity transmission displayed in figure 10.9 shows a distinct temperature dependence. For each day, the change in temperature is plotted along with the corresponding frequency drift. We arrive at a correlation of (55 ± 15) MHz/K, which is marked by the solid and dashed lines.

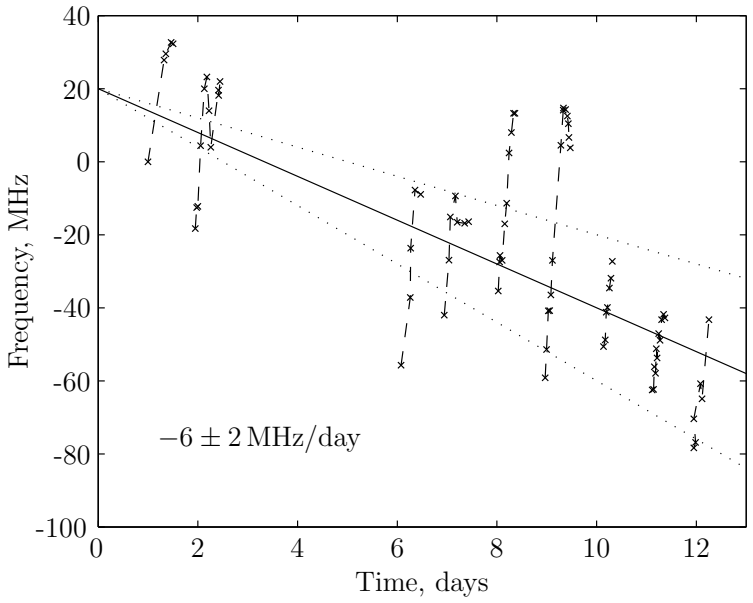

Figure 10.11: Estimate of overall frequency drift of cavity transmission in (leaking) vacuum. The plot shows the same data as graph (a) in figure 10.9. Besides the daily temperature induced behavior, the slow loss of vacuum causes a decrease of the transmission frequency. The frequency drift is estimated as approximately -6 MHz/day, and a rough error of ± 2 MHz/day is given for illustration purposes by dotted lines. Here, the top line denotes -4 MHz/day and the bottom one -8 MHz/day.

For the purpose of the laser lock, the achieved long–term stability within $-6\,\mathrm{MHz}$ overall drift per day is acceptable. The deviation can, if desirable, be counteracted by changing the effective cavity length by applying a constant voltage to one of the cavity piezo–electric transducers (PZT).

10.4.3 Fully stabilized cavity

When employing the temperature stabilization and allowing the system sufficient time to rethermalize, we can minimize the short and long–term fluctuations of the transmission frequency. The results of our measurements are shown in figures 10.12 to 10.14. Over 35 hours the total frequency drift amounts to approximately $-5\,\mathrm{MHz}$. Sudden changes in temperature or cavity length result in immediate changes of the transmission frequency.

The measurement presented in figure 10.12 shows frequency data taken over two days and the corresponding temperature deviations of the vacuum tube (inside NTC) and the outer stovepipe housing (outside NTC). The resistivity readings have been converted into temperatures. The system had been temperature stabilized for 24 hours before the measurement, and the vacuum body had been evacuated, with the pump running during the measurement. The readings of the frequency drift signal were taken at the same time as the temperature reading, averaging to one data set per hour during daytime. Our data gives insight to the general trend and amplitude of the frequency drift and temperature fluctuation of the heating circuit.

The first part of the frequency data set displays a linear drift of $-0.2\,\mathrm{MHz}$ per hour, the second day $-0.06\,\mathrm{MHz}$ per hour. The uncertainty around this linear approximation is $\pm 1\,\mathrm{MHz}$. We refrained from applying one (non–linear) function to all of the data as the laser drifted off resonance overnight and a different transmission peak was observed on the second day. Accounting for this, the overall shift in 35 hours adds up to approximately $-5\,\mathrm{MHz}$. This corresponds to a drift of $-4\,\mathrm{MHz}$ per day which is acceptable for the experimental applications.

The temperature of the inside heating circuit varies by $\pm 20\,\mathrm{mK}$ on the order of one day and the temperature of the stovepipe housing (outside) by $\pm 20\,\mathrm{mK}$ on the order of 2 hours. This fulfills our expectation that the outer temperature is subject to fluctuations with larger frequencies that are compensated for by the inner heating circuit. We note that the trend of the transmission frequency drift roughly corresponds to the trend of the inner temperature reading for both days. From this, obtain a value on the order of $-50\,\mathrm{MHz/K}$ and $-25\,\mathrm{MHz/K}$, respectively, for the temperature dependence of the transmission frequency. This is in agreement with the thermal contraction of the

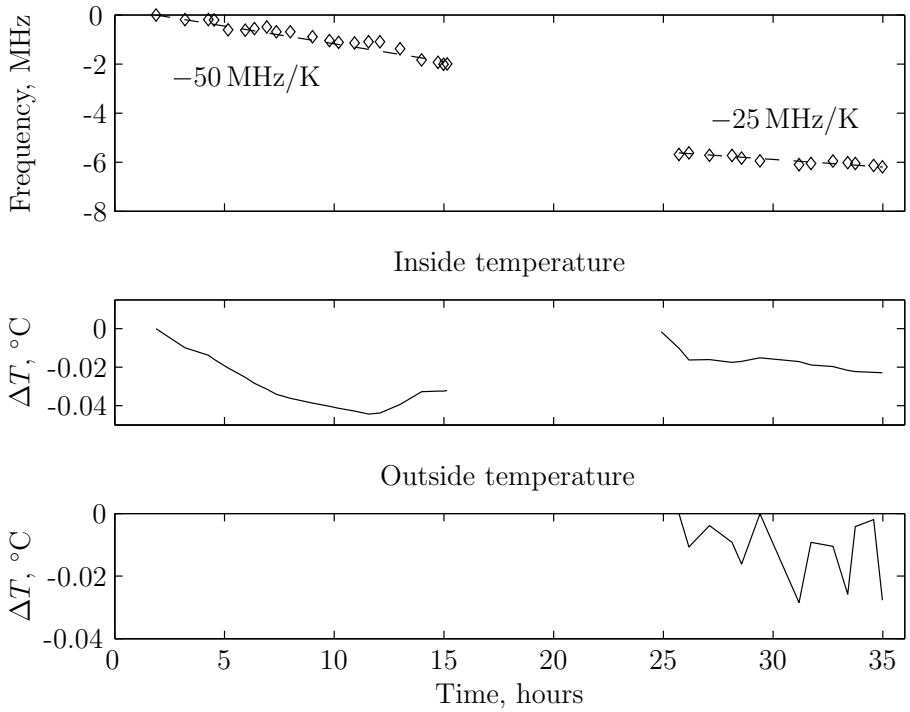

Figure 10.12: Results of frequency drift under temperature– and pressure–stabilized conditions. The drift of the transmission frequency is shown over the course of 35 hours. The temperature variation (derived from the monitoring NTCs) of the outer and inner heating circuit are shown, where we only took data of the outside stage in the last 10 hours of the measurement.

cavity of $\mp 40\,\mathrm{MHz/K}$, which is derived in section 10.1. It remains unclear why the drift seems to trend towards smaller values over the course of the measurement. We believe that the continuous pumping was still improving the vacuum conditions when we took the data. Secondarily, we believe that the frequency drift can be improved by reducing the amplitude of the temperature fluctuations imposed by the controlling circuit, which are on the same order as the fluctuations observed here. It is possible to lengthen the tune–in time, and gain a larger sensitivity in return, as described in section 10.3.2.

We explore the explicit temperature dependence of the transmission frequency on a short and intermediate time scale. The result is given in figure 10.13. We deliberately changed the reference value of the inside temperature circuit by $\Delta T = +0.6\,\mathrm{K}$. The inset in figure 10.13 shows that the transmission frequency reacts within 5 minutes and that the transmission frequency begins to increase, as would be expected from the heated cavity and the air

inside it. Initially, the frequency increases at 30 MHz/hour. After approximately 120 minutes, the transmission frequency arrives at the final value of $\sim$ 32 MHz, where we assume the system to have rethermalized. The data points are scattered with an amplitude of ± 2 MHz, which is within the resolution limit we expect. We observe a total frequency drift of 53 MHz/K and this is in accordance with the thermal expansion of the used materials. We observe the transmission frequency to react quickly to the external disturbance of a changed temperature, but it takes a considerably long time for the cavity to arrive at a new equilibrium state. The temperature control should remain in place at all times when the laser lock is used for experiments.

The measurement presented in figure 10.14 shows the behavior of the cavity to applying a constant voltage of 50 V to one of the cavity PZTs for 13 minutes. The transmission frequency instantly jumps to approximately -700 MHz, where it fluctuates with an amplitude of ± 20 MHz, as the bottom inset picture in figure 10.14 shows. With the PZT voltage turned off, the transmission instantly jumps to the starting value within -30 MHz. From there, the system takes about one hour to fully return to its original state. The last data points presented in the last 20 minutes of the measurement fluctuate with an amplitude of ± 3 MHz, which within the measurement resolution, corresponds to the arrival in the steady state. The slow leveling off into the steady state is caused by a hysteresis effect (displacement vs. applied voltage) that is intrinsic to PZT materials.

The response of the cavity to external disturbances in the form of an overall temperature change and jump to different cavity length is within the expected range and our results are satisfactory.

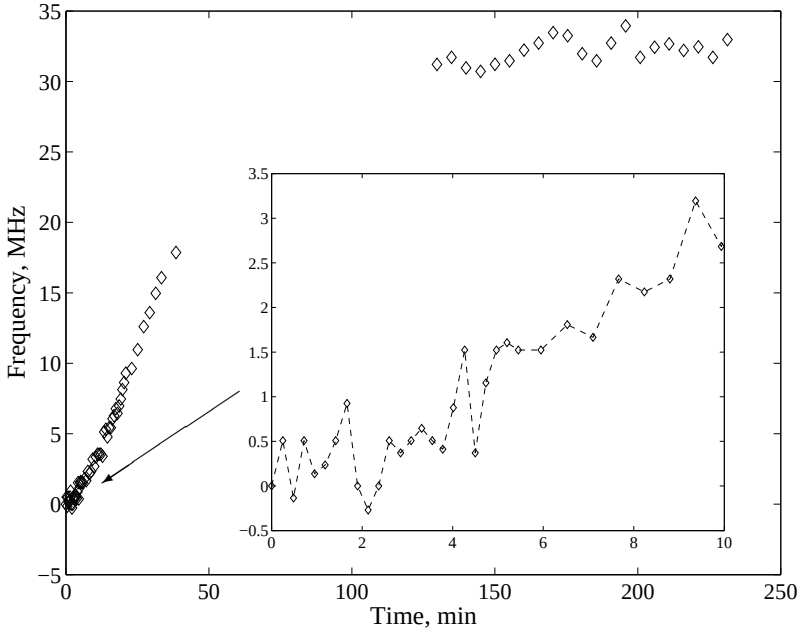

Figure 10.13: Drift of cavity transmission upon deliberate temperature change of the inside heating circuit of $\Delta T = +0.6\,\mathrm{K}$ at $t = 0$. The inset shows that the system reacts to the temperature change within 5 minutes.

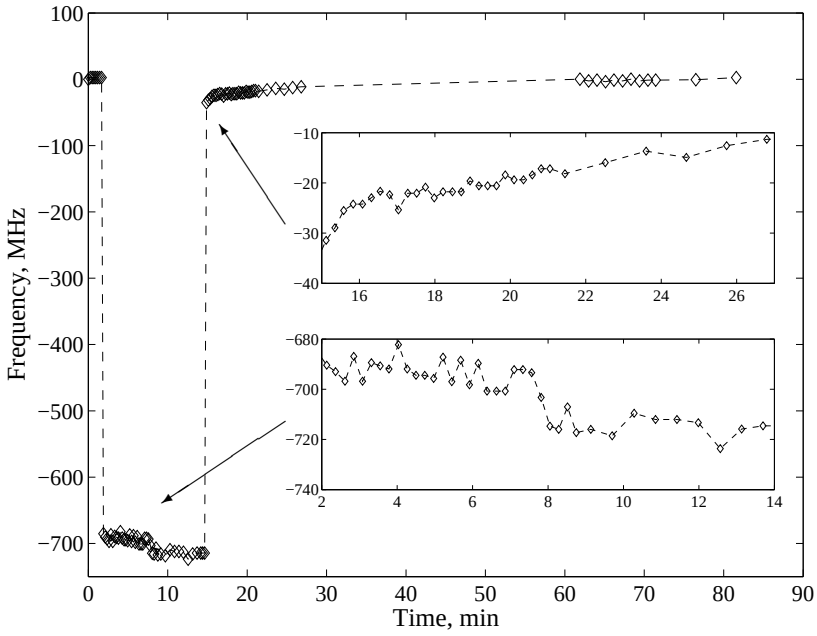

Figure 10.14: Drift of cavity transmission upon applying a pulsed PZT voltage of 50 V with a pulse length of 13 minutes. The insets show the detailed behavior while the voltage is applied and after it has been turned off.

Chapter 11

Conclusions

In the second part of this thesis, the implementation of a frequency stabilizing scheme using an optical mirror cavity and the Pound–Drever–Hall technique is documented. An introduction to the fundamentals of optical mirror cavities and the Pound–Drever–Hall method were given. We introduce the experimental setup for the laser lock and the components thereof. The performance of the lock was tested and we arrived at a satisfactorily result of a frequency stability within 140 kHz. The stability on the timescale of hours and days was studied. We described saturation spectroscopy on rubidium, which is used to determine the drift qualitatively. With evacuation of the housing and an active, two stage temperature stabilization, we could limit the long–term frequency drift to 5 MHz per day.

The laser lock is used as part of the experimental setup to generate a three–dimensional optical lattice potential and create the Mott insulating state starting from a ^{87}Rb BEC. In the "Ultracold atoms and quantum gases group" at the University of Innsbruck, Austria, experiments focussing on molecule formation in optical lattices are currently underway.

Part III

Appendix

Appendix A

Code listings

The presented MATLAB code is based onto functions previously written by Jos Martin and extended by Nick Thomas.

```
%b_combinefit.m
% Calls upon coiloptions.m to define coils stack and b_loop_ex.m to
%calculate the axial magnetic field due to one Ioffe coil along the
%z-axis and a quadrupole field with two identical coils along the
%x-axis.
%This version takes a few minutes to compute, as the field is fitted
%along all three directions to obtain results for radial confinement.

% Dec, 2003 Ina Kinski
%-------------------------------------------------------------------
%%DEFINITION OF WIRE RADIUS
rad=1.2; %real wire diameter
rad2=rad*0.87; %effective wire diameter in radial direction

%%DEFINITION OF CURRENT THROUGH COILS
currenti=25; %through Ioffe coil
current=25; %through quads
%%% Matrices containing current
Ii=currenti*ones(1, length(Ai));
Ih=current*ones(1, length(Ah));

%% IOFFE COIL %%%%%%%%%%%%%%%%%%%%%%%%%%%%%%%%%%%%%%%%%%%%%%%%%%%%%%%%
a1=31.07;%distance from first turn of the Ioffe coil to origin
Ni = 15;        %number of layers along symmetry axis
Nli=[22 22 22 22 22 22 22 15 15 15 15 15 7 7 7];
%varying number of layers from back to front
radiusi = (13+[0:rad2:14.616])*1e-3;
```

```
28  %radius of smallest to biggest radius. Must have same size as Ni
29  disti = [a1+rad*(0:Nli(1)-1)]*1e-3;
30  %smallest to largest distance of each turn to origin, same number as Nli
31  Ri = [];
32  Ai = [];
33  for i = 1:Ni;
34     for j = 1:Nli(i);
35        Ri = [Ri radiusi(i)];
36        Ai = [Ai disti(j)];
37     end
38  end
39  Ai=-(Ai-max(Ai))+disti(1);
40  %Correct position on axis, where disti(1) is the distance of closest
41  %turn to centre
42
43  %%INSERTION OF METAL DIVIDERS
44  Ii(:,[7:22:161,176:15:236,243,250])=0;
45  Ii(:,[15:22:169,184:15:229])=0;
46  Ii(:,[1:1:15,23:1:37,45:1:59,67:1:81,89:1:103,111:1:125,133:1:147])=0;
47  Ii(:,[155:1:160,170:1:175,185:1:190,200:1:205,215:1:220])=0;
48  w=find(Ii>0);
49  %%%%%%%%%%%%%%%%%%%%%%%%%%%%%%%%%%%%%%%%%%%%%%%%%%%%%%%%%%%%%%%%%%%%%%%%
50
51
52  %% QUADRUPOLE COILS %%%%%%%%%%%%%%%%%%%%%%%%%%%%%%%%%%%%%%%%%%%%%%%%%%%
53  a2 =(16.1+[0:rad2:32.364])*1e-3;
54  Nh = 5;
55  Nlh = repmat(32,5,1)';
56  radiush =(13+[0:rad:4.8])*1e-3;
57  Rh = [];
58  Ah = [];
59  for i = 1:Nh;
60     for j = 1:Nlh(i);
61        Rh = [Rh radiush(i)];
62        Ah = [Ah a2(j)];
63     end
64  end
65  v=find(Ih>0);
66  %%%%%%%%%%%%%%%%%%%%%%%%%%%%%%%%%%%%%%%%%%%%%%%%%%%%%%%%%%%%%%%%%%%%%%%%
67
68
69  %%%%PREP FOR EVALUATION %%%%%%%%%%%%%%%%%%%%%%%%%%%%%%%%%%%%%%%%%%%%%%
70  n=50;%Even number of points to evaluate at!
```

```
71  fitparameter=1e-3;%Stepsize of fit around z-axis minimum
72  %%% Calculate number of windings
73  Ioffe_windings=sum(Ii)/currenti
74  Helm_windings=sum(Ih)/current
75  %%%Plotting range in m
76  zmax=(a1-0.1)*1e-3;
77  xmax=5*1e-3;
78  ymax=5*1e-3;
79  [x z y]=meshgrid(linspace(-xmax,xmax,2*n+1),linspace(-zmax,zmax,2*n+1),...
80      linspace(-ymax,ymax,n+1));
81  ax=find(y==0 & z==0);
82  ay=find(x==0 & z==0);
83  az=find(y==0 & x==0);
84
85  %%% CALCULATE COILS %%%%%%%%%%%%%%%%%%%%%%%%%%%%%%%%%%%%%%%%%%%%%%%%%%%%
86  coili = coiloptions(Ai,Ri,Ii,[0 0 1]);
87  [bfi,bfxi,bfyi,bfzi] = b_loop_ex(coili,x,y,z);
88  coilh = coiloptions([Ah -Ah],[Rh Rh],[Ih -Ih],[1 0 0]);
89  [bf,bfx,bfy,bfz] = b_loop_ex(coilh,x,y,z);
90
91  %%% ADD UP COMBINED VALUES %%%%%%%%%%%%%%%%%%%%%%%%%%%%%%%%%%%%%%%%%%%%
92  bx=bfxi+bfx; by=bfyi+bfy; bz=bfzi+bfz; b=sqrt(bx.^2+by.^2+bz.^2);
93
94  %%% FIT IN Z-DIRECTION %%%%%%%%%%%%%%%%%%%%%%%%%%%%%%%%%%%%%%%%%%%%%%%%
95  zfit=z(az); bzfit=bz(az);
96  bzmin=min(bzfit);
97  zmin=zfit(find(bzfit==bzmin))
98  zfit=zfit-zmin;
99  ZZ=find(abs(zfit)<fitparameter);
100 fit1=polyfit(zfit(ZZ)*1e2,bzfit(ZZ),3); %into G/cm
101 %% meshgrid around minimum
102 axfit=find(y==0 & z==zmin);
103 ayfit=find(x==0 & z==zmin);
104 azfit=find(y==0 & x==0);
105
106 %FIT IN X AND Y AROUND MINIMUM FOUND ON Z-AXIS  %%%%%%%%%%%%%%%%%%%%%
107 xfit=x(axfit); bxfit=b(axfit); XX=find(abs(xfit)<fitparameter);
108 fit2=polyfit(xfit(XX)*1e2,bxfit(XX),3);
109 yfit=y(ayfit); byfit=b(ayfit); YY=find(abs(yfit)<fitparameter);
110 fit3=polyfit(yfit(YY)*1e2,byfit(YY),3);
111
112 %%% PLOT OF FIT IN ALL THREE DIRECTIONS %%%%%%%%%%%%%%%%%%%%%%%%%%%%%%
113 figure(1)
```

```
114  subplot(2,2,1), plot (zfit,bzfit,'r',zfit(ZZ),polyval(fit1,zfit(ZZ)*1e2),'b')
115  xlim([-0.002 0.002]);legend('Bz','Fit')
116  subplot(2,2,3), plot (xfit,bxfit,'r',xfit(XX),polyval(fit2,xfit(XX)*1e2),'b')
117  xlim([-0.002 0.002]);legend('B,x','Fit')
118  subplot(2,2,4), plot (yfit,byfit,'r',yfit(YY),polyval(fit3,yfit(YY)*1e2),'b')
119  xlim([-0.002 0.002]); legend('B,y','Fit')
120
121  %%% OUTPUT: BIAS FIELD, GRADIENT, CURVATURE,... %%%%%%%%%%%%%%%%%%%%
122  %Offset fields:
123  bznot=fit1(4)
124  bxnot=fit2(4)
125  bynot=fit3(4)
126  thirdz=fit1(1); thirdx=fit2(1); thirdy=fit3(1);
127  %Gradients:
128  bxprime=fit2(3);byprime=fit3(3);bzprime=fit1(3)
129  %Curvatures:
130  bxdblprime=2*fit2(2)
131  bydblprime=2*fit3(2)
132  bzdblprime=2*fit1(2)
133  %Radial gradient:
134  radialgrad=(bznot*(bxdblprime+(bzdblprime/2)))^(1/2)
135  % Anisotropy
136  aniso=(bxdblprime/bzdblprime)^(1/2)
137  % Trapping frequencies
138  mass=1.44e-25; muh=9.274e-24; prefactor=(muh/mass)^(1/2);
139  omegaz=prefactor/(2*pi)*(2*fit1(2))^(1/2)
140  omegax=prefactor/(2*pi)*(2*fit2(2))^(1/2)
141  omegay=prefactor/(2*pi)*(2*fit3(2))^(1/2)
142  %Mean average omega
143  omegaav=prefactor/(2*pi)*(fit1(2)*fit2(2)*fit3(2))^(1/6)
144  %Power consumption for both coils
145  rhocopper=0.0175; area=(rad/2)^2*pi;
146  langei=sum(sum(2*pi*Ri(w))); langeh=sum(sum(2*pi*Rh(v)));
147  resisti=(rhocopper*langei)/area; resisth=(rhocopper*langeh)/area;
148  Power_i=resisti*(currenti^2)
149  Power_h=resisth*(current^2)
150
151  %%%%%%%%%%%%%%%%%%%%%%%%%%%%%%%%%%%%%%%%%%%%%%%%%%%%%%%%%%%%%%%%%%%%%%%
152
153  %PLOT OF AXIAL FIELDS, AND SURF PLOT
154  figure(2);
155  subplot(3,3,1); plot(x(axfit)./1e-2, bx(axfit),x(axfit)./1e-2,...
156      bfxi(axfit),x(axfit)./1e-2, bfx(axfit))
```

```
157       grid; title('blue:sum, green:Ioffe, red:Helmholtz');
158       xlabel('x-axis, cm'); ylabel('Axial Magnetic Field, G')
159   subplot(3,3,2), plot(y(ayfit)./1e-2, by(ayfit),y(ayfit)./1e-2,...
160       bfyi(ayfit),y(ayfit)./1e-2, bfy(ayfit))
161       grid; title(sprintf('I=%1.2f B''''(z)=%1.2f B0=%1.2f',current,...
162           bzdblprime,bznot))
163       xlabel('y-axis, cm'); ylabel('Axial Magnetic Field, G')
164   subplot(3,3,3), plot(z(azfit)./1e-2, bz(azfit),z(azfit)./1e-2,...
165       bfzi(azfit),z(azfit)./1e-2, bfz(azfit));
166       title(sprintf('B""(x)=%1.2f B""(y)=%1.2f',bxdblprime,bydblprime))
167       grid;ylim([-20 20]);
168       xlabel('z-axis, cm'); ylabel('Axial Magnetic Field, G')
169   %%Extracting for surf plot, set bfield cutoff
170   xs=x(:,:,(n/2)+1); ys=y(:,:,(n/2)+1); zs=z(:,:,(n/2)+1); bs=b(:,:,(n/2)+1);
171   bfis=bfi(:,:,(n/2)+1); bfs=bf(:,:,(n/2)+1); bfis(find(bfis>600))=NaN;
172   bfs(find(bfs>600))=NaN;bs(find(bs>600))=NaN;
173   %%%
174
175   subplot(3,3,4), surfc(xs./1e-2,zs./1e-2, bfis); view([108 18]); shading flat
176       xlabel('x, cm'); ylabel('z, cm'); zlabel('Abs value B, G')
177   subplot(3,3,7), surfc(xs./1e-2,zs./1e-2, bfs); view([108 18]); shading flat
178       xlabel('x, cm'); ylabel('z, cm'); zlabel('Abs value B, G')
179   subplot(3,3,[5 6 8 9]), surfc(xs./1e-2,zs./1e-2, bs); view([108 18])
180   shading flat; title(['All three combined']); xlabel('x-axis, cm');
181   ylabel('z-axis, cm'); zlabel('Abs value B, G');
182
183   %PLOT OF COIL POSITION & SCIENCE CELL
184   figure(3);clf
185   i1=[Ai(w);Ri(w)]'; i2=[Ai(w);Ri(w)*(-1)]'; ioffePLOT=[i1;i2];
186   h1=[Ah(v);Rh(v)]'; h2=[Ah(v)*(-1);Rh(v)]'; h3=[Ah(v);Rh(v)*(-1)]';
187       h4=[Ah(v)*(-1);Rh(v)*(-1)]'; helmPLOT=[h1;h2;h3;h4];
188   plot(ioffePLOT(:,1)*1e3,ioffePLOT(:,2)*1e3,'x',helmPLOT(:,2)*1e3,...
189       helmPLOT(:,1)*1e3,'x')
190   hold on;
191   %plot cell
192   plot([-35 -35],[-10 10],'r'); plot([35 35],[-10 10],'r');
193   plot([35 -35],[10 10],'r'); plot([35 -35],[-10 -10],'r');
194   xlabel('z-axis, mm'); ylabel('x-axis, mm'); axis equal
195   xlim([-46 80]); ylim([-44 44]); grid on; hold off
```

```
function Coil = CoilOptions(A,R,I,Z_axis,Coil_centre)
%Coil = CoilProp(A,R,I,Z_axis,Coil_centre)
%
%This function returns a structure suitable for use in B_Loop_Ex.
%This structure represents a series of coils lying along the axis
%Z_axis with the vectors A,R and I representing the distance from
%the co-ordinate origin, the radius and the current respectively.
%
%CoilOptions.m - Matlab 5.1 - Jos Martin - March 1999

if size(A) ~= size(R) & size(R) ~= size(I)
   error('A, R and I must be the same size');
end

if size(Z_axis) ~= [1 3]
   error('Z_axis must be a 1x3 vector');
end

Coil.A = A;
Coil.R = R;
Coil.I = I;
Coil.Z_axis = Z_axis;
if nargin < 5
   Coil.Coil_centre = Z_axis;
else
   Coil.Coil_centre = Coil_centre;
end
```

```
function [Br, Bz] = B_loop(A,R,I,z,rho)
%[Br, Bz] = B_loop(A,R,I,z,rho)
%
% Calculates axial magnetic field for a coil from exact expression
% derived from integral over vector potential A.
% Uses polar coordinate system.
%
% where A = Axial coil Position in m
%       R = Coil Radius in m (coil centred on axis)
%       I = Current in coil in A
%       z = axial position to calculate field at
%       rho = radial position to calcluate field at
%
```

```
14  % returns Br,Bz = radial and axial field in Tesla
15  %
16  % b_loop.m - Matlab 5.1 - Jos Martin - March 1999
17  %
18  %(from NRT Br_loop.m and Bz_loop, optimised)
19
20  % consts
21  mu0 = 4e-7 * pi;                % permeability of free space
22  factor1 = (mu0 * I)/(2 * pi);
23  global tol
24  % calculation
25  Z2 = (z-A).^2;
26  k2_denom = 1./((R+rho).^2 + Z2);
27
28  factor1_r = factor1./rho;
29  factor2 = sqrt(k2_denom);
30
31  k2 =  (4 * R * rho).* k2_denom;
32  [K,E] = ellipke(k2,eps); clear k2_denom k2
33
34  factor3 = E./((R-rho).^2 + Z2);
35
36  factor3_R2 = factor3*R^2;
37  factor3_r2Z2 = factor3.*(rho.^2 + Z2); clear factor3 Z2 rho
38
39  factor3_r = -K + factor3_R2 + factor3_r2Z2;
40  factor3_z =  K + factor3_R2 - factor3_r2Z2;
41
42  clear K E factor3_R2 factor3_r2Z2
43
44  Br = factor1_r.*((z-A).*factor2).*factor3_r;
45  clear z factor1_r factor3_r
46  Br = excise(Br);
47
48  Bz = factor1*factor2.*factor3_z;
```

```
function [B,Bx,By,Bz] = b_loop_ex(Coils,X,Y,Z)
%Calculates the vector magnetic field and the magnitude
%for a series of coils.
%
%Coils is a vector of structures. Each element of Coils has the following form
% Z_axis  (1x3) : The direction of the axis of the coils
% A       (MxN) : The distance from the origin to the centre of each coil
% R       (MxN) : The radius of each coil
% I       (MxN) : The current in each coil
%
%Individual elements of Coils can be created using CoilOptions.
%
%Note the vector Z_axis should be defined with respect
%to the co-ordinate system X,Y,Z. This function transforms to the
%coils cylindrical co-ordinate system, calculates B_z and B_rho using
%B_loop and then transforms back to the original co-ordinate system
%
%B_Loop_Ex.m - Matlab 5.1 - Jos Martin - March 1999

Bx_total = zeros(size(X));
% Initialise B_total's to correct size
By_total = Bx_total;
Bz_total = Bx_total;

warning off
for i = 1:length(Coils) % Length(Coils) is the number of different axis
   A = Coils(i).A(:);   % Ensure that A,R and I are column vectors ...
   R = Coils(i).R(:);
   I = Coils(i).I(:);
   Z_axis = Coils(i).Z_axis;
        Coil_centre = Coils(i).Coil_centre;

        if length(A) ~= length(R) & length(R) ~= length(I)
        error('A, R and I must have the same number of entries')
        end

        [L,v] = axial2cartmatrix(Z_axis,Coil_centre);
        % Get transformation matrix L

        Brho  = zeros(size(X));
        % Initialise B's to correct size
        BzPol = Brho;

```

```
44          [theta,rho,zPol] = cart2axial(X,Y,Z,inv(L),v);
45          % Transform to cylindrical co-ord with L^-1
46
47          for j = 1:length(A)
48          % Evaluate B_r and B_z for each coil and remove
49          % any infinities introduced
50        [Brho_t,BzPol_t] = b_loop(A(j),R(j),I(j),zPol,rho);
51                   Brho  = Brho  + Brho_t;
52          BzPol = BzPol + BzPol_t;
53          end
54
55          [Bx,By,Bz] = axial2cart(theta,Brho,BzPol,L);
56          % Transform back to Cartesian co-ord with L
57
58          Bx_total = Bx_total + Bx;
59     By_total = By_total + By;
60     Bz_total = Bz_total + Bz;
61   end
62   warning on
63
64   Bx = Bx_total*1e4;
65   By = By_total*1e4;
66   Bz = Bz_total*1e4;
67   B = sqrt(Bx.^2 + By.^2 + Bz.^2);
```

```
1    % excise.m - 15/4/97
2    % code as per phd thesis of Jocelyn L. Martin
3    %
4    % removes infinities and NaN's from input matrix
5
6    function a = excise(a)
7
8    sz = size(a);
9    a = a(:);
10   a(find(1-finite(a))) = 0;
11   a = reshape(a,sz);
```

Appendix B

Additional information

A partial rubidium energy level scheme and the construction drawings for the the ceramic rings that support the piezo stack of the cavity are shown on the following pages.

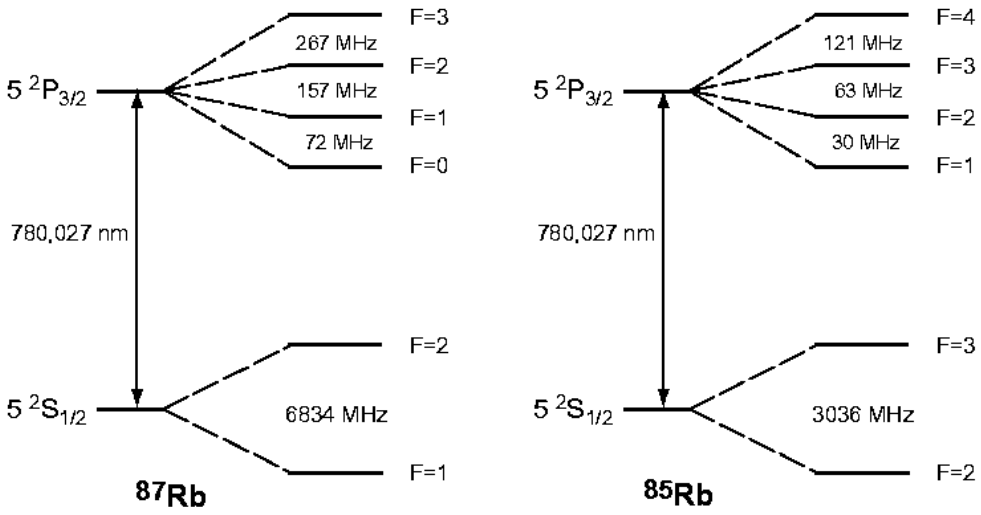

Figure B.1: Partial rubidium level scheme of the D_2-line, which is the transition from the $^5S_{1/2}$ ground state to the $^5P_{3/2}$ excited state. Taken from literature for the Advanced Lab Course in Innsbruck, Chr. Roos.

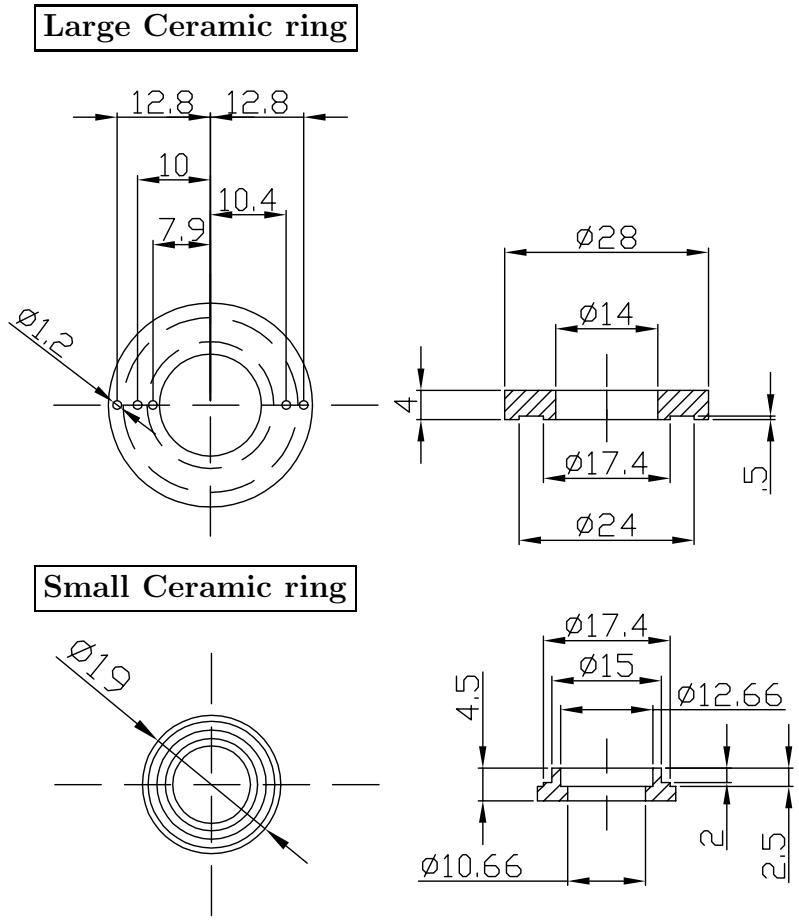

Figure B.2: The figure shows the construction plans for the ceramic rings used for the optical cavity. The arrangement is shown in figure 9.3 on page 64. The rings, which are made from Macor ceramic (obtainable at RS components) hold the PZT stack and output mirror in place. The top row shows the larger rings in front view and cross-section. The feed through holes for electrical wiring is shown. The smaller ring is shown in the bottom row. Again, front view and cross-section are illustrated. All dimensions are given in mm. The drawings were done and made available to us by Ferdinand Schmidt-Kaler.

Bibliography

[And95] M. Anderson, J. Ensher, M. Matthews, C. Wieman, and E. Cornell, *Observation of Bose-Einstein condensation in a dilute atomic vapor*, Science **269**, 198 (1995).

[Bar04] M. Bartenstein, A. Altmeyer, S. Riedel, S. Jochim, C. Chin, J. H. Denschlag, and R. Grimm, *Crossover from a molecular Bose-Einstein condensate to a degenerate Fermi gas*, Phys. Rev. Lett. **92**, 120401 (2004).

[Ber87] T. Bergeman, G. Erez, and H. Metcalf, *Magnetostatic trapping for neutral atoms*, Phys. Rev. A **35**, 1535 (1987).

[Bjo83] G. Bjorklund, M. Levenson, W. Lenth, and C. Ortiz, *Frequency Modulation (FM) Spectroscopy - Theory of Lineshapes and Signal-to-Noise Analysis*, Appl. Phys. B **32**, 145 (1983).

[Bos24] S. Bose, *Plancks Gesetz und Lichtquantenhypothese (translated by A. Einstein)*, Zeitschrift für Physik **26**, 178 (1924).

[Cir04] J. Cirac and P. Zoller, *New Frontiers in Quantum Information With Atoms and Ions*, Physics Today **57**, 38 (2004).

[Dav95] K. Davis, M.-O. Mewes, M. Andrews, N. van Druten, D. Durfee, D. Kurn, and W. Ketterle, *Bose-Einstein condensation in a gas of sodium atoms*, Phys. Rev. Lett. **75**, 3969 (1995).

[Dem93] W. Demtröder, *Laserspektroskopie - Grundlagen und Techniken*, Springer Verlag, Heidelberg (1993).

[Don02] E. Donley, N. Claussen, S. Thompson, and C. Wieman, *Atom-Molecule Coherence in a Bose-Einstein Condensate*, Nature **417**, 529 (2002).

[Dre83] R. Drever, J. Hall, F. Kowalski, J. Hough, G. Ford, A. Munley, and H. Ward, *Laser phase and frequency stabilization using an optical resonator*, Appl. Phys. B **31(2)**, 97 (1983).

[Ein25] A. Einstein, *Quantentheorie des einatomigen idealen gases, Zweite Abhandlung*, Sitzungsbericht Königliche Preussische Akademie der Wissenschaften **3**, 3 (1925).

[Ens98] J. Ensher, *The First Experiments with Bose-Einstein Condensation of 87Rb*, Dissertation in the Physics Department of the University of Colorado, JILA (1998).

[Ess98] T. Esslinger, I. Bloch, and T. Hänsch, *Bose-Einstein condensation in a quadrupole-Ioffe-configuration trap*, Phys. Rev. A **58**, R2664 (1998).

[Gre01] M. Greiner, I. Bloch, T. Hänsch, and T. Esslinger, *Magnetic transport of trapped cold atoms over a large distance*, Phys. Rev. A **63**, 031401(R) (2001).

[Gre02] M. Greiner, O. Mandel, T. Esslinger, T. Hänsch, and I. Bloch, *Quantum phase transition from a superfluid to a Mott insulator in a gas of ultracold atoms*, Nature **415**, 39 (2002).

[Gre03] M. Greiner, *Ultracold quantum gases in three-dimensional optical lattice potentials*, Dissertation in the Physics department of LMU Munich (2003).

[Gri00] R. Grimm, M. Weidemüller, and Y. Ovchinnikov, *Optical Dipole Traps for Neutral Atoms*, Adv. At. Mol. Opt. Phys. **42**, 95 (2000).

[Gri05] A. Griesmaier, J. Werner, S. Hensler, J. Stuhler, and T. Pfau, *Bose-Einstein condensation of chromium*, cond-mat/ 0503044 (2005).

[Jak98] D. Jaksch, C. Bruder, J. Cirac, C. Gardiner, and P. Zoller, *Cold bosonic atoms in optical lattices*, Phys. Rev. Lett. **81**, 3108 (1998).

[Jak99] D. Jaksch, H. Briegel, J. Cirac, C. Gardiner, and P. Zoller, *Entanglement of atoms via cold controlled collisions*, Phys. Rev. Lett. **82**, 1975 (1999).

[Jak02] D. Jaksch, V. Venturi, J. Cirac, C. Williams, and P. Zoller, *Creation of a molecular condensate by dynamically melting a Mott insulator*, Phys. Rev. Lett. **89**, 040402 (2002).

[Joc03] S. Jochim, M. Bartenstein, A. Altmeyer, G. Hendl, S. Riedl, C. Chin, J. H. Denschlag, and R. Grimm, *Bose-Einstein Condensation of Molecules*, Science **302**, 2101 (2003).

[Ket99] W. Ketterle, D. Durfee, and D. Stamper-Kurn, *Making, Probing and Understanding Bose-Einstein Condensates*, Proceedings of the International School of Physics "Enrico Fermi" - Bose-Einstein Condensation in Atomic Gases, cond–mat/9904034v2 (1999).

[Kin04] T. Kinoshita, T. Wenger, and D. Weiss, *Observation of a One-Dimensional Tonks-Girardeau Gas*, Science **305**, 1125 (2004).

[Lew03] H. Lewandowski, D. Harber, D. Whitaker, and E. Cornell, *Simplified System for Creating a Bose Einstein Condensate*, JLTP **132(5-6)**, 309 (2003).

[Maj32] E. Majorana, *Atomi Orientati in Campo Magnetico Variabile*, Nuovo Cimento **9**, 43 (1932).

[Man03a] O. Mandel, M. Greiner, A. Widera, T. Rom, T. Hänsch, and I. Bloch, *Coherent transport of neutral atoms in spin-dependent optical lattice potentials*, Phys. Rev. Lett. **91**, 010407 (2003).

[Man03b] O. Mandel, M. Greiner, A. Widera, T. Rom, T. Hänsch, and I. Bloch, *Controlled collisions for multi-particle entanglement of optically trapped atoms*, Nature **425**, 937 (2003).

[Mig85] A. Migdal, J. Prodan, W. Phillips, T. Bergemann, and H. Metcalf, *First observation of magnetically trapped neutral atoms*, Phys. Rev. A **54**, 2596 (1985).

[Par04] B. Paredes, A. Widera, V. Murg, O. Mandel, S. Fölling, I. Cirac, G. Shlyapnikov, T. Hänsch, and I. Bloch, *Tonks-Girardeau gas of ultracold atoms in an optical lattice*, Nature **429**, 277 (2004).

[Pet95] W. Petrich, M. Anderson, J. Ensher, and E. Cornell, *Stable, Tightly Confining Magnetic Trap for Evaporative Cooling of Neutral Atoms*, Phys. Rev. A **74**, 3352 (1995).

[Pou46] R. Pound, *Electronic frequency stabilization of microwave osciallators*, Rev. Sci. Instrum. **17**, 490 (1946).

[Pri84] D. Pritchard, *Cooling neutral atoms in a magnetic trap for precision spectroscopy*, Phys. Rev. Lett. **51**, 1336 (1984).

[Raa87] E. Raab, M. Prentiss, A. Cable, S. Chu, and D. Pritchard, *Trapping of Neutral Sodium Atoms with Radiation Pressure*, Phys. Rev. Lett. **59**, 2631 (1987).

[Reg04] C. Regal, M. Greiner, and D. Jin, *Observation of Resonance Condensation of Fermionic Atom Pairs*, Phys. Rev. Lett. **92**, 040403 (2004).

[Ste01] D. Steck, *Rubidium 87 D-Line Data*, http://steck.us/alkalidata (2001).

[Tha00] G. Thalhammer, *Frequenzstabilisierung von Diodenlasern bei 850, 854 und 866 nm mit Linienbreiten im Kilohertz-Bereich*, Magister thesis at Leopold-Franzens-Universität Innsbruck (February 2000).

[Tie02] U. Tietze and C. Schenk, *Halbleiter-Schaltungstechnik*, Springer Verlag (2002).

[Woh01] W. Wohlleben, F. Chevy, K. Madison, and J. Dalibard, *An Atom Faucet*, Eur. Phys. J. D **15**, 237 (2001).

[Wyn00] R. Wynar, R. Freeland, D. Han, C. Ryu, and D. Heinzen, *Molecules in a Bose-Einstein Condensate*, Science **287**, 1016 (2000).

Acknowledgments

I would like to acknowledge my supervisors Andrew Wilson, Johannes Hecker Denschlag and Rudi Grimm. Thank you for your guidance and faith, and for knowing when a push in the right direction or a pat on the shoulder was needed, and a kick in the bum deserved. I would like to express my gratitude to Günter Kaindl, without whose encouragement none of this would have happened.

A big thank you goes to Nick Thomas, Peter Stroud, Gregor Thalhammer, Gerhard Hendl, and Klaus Winkler for their ongoing patience, invaluable help and company in the lab and workshops. I don't know what I would have done without you!

Thank you to everyone in the groups of Hardy Gross and Martin Wolf at the FU Berlin for granting asylum, providing the disk space, the soft– and hardware that made writing up possible. Besides this, you were great company!

Cheers–big–ears to Reece Geursen, for being a tremendously good friend and precious (and amazingly thorough) proof–reader.

Thanks to everyone in the groups at Otago and Innsbruck for welcoming me in their midst, and many helping hands. You are too many to be named here ... but I would like to mention: Cheng Chin - for being my weekend and late night info–point; Angela Mellish - thanks for all your help; Matthias Theis - staying friends in the rat–race; Brent Russel and David Hutchinson - for your company during many needed (and occasionally deserved) coffee breaks;

Many thanks to all willing to start endless discussions and provide valuable comments while writing up: Boris Kastening, Wieland Schöllkopf, Nicole Helbig, Julie Fry, Francois Snous–de–Pain, Jane Clark, Nils Henningsen, Isabel Torrente, and Juliane Schwendike.

I gratefully acknowledge the DAAD (Deutscher Akademischer Austauschdienst), Referat 411, and the SFB "Control and Measurement of Coherent Quantum Systems" of the FWF (Österreichischer Fonds zur Förderung der Wissenschaftlichen Forschung) for support.